

POLITECNICO DI TORINO

Department of Engineering

Master Degree in Mechanical Engineering

Master Degree Thesis

Effect of non metallic inclusions on the fatigue  
life of ball bearing



Tutor:  
Ing. Raffaella Sesana

Candidate:  
Stefano Gili

Academic Year 2019/2020

# Contents

<b>1 Introduction</b>	<b>3</b>
<b>2 Rolling Contact Fatigue</b>	<b>9</b>
2.1 Hertz theory .....	10
2.1.1 Hypothesis .....	11
2.1.2 Geometry around the contact area .....	11
2.1.3 Stress on sub-surface .....	13
2.2 A review of bearing life model .....	15
2.2.1 Lundberg-Palmgren model .....	15
2.2.2 Ioannides-Harris model .....	16
2.2.3 Zaretsky model .....	17
<b>3 Non metallic inclusion</b>	<b>21</b>
3.1 Type of inclusion .....	21
3.2 Factors that influence the stress peak .....	23
3.2.1 Dimension .....	23
3.2.2 Depth .....	25
3.2.3 Shape .....	26
3.2.4 Chemical composition .....	28
<b>4 Experimental test</b>	<b>30</b>
4.1 Rotating bending machine .....	30
4.2 Tension-tension testing machine .....	33
4.3 Test rigs for bearing .....	36
4.4 Fracture inspection .....	41

<b>5 Eshelby model</b>	<b>43</b>
5.1 Equivalent inclusion method .....	44
5.2 Numerical solver .....	45
<b>6 Ball frequency</b>	<b>47</b>
6.1 Ball spin frequency .....	48
6.2 Transversal slip .....	49
<b>7 Statistics of extreme values method</b>	<b>53</b>
7.1 Calculation procedure .....	54
7.2 Cleanliness analysis .....	55
7.3 Experimental data .....	56
<b>8 Results</b>	<b>60</b>
8.1 Raw Material results .....	60
8.1.1 Rotating bending test .....	60
8.1.2 Implementation of numerical model .....	66
8.2 Tension-tension test .....	74
8.2.1 Cleanliness analysis .....	78
8.3 Balls test results .....	82
8.3.1 Implementation of numerical model .....	82
8.3.2 Ball bearing life prediction ( $L_{10}$ ) .....	98
8.3.3 Simulation of worst cases .....	99
<b>9 Conclusion</b>	<b>101</b>
<b>10 Future works</b>	<b>103</b>

# Chapter 1

## 1.Introduction

Tsubaki Nakashima Co., Ltd. is one of the biggest company in the field of bearing manufactures. In particular it is specialized in the production of rolling contact elements which can be made of different shape (balls or cylinder) or material (steel or ceramic).

Pinerolo plant, where this work was carried out, takes care of steel balls bearings production.

Bearing is as a part of a machine that allows one part to rotate or move in contact with another part with as little friction as possible. Additional functions include the transmission of loads and enabling the accurate location of components. [1]

A wide variety of bearing designs exists to allow the demands of the application to be correctly met for maximum efficiency, reliability, durability and performance.

Bearings are composed of different elements: cylinders or balls as rolling elements and external and internal rings, which form the raceways. Also the lubrication between the parts is very important.

Fatigue life performances of the rolling elements have a key role to prevent premature failures of the bearings during working operations. For this reason, it is important to understand how the microinclusions affect the life of the balls and consequently of the bearing.

It is now been clearly established that fatigue resistance correlates strongly with steel cleanliness. However, inclusions are inevitably present in steels, they cannot be eliminated in the steelmaking process,[2] therefore many technical and commercial decisions by bearing manufacturers and end users depend on information regarding steel cleanliness and its effect on predicted bearing fatigue life. Historically, these information are based of experimental testing data. Bearing samples are ultrasonically inspected for steel cleanliness and then put on physical test rigs for fatigue life testing. Empirical relationships between

steel cleanliness and bearing life performance are obtained through the curve fitting of test data [3]. This has been a very costly and time-consuming practice.

Because of this, many studies were made to better understand which characteristics of inclusion are more relevant for the fatigue life, and a solution to calculate fatigue limit of steel considering inclusions presence.

In general, rolling contact fatigue is driven by two phenomena: surface originated pitting and subsurface originated spalling. These two are different, at the point that they can be considered separately. The first one can be prevented with better lubricants or a better surface finish [4], while there are not many ways to stop subsurface originated fatigue. Subsurface cracks mostly occur at stress concentration sites such as material defects, voids and non-metallic inclusions. Such inclusions act like stress risers, leading to cracks and final failure [5]. The inclusions are very critical since they are in a position where the shear stress due to the Hertzian contact is maximum. Many studies, both experimental and numerical ones, have been carried out to understand the most important factors that affect RCF life. Nowadays it is known that they are: inclusion composition, size, shape and location [2]. The relationship between the RCF life and the maximum inclusion size has been studied by Nagao et al.[6] and Seki [7], but the results are different of one order of magnitude even if the size of the inclusion is the same.

Hashimoto et al. [2] made experimental tests to analyze the role of the composition using different deoxidation post-processes. The size and composition are evaluated thanks to an optical microscopy and an X-ray energy dispersive spectroscopy (XREDS). The tests showed that the RCF life in case of similar sized inclusions, is affected primarily by the chemical composition. In particular, they showed that RCF life is improved reducing the oxygen content as the size of the oxides. Moreover, they examined the length of the crack around the inclusions throughout the test, finding out that the crack length controlling RCF life is influenced by the interface condition between the inclusion and the matrix. Since matrix-MnS and matrix-TiN interfaces showed no cavities, they suggested that the oxide inclusions play the most detrimental role in the material's RCF. Also S. M. Moghaddam et al.[5] and J. Guan et al.[8] studied the effect of the inclusion composition, considering the inclusion

elastic modulus. The maximum von Mises stress increases with the increase of the elastic modulus of the inclusion and it appears at the interface between inclusion and surrounding material. Cerullo and Tvergaard [9] compared TiN and Al<sub>2</sub>O<sub>3</sub> inclusions using a micromechanical approach to estimate the locations around inclusions that will be most critical for the initiation of fatigue failure, and the loads at which fatigue will initiate. They used a multiaxial fatigue criterion to ensure that the stress cycles in the structural alloy around the inclusion do not exceed the fatigue limit. They conclude that for a given volume  $V_f$  a higher maximum damage factor is practically always reached in the matrix with an alumina inclusion rather than with a titanium nitride inclusion. They expected this conclusion, since the alumina has a higher  $E_h/E_m$  (inclusion elastic modulus/matrix elastic modulus) ratio than that of the titanium nitride,

The effect of size, stiffness and depth has been shown in [5] and in [8]. The authors of [5] and [8] developed a model that takes advantage of the Voronoi tessellation to construct the FEM domain. In this way, the model is able to capture the butterfly wing formation, crack initiation and crack propagation. Moreover, the model was used to study the different RCF life varying size, stiffness and depth. Regarding the size, a comparison between a 16  $\mu\text{m}$  and a 8  $\mu\text{m}$  inclusions with the same stiffness value and depth, has been made [5]. Similar test were performed in [8], with a set of inclusions which is set to vary from 5  $\mu\text{m}$  to 20  $\mu\text{m}$ . No strong influence on stress concentration was found, but it is known that larger inclusions subject larger volumes of the material to stress concentration. Furthermore, larger inclusions have a higher chance of being located at the critical depth. For what concerns the inclusion location, the stress profile changes at the inclusion depth, while the rest of the profile remains pristine. Inclusions located at 0.5 times the contact half width ( $b$ ) are critical [5], since there is the maximum von Mises stress calculated from the Hertz theory. For a certain value of depth, the stress rise remains below the original stress at  $0.5b$ , so the inclusion will not be the controlling phenomenon of the RCF life. J.Guan et al. [8] showed that the highest stress concentration is located at about  $0.75b$  but both [5] and [8] lead to the same conclusion. Taking into account the shape of the inclusion, Stienon et al.[10] showed that stress fields obtained with simplified shape are in good agreement with those obtained with real shape,

therefore is reasonable to use simplified shapes to simulate the stress concentration around the inclusion. Yutaka Neishi et al. [11] did ultrasonic fatigue tests on different specimens with different MnS inclusions shape and It was found that the RCF life was well correlated with the length of MnS, since the initiation of shear crack in the subsurface was accelerated as the length of MnS increased.

Once that the effect of microinclusions on the material matrix is clarified, it would be very useful to have a model that is capable to predict the fatigue limit considering the steel cleanliness.

Y. Murakami [12] predicted the upper and the lower limits of fatigue strength relating the fatigue limit to the Vickers hardness of a matrix and the maximum size of inclusions defined by the square root of the projected area of an inclusion. He estimated the expected value of inclusion size in a definite numbers of specimens or machine components using the statistics of extreme values.

Lamagnere et al. [4] presented a model that calculates the fatigue limit  $H_1$  of the bearing steel, it is the maximum Hertzian pressure that would not introduce any plastic deformation. They approximated the inclusion geometry to be ellipsoidal and used the Eshelby method to calculate the effect of aluminum oxide and molybdenum carbide inclusions on the fatigue limit of M50 steel as a function of temperature. The fatigue limit threshold is derived from the comparison between the local shear stress around the inclusion and the microyield stress of the matrix. The idea of a stress threshold below which a material would not be damaged was first introduced by Weibull [13], and then developed in bearing fatigue life models by several authors [14], but without considering the steel cleanliness. The local shear stress around the inclusion is calculated with the Eshelby method [15], while the microyield stress of the matrix is evaluated by means of experimental compression tests. J Courbon et al. [16] extended this work by examining the interaction between multiple inclusions (pairs, clusters and stringers) using the Moschovidis and Mura extension [17] of the Eshelby method [15] They found out that the orientation of the axes according to which the inclusions are arranged, plays a fundamental role on the stress field. Vincent et al. [18] further extended

this concept by adding the effects of residual stresses and graded material properties in carburized steels. However, these studies have not included many other factors which may affect the fatigue limit. For example, the only effect of temperature accounted for was the change in yield strength of the steel matrix. There are other factors that change with temperature that may contribute to the reduction in the fatigue limit e.g. thermal expansion and elastic modulus.

For this reason Bryan Allison and Anup Pandkar [19] extended Lamagnere work [4] using a finite element simulations to determine which factors have the largest impact on the estimated fatigue limit of bearing steels under rolling contact. It was found that porosity and debonded inclusions dominate the fatigue limit of bearing steels. When these are excluded, the change in mechanical properties (elastic modulus and matrix yield strength) due to temperature are the next most important factors followed by the distance between inclusions. The geometry (size, aspect ratio, and orientation) of a single inclusion were all found to have a relatively small effect on the overall fatigue limit.

Taking into account the bearing life prediction Jalalahmadi and Sadeghi [20] developed a two dimensional Voronoi finite element method (VFEM) using the Voronoi tessellation to simulate the material microstructure and its effects on rolling contact fatigue. They generate the microstructure of bearing using the Voronoi cells to create the semi-infinite domain and the circular inclusion is considered as a grain with different material properties. Then they did numerical simulation in order to modify Lundberg-Palmegren fatigue criterion [21] considering the effect of the inclusion. Four different characteristics of inclusions were studied, that is, their stiffness, size, depth, and number, they consider a baseline case for inclusion parameters that is common between all of simulations such that the different results can be compared to each other. Then they did simulations changing one characteristic at a time in order to found four different coefficient one for each characteristic. Employing these coefficients, a RCF life equation was developed that is able to predict the fatigue lives of the bearing elements including the effects of the material inclusions.

The current work investigates the effect of microinclusions on fatigue life of a steel alloy (100Cr6) for bearing rolling elements.

Works was divided in four main parties:

- Fatigue test on ball bearing and raw material are made in order to get real data
- A dedicated 3D solver implementing Eshelby model [4] was developed to estimate the stress distribution surrounding the microinclusion
- Frequency with which a ball of a bearing spin was calculated in order to understand how often a microinclusion, present in the steel matrix of the ball, will be stressed.
- Knowing the stress of the steel matrix, the stress at the boundary of the inclusion and the frequency with which the inclusion is stressed a new equivalent load  $P_{eq}$  is identify. Then a different  $L_{10}$  considering the effect of the inclusion is calculated.

# Chapter 2

## 2 Rolling contact fatigue

Rolling-contact fatigue is defined as a failure or material removal driven by crack propagation caused by the near-surface alternating stress field. It is typically considered that if a bearing is properly mounted, aligned, lubricated, maintained and not overloaded, then the material fails due to RCF [22].

Two categories in which RCF may be manifested are surface-originated pitting and subsurface-originated spalling. Surface-originated pitting occurs due to the presence of surface distresses such as dents, fretting scars, etc., on the surface of the contacting bodies. However, if the contacting bodies are relatively smooth, then the main mode of RCF is subsurface-originated spalling [23]. Spalling is a catastrophic contact fatigue failure mode for rolling contact element typically appears near the presence of an inclusion or material inhomogeneity inside the material domain, it was the result of subsurface crack initiation and propagation for modern bearings. [24]

RCF life depends on many factors like: [1]:

- Contact pressure
- Material properties
- Lubricant properties
- Surface roughness
- Relative slip during the rotation between the elements
- Microstructure
- Cleanliness condition
- Residual stress

Rolling contact fatigue differs from the classical fatigue due to several characteristic conditions [25]:

- The state of stress in nonconformal contacts is complex and multiaxial and governed by the Hertzian contact theory.
- The loading history at a point below the surface is nonproportional, the stress components do not rise and fall with time in the same proportion to each other;
- There is a high hydrostatic stress component present in the case of nonconformal contacts.
- The phenomenon of RCF occurs in a very small volume of stressed material.
- Localized plastic deformation and development of residual stresses play crucial role in the fatigue damage.
- The principal axes in nonconformal contacts constantly change in direction during a stress cycle due to which the planes of maximum shear stress also keep changing. Thus, it is difficult to identify the planes where maximum fatigue damage occurs.

For this reason, it is impossible to directly apply the results from classical fatigue to RCF.

## 2.1 Hertz theory

Theoretically, the contact area of two spheres is a point, and it is a line for two parallel cylinders. As a result, the pressure between two curved surfaces should be infinite for both of these two cases, which will cause immediate yielding of both surfaces. However, a small contact area is being created through elastic deformation in reality, limiting the stresses considerably. These contact stresses are called Hertz contact stresses, which were first studied by Hertz in 1881.

## 2.1.1 Hypothesis

In order to solve the problem have been made the following assumptions:

- The two surfaces in contact are continuous and they can be represented with polynomial
- Elastic and isotropic material
- The bodies are in frictionless contact
- Each body can be considered an elastic half-space, i.e., the area of contact is much smaller than the characteristic radius of the body.

## 2.1.2 Geometry around the contact area

Consider two bodies with radii of curvature  $R'$  and  $R''$ .

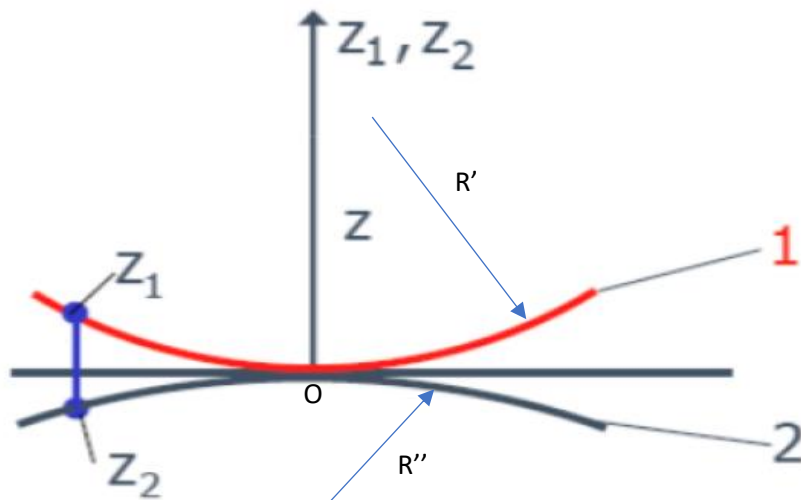


Figure 2.1 – Contact between two bodies

Before deformation the bodies touch at O and the separation of point  $Z_1$  and  $Z_2$  is:

$$h = |Z_2 - Z_1| = \frac{1}{2R'} X^2 + \frac{1}{2R''} Y^2$$

Applying a normal load, the two bodies are compressed. The separation of  $Z_1$  and  $Z_2$  is now:

$$h' = h - (\delta_1 + \delta_2) + (w_1 + w_2)$$

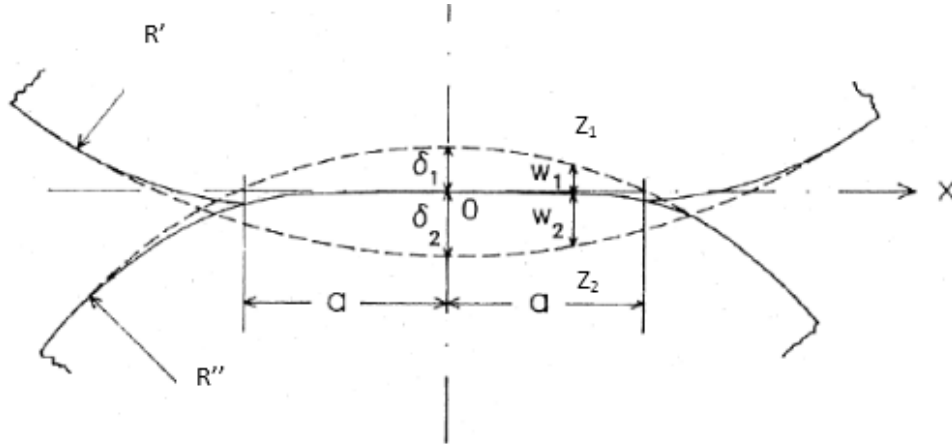


Figure 2.2 – Hertz contact

If points  $Z_2$  and  $Z_1$  are within the contact area  $h' = 0$

$$w_1 + w_2 = \delta - \frac{1}{2R'} X^2 - \frac{1}{2R''} Y^2 \quad [1]$$

- $w_1 + w_2 =$  the elastic displacement
- $\delta = \delta_1 + \delta_2 =$  displacement of bodies

The elastic displacement at distance  $r$  is:

$$W(r) = \frac{1-\nu^2}{\pi E} \frac{P}{r}$$

On each area element:  $dA = dx'dy'$  inside the contact surface at a point  $(x',y')$ ,  $P$  is:

$$dP = p(x',y')dx'dy'$$

- $P =$  normal load
- $p =$  contact pressure

The displacement due to  $P$  at any points  $Z(x,y)$  is:

$$w(x,y) = \frac{1-\nu^2}{\pi E} \int_S \frac{p(x',y')}{r'} dx'dy' \quad [2]$$

$$r' = ((x-x')^2 + (y-y')^2)^{1/2}$$

It follows from equation 1 and 2 that an ellipsoidal distribution evolved satisfy the equation:

$$p(x,y) = p_0 \left(1 - \frac{a}{x^2} - \frac{b}{y^2}\right)^{1/2}$$

- $p_0 = p_{max} = \frac{3P}{2\pi ab}$
- $a, b =$  semi axes of the elliptic contact surface. The values of the semi axes depend on the solution of an integral equation, which is normally given in numerical form.

### 2.1.3 Stress on sub-surface

Experimental evidence shows that failure starts at points below the surface. For this reason, it is interesting to know the 3D stress status along the z-axis, which is the one that is parallel to the applied force. In this way, it is possible to calculate the principal stresses and then the maximum tangential stress, the von Mises stress and so on. The stresses below the surface, for the sphere-sphere contact and for the cylinder-cylinder contact, are represented below (Fig.2.3, Fig.2.4) and that is similar to what happens in the sphere-ring contact inside a bearing.

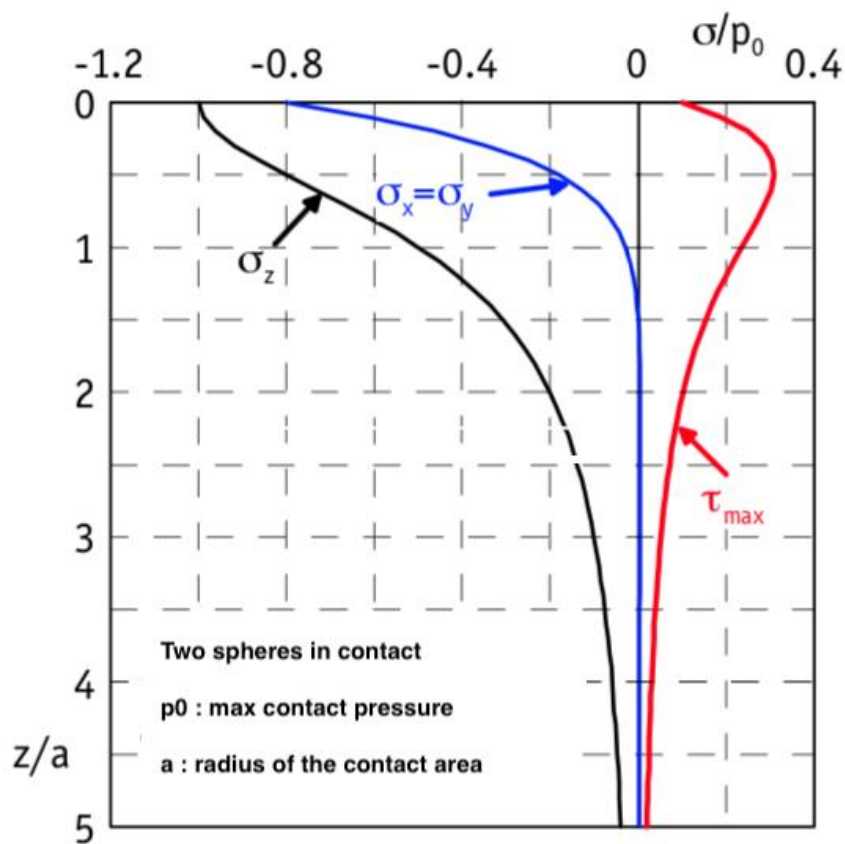


Figure 2.3 - Subsurface stresses: sphere-sphere contact

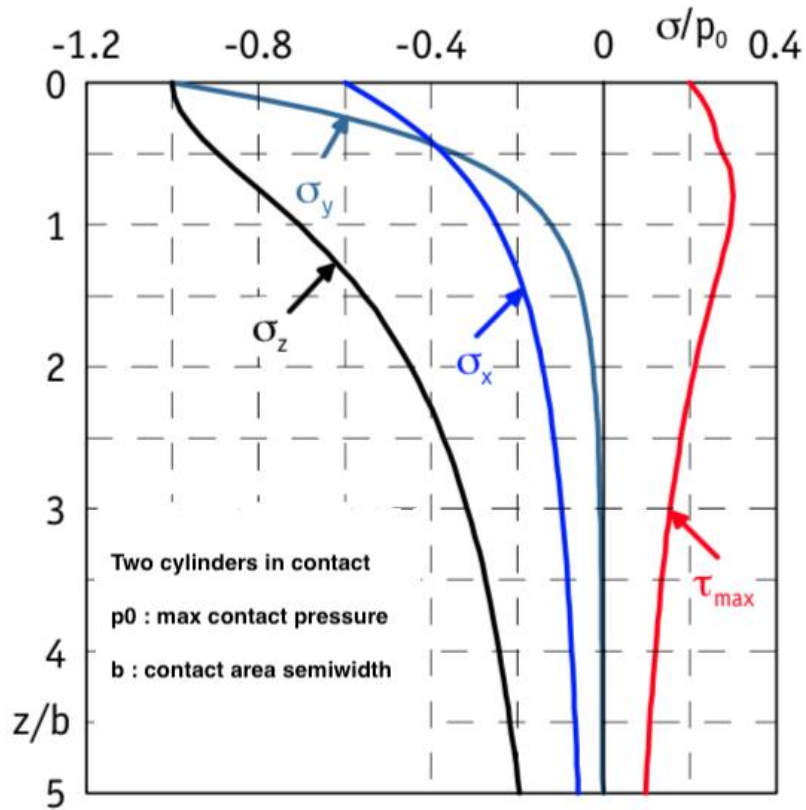


Figure 2.4 - Subsurface stresses: cylinder-cylinder contact

Many researches have been conducted to study which shear stress (maximum tangential stress, von Mises stress, Tresca stress) is the one that has to be considered in the context of fatigue of contacting bodies [26]. Their roles can in principle be determined by comparing the respective stress distributions against the location of maximum damage in experiments. However, whichever shear stress is considered, the maximum occurs below the contact surface and this has significant consequences to the development of damage. Notice that the shear stress is proportional to the contact pressure  $p_0$  but the proportionality constant will depend on the geometry of the contact.

## 2.2 A review of bearing life model

Since fatigue is the predominant mode of failure in rolling element bearings, the life of bearings is governed by RCF. Over the years, several mathematical models have been proposed to estimate lives of bearing components under RCF. These models can be classified into probabilistic engineering models and deterministic research models. The engineering models are largely empirical in nature and include variables that are obtained from extensive experimental testing. They do not directly consider the details of the constitutive behavior of materials under contact loading, nor the residual stress and strain computations in the contact areas. The research models, on the other hand, are theoretical in nature, require complete stress-strain behavior information for the materials in contacts, and are used in conjunction with a material failure model. However, these models are usually confined to a specific aspect of the failure process, e.g., only the crack initiation part or only the crack propagation part. Due to the special nature of RCF and the inability to relate directly to classical component fatigue, most of the early work in determining lives of rolling bearings was based on empirical results.

### 2.2.1 Lundberg-Palmgren model

The first theoretical basis for the formulation of a bearing life model was provided by the seminal work of Lundberg and Palmgren [21]. They supposed that a crack initiates at subsurface due to the simultaneous occurrence at a particular depth of the maximum orthogonal shear stress and a weak point in the material. Such weak points were hypothesized to be statistically distributed in the material. The Weibull statistical strength theory was applied to the stressed volume in a pure Hertzian contact to obtain the probability of survival of the volume from subsurface initiated fatigue. Failure was assumed to be crack initiation dominant.

For the first time they derived the relationship between individual component life and system life. A bearing is a system of multiple components, each with a different life. As a result, the life of the system is different from the life of an individual component in the

system. The  $L_{10}$  bearing system life, where 90 percent of the population survives, can be expressed as [8]:

$$L_{10} = \left(\frac{C_d}{P_{eq}}\right)^p$$

- $p$  is the load-life exponent and is 3 for ball bearings and  $\frac{10}{3}$  for roller bearings;
- $C_d$  is the dynamic load capacity for a rolling-element, defined by Lundberg and Palmgren as the load placed on a bearing that will theoretically result in a  $L_{10}$  life of 1 million inner-race revolutions;
- $P_{eq}$  is the equivalent load, defined as the combined and variable load around the circumference of a ball bearing;

### 2.2.2 Ioannides-Harris model

Ioannides and Harris [14] using Weibull and Lundberg and Palmgren introduced a fatigue limiting shear stress  $\tau_u$ . They modified Lundgren-Palmgren equation using the fatigue limit load  $P_u$  that is a function of  $\tau_u$ :

$$L_{10} = \left(\frac{C_d}{P_{eq} - P_u}\right)^p$$

When  $P_{eq} < P_u$ , bearing life is infinite and no failure would be expected. When  $P_u = 0$ , the life is the same as that for Lundberg and Palmgren.

### 2.2.3 Zaretsky model

All models earlier described relate the critical shear stress-life exponent  $c$  to the Weibull slope  $e$ , in fact they derived their results starting from Weibull equation:

$$\eta \sim \frac{1}{\tau} \frac{1^{c/e}}{V^{1/e}}$$

- $\eta$  is the number of stress cycles to failure.
- $V$  is the stressed volume

The parameter  $c/e$  thus becomes the effective critical shear stress-life exponent, implying that the critical shear stress-life exponent depends on bearing life scatter or dispersion of the data.

From the experimental data the exponent appears to be independent of scatter or dispersion in the data, so Zaretsky [27] has rewritten the Weibull equation to reflect that observation by making the exponent  $c$  independent of the Weibull slope  $e$ :

$$\eta \sim \frac{1}{\tau} \frac{1^c}{V^{1/e}}$$

Also, differently to Ioannides-Harris Zaretsky that used Von Mises criterium to determine the fatigue limiting shear stress  $\tau_u$ , he chose the maximum shear stress.

From these considerations he wrote the following equation:

$$L_{10} = LF_c \cdot \left(\frac{C_d}{P_{eq}}\right)^p$$

- $p$  is the load-life exponent and is 3 for ball bearings and  $\frac{10}{3}$  for roller bearings;
- $C_d$  is the dynamic load capacity for a rolling-element, defined by Lundberg and Palmgren as the load placed on a bearing that will theoretically result in a  $L_{10}$  life of 1 million inner-race revolutions;
- $P_{eq}$  is the equivalent load, defined as the combined and variable load around the circumference of a ball bearing;
- $LF_c$  is the bearing life factor;

The equation of  $C_d$  and  $P_{eq}$  are shown below:

$$P_{eq} = X \cdot F_r + Y \cdot F_a$$

Where:

- $F_r$  is the radial component of the load;
- $F_a$  is the axial component of the load;
- $X$  is a rotation factor, defined as the bearing capacity of the conditions of rotation = 0,35;
- $Y$  is the thrust load factor of the bearing = 0,57.

The dynamic load capacity, expressed in Newton:

$$C_D = f_{cm}(i \cos \phi)^{0,7} (\tan \phi) Z^{\frac{2}{3}} d^{1,8}$$

Where:

- $f_{cm}$  is material-geometry coefficient. The material-geometry coefficient depends on the bearing type, material, and the conformity between the rolling elements and the races;
- $i$  is the number of rows of rolling elements;
- $d$  is the ball diameter;
- $Z$  is the number of rolling elements for each row  $i$ ;
- $\phi$  is the bearing contact angle. The contact angle is defined as the angle between the line joining the points of contact of the ball and the raceways in the radial plane, along which the combined load is transmitted from the raceways, and the line perpendicular to bearing axis;

For angular contact ball bearings, the life factor is dependent from several factors explained below.

$$LFC = \left( \frac{(LFi)^e (LFO)^e (2\chi^{e^e} + 1)}{2(LFO)^e \chi^e + (LFi)^e} \right)^{\frac{1}{e}}$$

- $e = \tan \alpha$  is the Weibull slope ( $\alpha$  is the angle between the Weibull distribution and x-axis).
- $LF$  is the ball-race conformity effects at the inner and outer races, introduced by Zaretsky, is normalized for ball bearings with inner-race and outer-race conformities of 52 percent.

$$LF = \left( \frac{S_{max,0.52}}{S_{max}} \right)^n$$

- From Hertz theory  $S_{max}$  is the maximum contact stress.
- $n$  is the Hertz stress life exponent

$$n = c + \frac{2}{e}$$

where:

- $c = 9$  for ball bearings;
- $\chi$  is the outer to inner life ratio:

$$\chi = \left( \frac{\left( \frac{2 \cos \phi}{d_e - d \cos \phi} + \frac{4}{d} \frac{1}{f_i d} \right)^{\frac{2}{3}} (\mu\nu)_o}{\left( \frac{2 \cos \phi}{d_e - d \cos \phi} + \frac{4}{d} \frac{1}{f_o d} \right)^{\frac{2}{3}} (\mu\nu)_i} \right)^n$$

The bearing geometry is defined in figure 2.5, from Hertz contact theory, the dimensions for the pressure area is given in terms of transcendental functions  $\mu$  and  $\nu$ . The values of the product of the transcendental functions ( $\mu\nu$ ) are tabulated in function of ball bearing envelope size ( $S$ ) and they are different for the inner and outer races.

$$S = \frac{d \cos \phi}{d_e}$$

The conformity of the races ( $f$ ) is defined as the ratio between the race radius ( $R_r$ ) and the ball diameter.

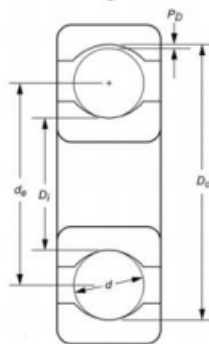


Figure 2.5 - Characteristic bearing dimensions.

The evaluation of  $LF$  is dependent on the geometry of the bearing, in this case, for angular thrust loaded ball bearing, they have been calculated the Ball-Inner race conformity effect ( $LF_i$ ) and the Ball-Outer race conformity effect ( $LF_o$ ).

$$LF_i = \left( \frac{\left(\frac{2}{d_e-d} + \frac{4}{d} - \frac{1}{0.52d}\right)^{\frac{2}{3}} (\mu\nu)_i}{\left(\frac{2}{d_e-d} + \frac{4}{d} - \frac{1}{f_i d}\right)^{\frac{2}{3}} (\mu\nu)_{0.52}} \right)^n$$

$$LF_o = \left( \frac{\left(\frac{2}{d_e-d} + \frac{4}{d} - \frac{1}{0.52d}\right)^{\frac{2}{3}} (\mu\nu)_o}{\left(\frac{2}{d_e-d} + \frac{4}{d} - \frac{1}{f_o d}\right)^{\frac{2}{3}} (\mu\nu)_{0.52}} \right)^n$$

- $\mu\nu_i$  is Transcendental function of Hertzian Contact theory for inner race
- $\mu\nu_o$  is Transcendental function of Hertzian Contact theory for outer race
- $\mu\nu_i$  is Transcendental function of Hertzian Contact theory with a conformity of 0.52

# Chapter 3

## 3 Non metallic inclusion

Non metallic inclusions are chemical compounds and nonmetals that are present in steel and other alloys. They are the product of chemical reactions, physical effects, and contamination that occurs during the melting and pouring process [28].

Non-metallic inclusions play an essential role in the length of the rolling contact fatigue (RCF) life, as fatigue cracks start growing from subsurface located inclusions where the shear stress reaches its maximum. However, inclusions are inevitably present in steels, they cannot be eliminated in the steelmaking process.

### 3.1 Type of inclusion

Non metallic inclusions are divided in four macro-categories based on similarities in morphology [29]:

- Sulfides
- Aluminates
- Silicates
- Oxides

Hard inclusions with low deformability are the most dangerous because may cause microcrack formation at the interface between the inclusion and the matrix during the steel-making process, which may make it possible for a fatigue crack to initiate from these microcracks.

Inclusion type	Inclusion	$\alpha \times 10^{-6}/^{\circ}\text{C}$ (0 ~ 800 °C)	E (GPa)	$\nu$
Sulphides	MnS	18,1	(69-138)	(0,3)
	CaS	14,7		
Calcium aluminates	CaS·6Al <sub>2</sub> O <sub>3</sub>	8,8	(113)	(0,234)
	CaS·2Al <sub>2</sub> O <sub>3</sub>	5,0		
	CaO·Al <sub>2</sub> O <sub>3</sub>	6,5		
	12CaO·7Al <sub>2</sub> O <sub>3</sub>	7,6		
	3CaO·Al <sub>2</sub> O <sub>3</sub>	10,0		
Spinels	MgO·Al <sub>2</sub> O <sub>3</sub>	8,4	271	0,260
	MnO·Al <sub>2</sub> O <sub>3</sub>	8,0		
	FeO·Al <sub>2</sub> O <sub>3</sub>	8,6		
Alumina	Al <sub>2</sub> O <sub>3</sub>	8,0	389	0,250
	Cr <sub>2</sub> O <sub>3</sub>	7,9		
Nitrides	TiN	9,4	(317)	(0,192)
Oxides	MnO	14,1	(178)	(0,306)
	MgO	13,5	306	0,178
	CaO	13,5	183	0,21
	FeO	14,2		

Table 3.1 - Values of coefficients of thermal expansion  $\alpha$ , Young's modulus  $E$ , and Poisson's ratio  $\nu$  (Brooksbank, 1970)

Alluminates consist of a number (at least 3) of round or angular oxide particles with aspect ratio less than 2 that are aligned nearly parallel to the deformation axis. (fig 3.1, 3.2) Oxides includes any other oxide particles that have globular shape (fig 3.3, 3.4).

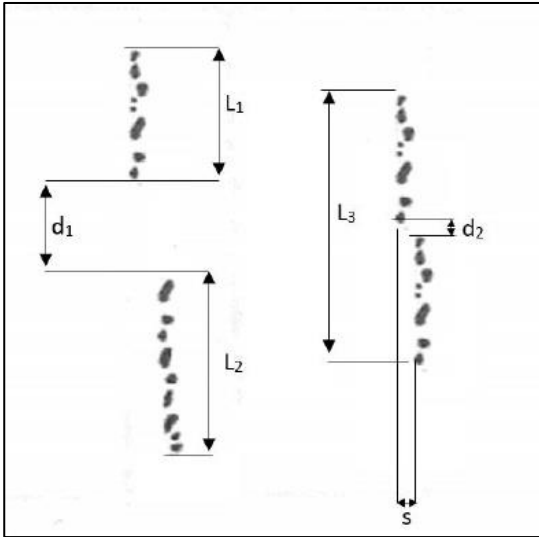


Figure 3.1 – Alluminates type

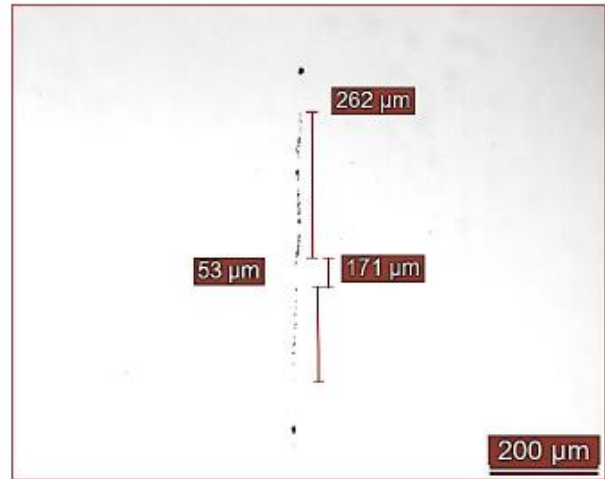


Figure 3.2 – Alluminates type

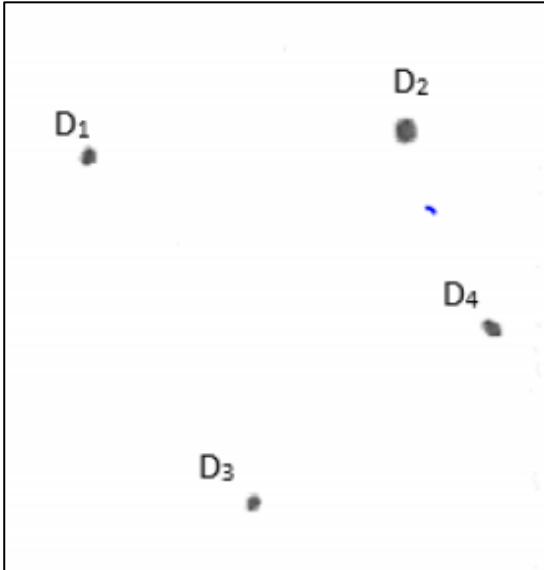


Figure 3.3 – Oxides type



Figure 3.4 – Oxides type

## 3.2 Factors that influence the stress peak

It is now well known that inclusions act like a stress raiser so it is important to understand which characteristics of the inclusion are more relevant for the increase of the stress in steel's matrix.

In the follow examples Eshelby's model [15] was applied for different inclusion to understand the effect of the shape, chemical composition, depth and dimension on the increase of stress at the boundary of the inclusions.

### 3.2.1 Dimension

The inclusion size affects the stress field around the inclusion: increasing the inclusion dimension the area subjected to a stress perturbation increases. On the other hand, the Tresca stress peak value does not change significantly. Nevertheless only inclusions which are larger than critical size could affect fatigue life. Critical size is the minimum dimension since inclusions are dangerous for the component subjected to rolling fatigue limit.

In the table are shown Tresca stress peak for different inclusion size, position and chemical composition are the same for the two example.

Simulation condition are:

- Elastic modulus of the matrix  $E_m$ : 210 GPa
- Elastic modulus of the inclusion  $E_h$ : 375 GPa
- Depth: 200 $\mu$ m

Tresca stress evaluated for different inclusion size	
Semiaxis of inclusion size [ $\mu$ m]	Tresca peak increment
0.5 x 0.5 x 0.5	+39%
50 x 50 x 50	+39%

Table 3.2 – Tresca stress evaluated for different inclusion size

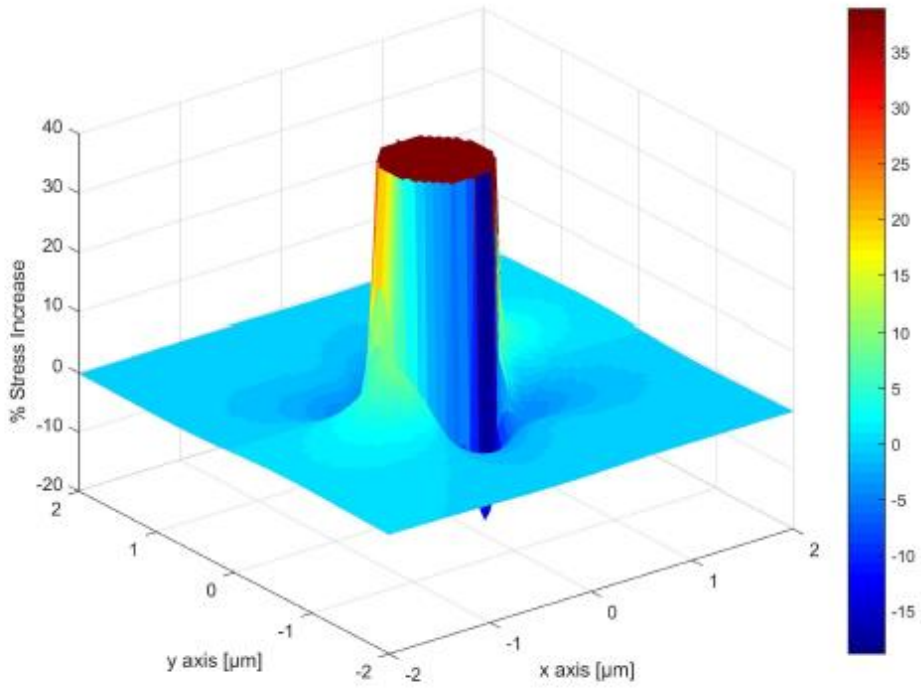


Figure 3.5 – Stress perturbation, Size 0.5x0.5x0.5 μm

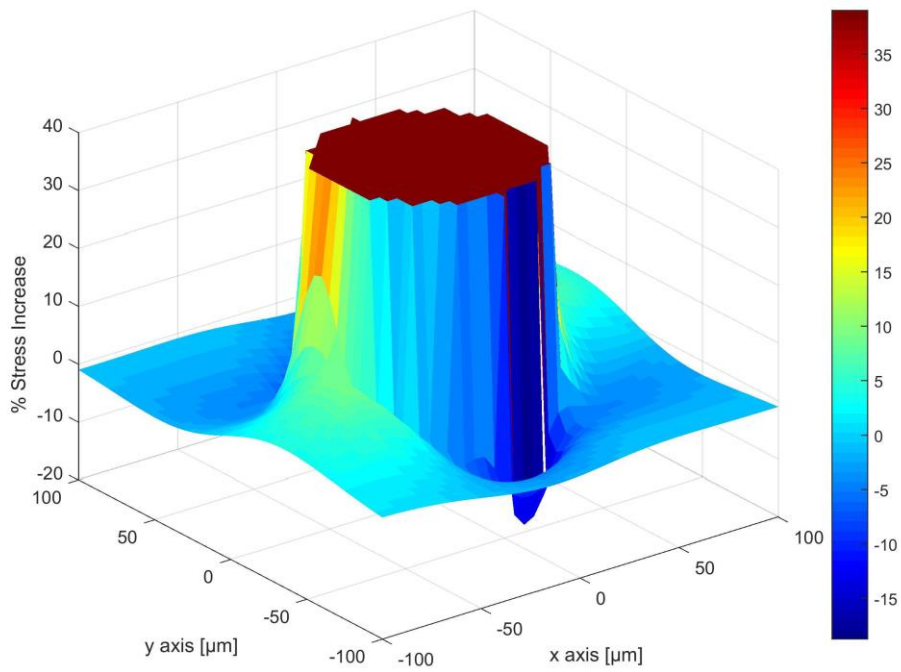


Figure 3.6 – Stress perturbation, Size 50x50x50 μm

### 3.2.2 Depth

Location of inclusion is very important because stress caused by Hertzian contact is related to the depth below the surface. From the Hertz theory, it is known that the maximum equivalent stress is located at a certain depth below the surface. This depth can be identified, with a good approximation, as:

$$Depth_{eq,max} = 0.75b$$

where  $b$  is the contact half width.

In fig 3.7 it is shown the stress increment [%] due to the NMI remains the same independently from the depth. Since steel matrix stress changes, the absolute increase is maximum at critical depth.

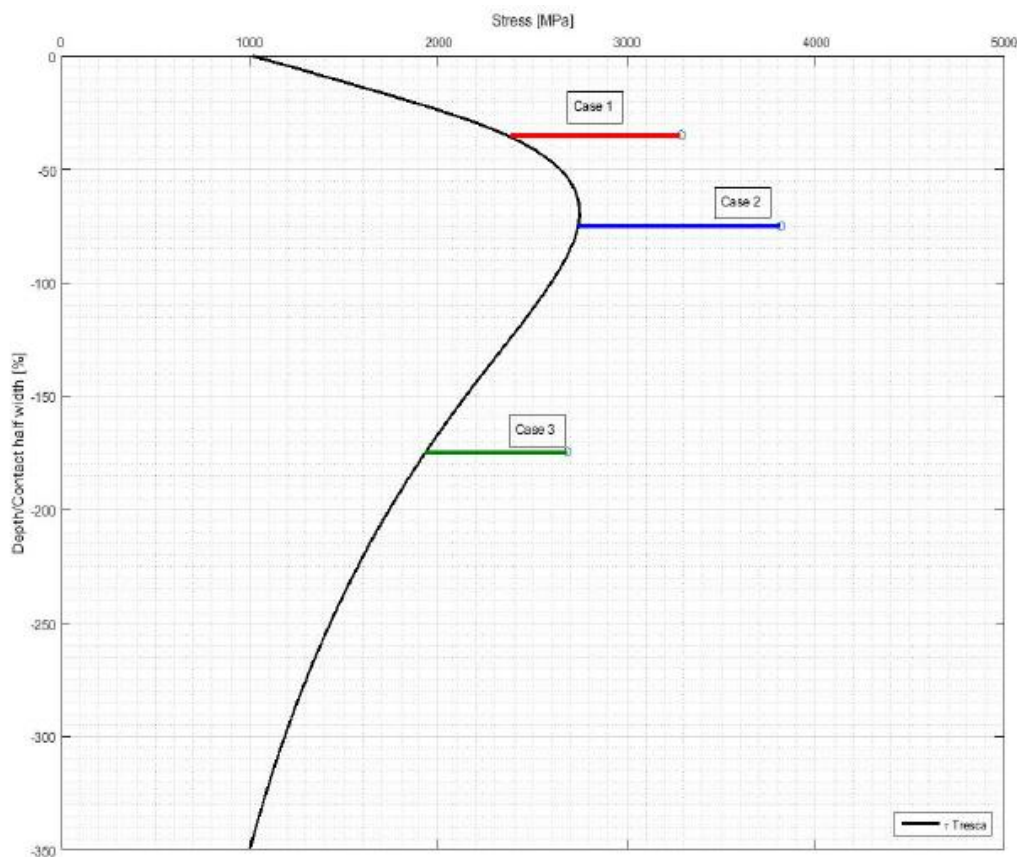


Figure 3.7 – Stress perturbation: effect of the depth

### 3.2.3 Shape

Shape is an important factor which influences the stress peak at the inclusion boundary. Ellipsoidal shape is more dangerous than spherical one, since larger is the difference of the length of semiaxes, larger is the Tresca peak increment. Numerical simulation was made changing the ratio between the two semiaxes  $a$  and  $b$  perpendicular to the force direction until one order of magnitude.

Simulation condition are:

- Elastic modulus of the matrix  $E_m$ : 210 GPa
- Elastic modulus of the inclusion  $E_h$ : 375 GPa
- Depth: 200 $\mu$ m

The results are showed below (Table 3.3):

Tresca stress evaluated for different ratio $a/b$		
Case	aspect ratio ( $a/b$ )	Tresca peak increment
1	1	+39%
2	2	+42%
3	10	+49%

Table 3.3 – Tresca stress evaluated for different ratio  $a/b$

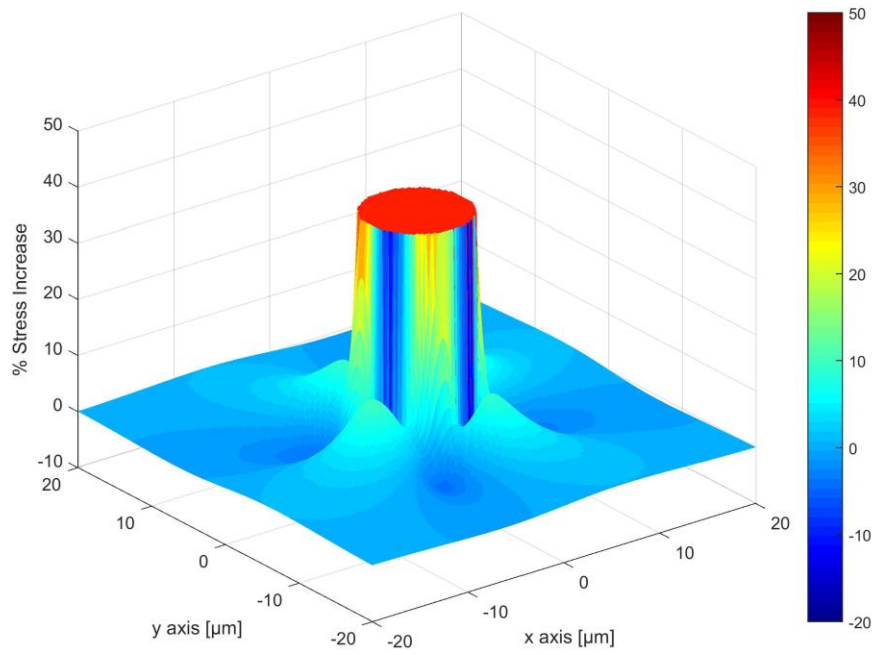


Figure 3.8 – Stress perturbation,  $a/b = 1$

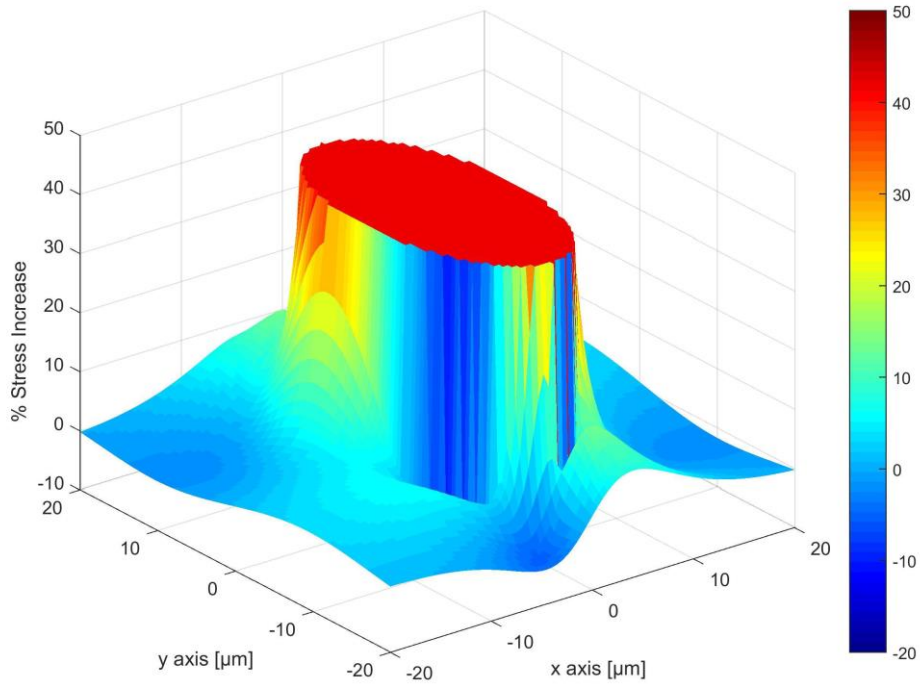


Figure 3.9 – Stress perturbation,  $a/b = 2$

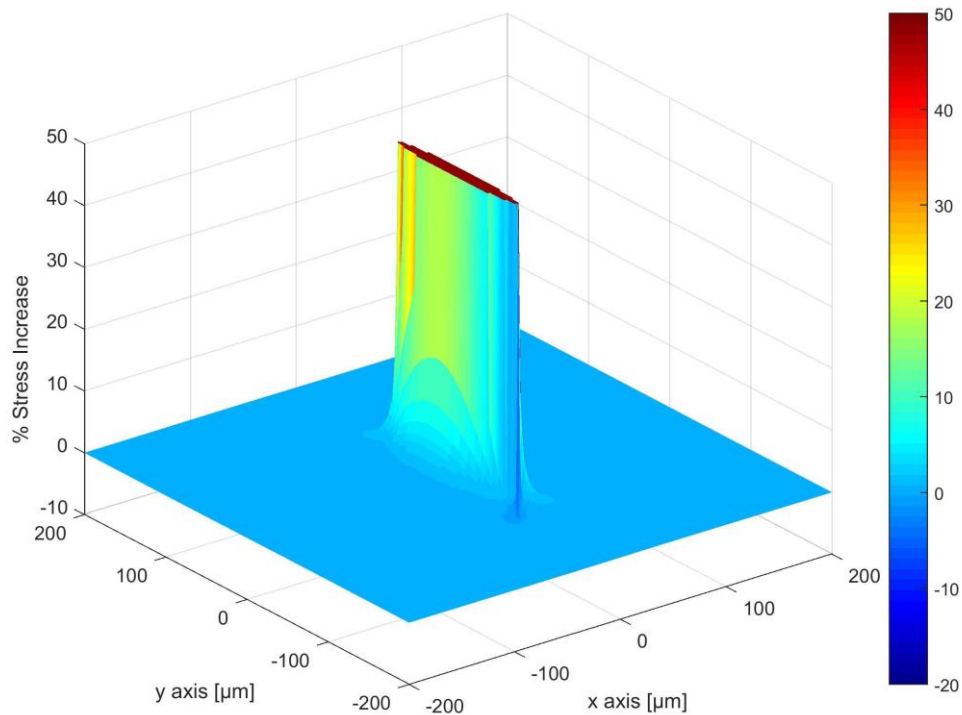


Figure 3.10 – Stress perturbation,  $a/b = 10$

### 3.2.4 Chemical composition

Most inclusions in bearing steels, are non metallic (NMI), and typically they are stiffer than the matrix. In fact, referring to experimental cases, few of the most common ones are Allumina ( $Al_2O_3$ ), Titanium nitrides (TiN) and Titanium carbides (TiC) and each of them has an elastic modulus that is approximately 1.8 times or higher than the elastic modulus of the pure steel. Furthermore, other types of inclusions can be found in steels, typically they are not detrimental as the ones presented above since they are not as stiff as those. In the cases presented here, the peak increment remains almost the same, but this effect is due to a similar Young modulus. Major changes on the elastic modulus will lead to larger increments, since they are related to the difference between  $E_m$  and  $E_h$ : if the difference from  $E_h$  and  $E_m$  increases, the peak increases. Another parameter is the Poisson ratio of the matrix  $\nu_m$  and the inclusion  $\nu_h$ , index of the shrinkage and the expansion of the sample. Similarly to what seen for the Young modulus, if the difference between  $\nu_h$  and  $\nu_m$  increases, also the peak increases.

Simulation condition are:

- Elastic modulus of the matrix: 210 GPa
- Elastic modulus of the inclusion TiN: 380 GPa
- Elastic modulus of the inclusion TiC: 375 GPa
- Elastic modulus of the inclusion Al<sub>2</sub>O<sub>3</sub>: 375 GPa
- Depth: 200μm
- Aspect ratio ( $a/b$ ) = 10

Tresca stress evaluated for different chemical composition		
Case	Chemical composition	Tresca peak increment
1	Al <sub>2</sub> O <sub>3</sub>	+36%
2	TiC	+36%
3	TiN	+37%

Table 3.4 – Tresca stress evaluated for different chemical composition

# Chapter 4

## 4 Experimental test

Experimental tests have been made in order to get real data of the failure caused by inclusions. It is important to test both raw material and finished product (Balls,  $d=11.112$  mm), Balls were tested in a special bench, instead raw material on an axial fatigue testing machine or rotating bending machine.

### 4.1 Rotating bending machine

This machine demonstrates the fatigue failure of materials when subject to alternating stresses, it uses a motor to rotate a specimen with a load at its free end.

In fig. 4.1 it is shown a diagram of the machine used in this work:

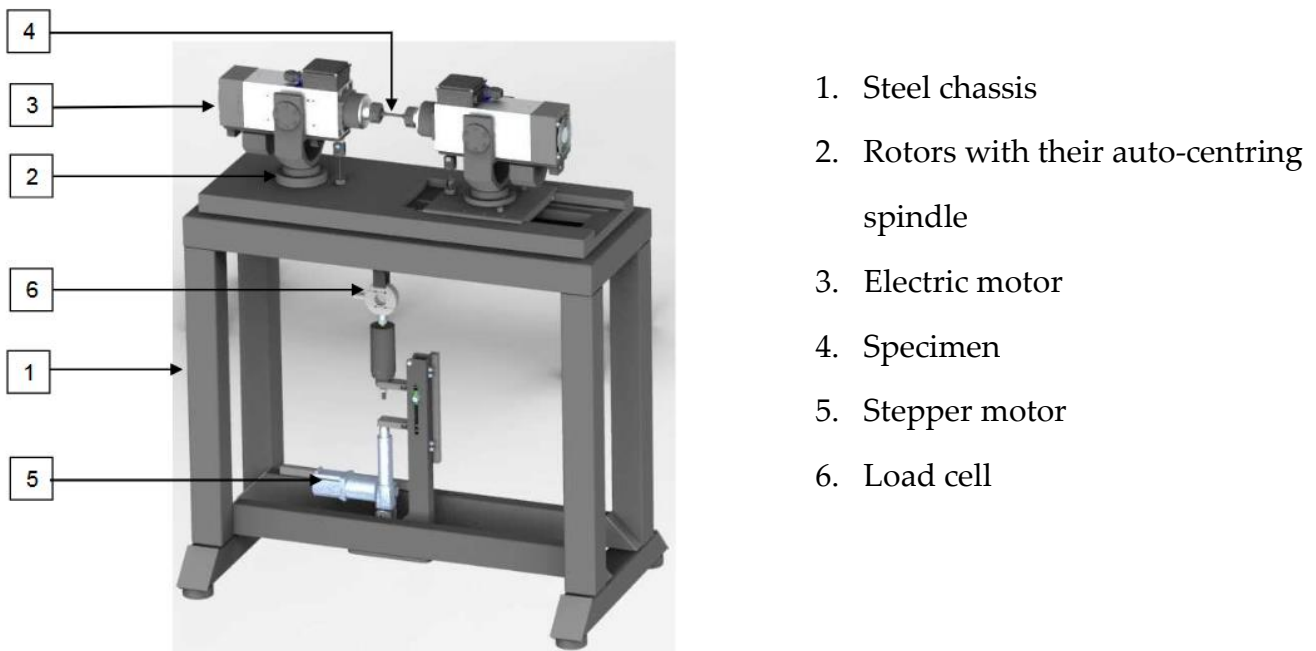


Figure 4.1 – Rotating bending machine

The rotating bending machine rotates and bends the specimen.

The specimen (100Cr6 or 100CrSiMn6-5-4) has a special design that creates a point of maximum stress at their midpoint rather than at their end. This gives a definite point of failure and avoids unwanted stress concentrations.

#### 4 – Experimental test

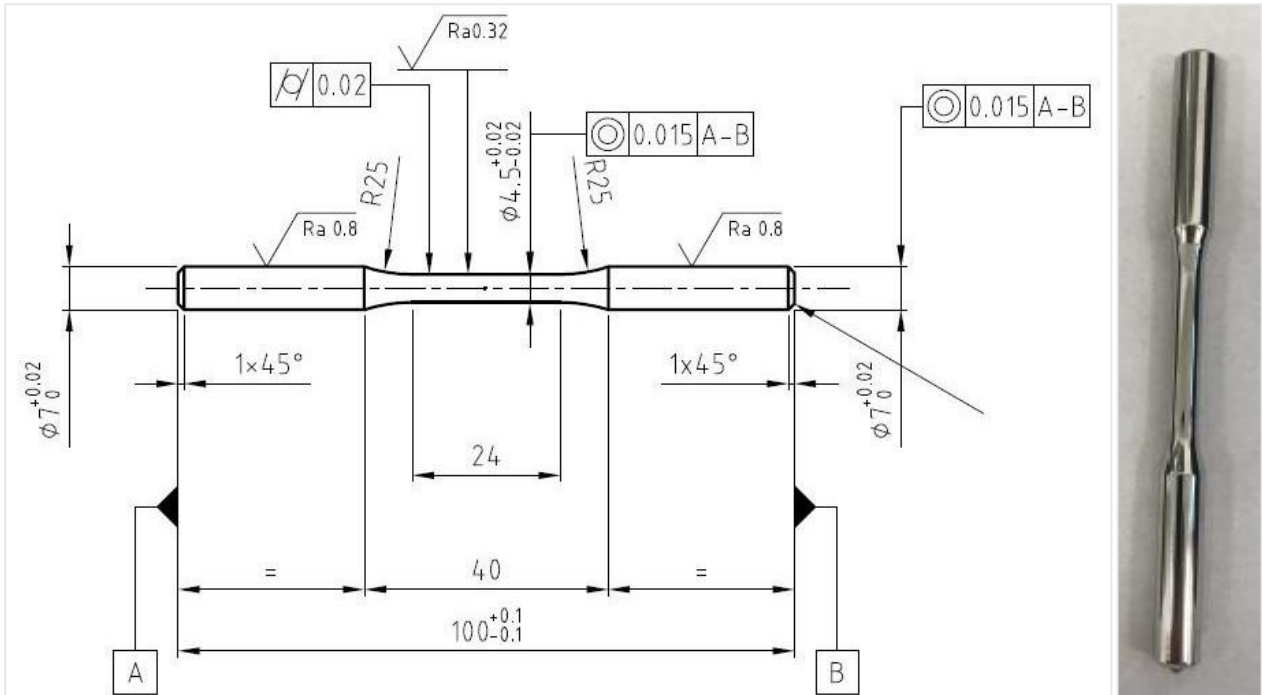


Figure 4.2-4.3 - Rotating bending specimen

Chemical composition 100Cr6								
Element	C%	Si%	Mn%	Ni%	Cr%	Mo%	Cu%	S%
%	0.97	0.23	0.29	0.08	1.43	0.013	0.05	0.003
Element	P%	Al%	As%	Sn%	Sb%	Pb%	Ti%	Ca%
%	0.014	0.025	<0.01	<0.01	0.002	0.001	0.001	<0.001

Table 4.1 – Chemical composition 100Cr6

Chemical composition 100CrSiMn6-5-4								
Element	C%	Si%	Mn%	Ni%	Cr%	Mo%	Cu%	S%
%	1.03	1.20	0.97	0.12	1.47	0.04	0.13	0.005
Element	P%	Al%	As%	Sn%	Sb%	Pb%	Ti%	Ca%
%	0.013	0.02	0.01	0.01	0.001	0.003	<0.001	<0.0005

Table 4.2 – Chemical composition 100CrSiMn6-5-4

Bending moment applied on the central section of the specimen is constant (Fig 4.5), since machine also puts in rotation the sample, normal stress of a point P changes (Fig 4.6) leading the specimen to a fatigue failure.

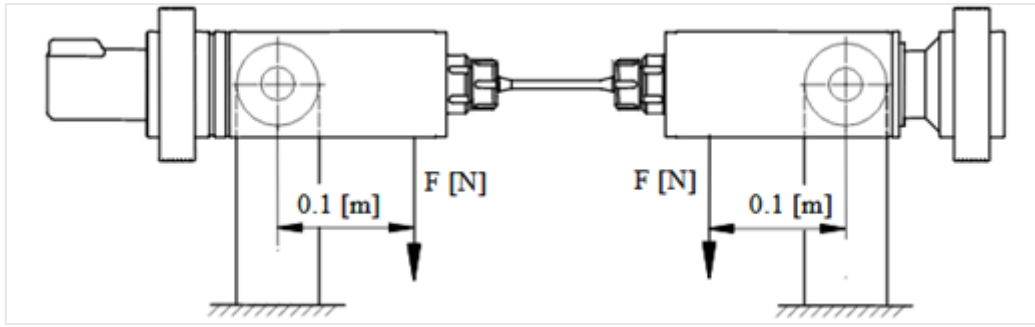


Figure 4.4 – Rotating bending machine scheme

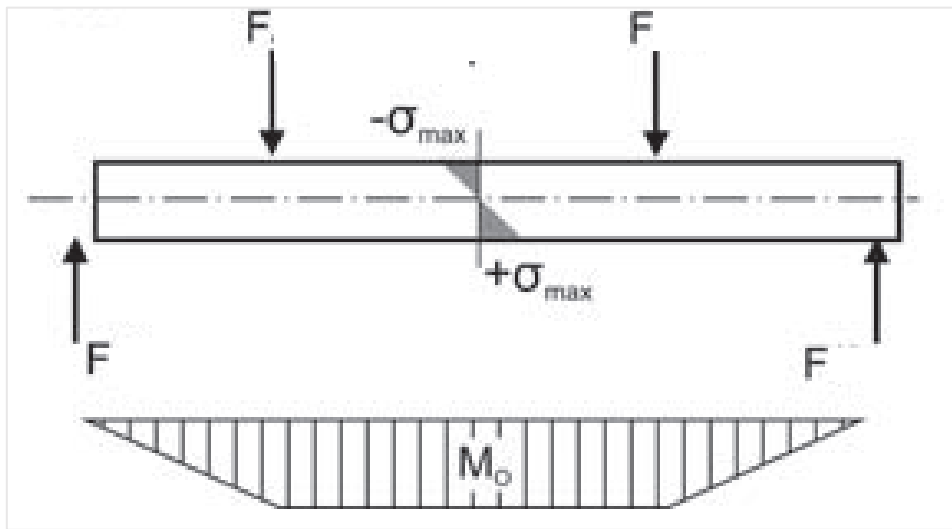


Figure 4.5 – Bending moment

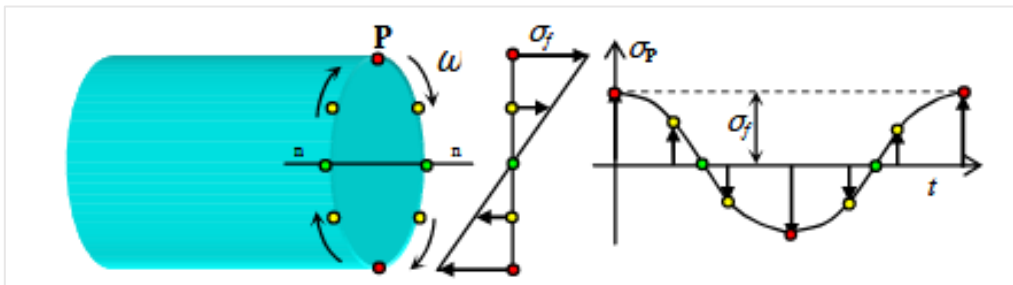


Figure 4.6 – Stress on point P as a function of time

### Testing condition

Method used for rotating bending test is a staircase methodology. It consists to subjecting the first specimen to a stress corresponding to the expected average fatigue strength. If the specimen survives  $5 \cdot 10^6$ , it is discarded and the next specimen is subjected to a stress that is one increment above the previous. When a specimen fails prior to reaching  $5 \cdot 10^6$  cycles, the obtained number of cycles is noted and the next specimen is subjected to a stress that is one increment below the previous. The increment  $\Delta\sigma$  is fixed before starting the test campaign. The load applied at the minimum cross section is controlled by a PC software, as the rotational speed.

## 4.2 Tension-tension testing machine

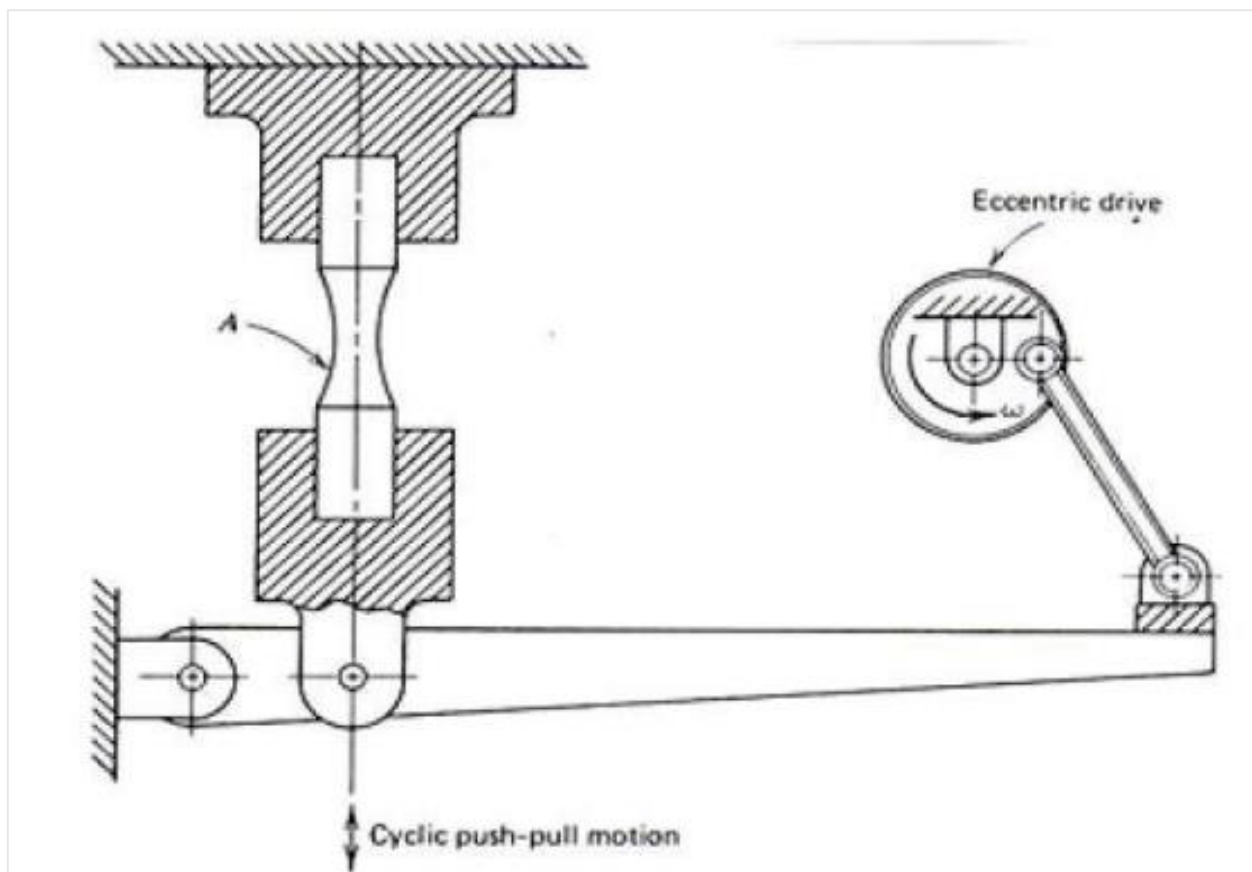


Figure 4.7 – Direct force fatigue testing machine (Collins 1981).

Axial fatigue testing machine subjects a test specimen to a uniform stress or strain through its cross section. In this type the specimen is exposed to pure axial (tensile or compressive) loading. Specimen is held at two ends and loaded cyclically between two extreme values (maximum and minimum), therefore normal stress changes over the time leading to a fatigue failure the specimen.

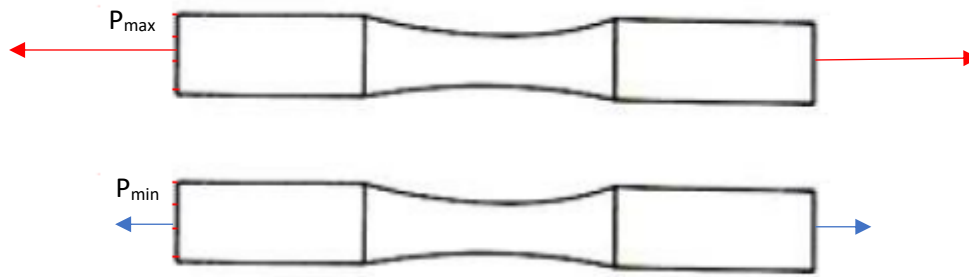


Figure 4.8 – Tension-tension test

### Testing condition

Axial fatigue tests were made in Argentina thanks to a collaboration between Tsubaki Nakashima Co., Ltd, Politecnico di Torino and Universidad de Buenos Aires. As a result it was possible to compare different steels and testing method.

Axial fatigue test was made to determine stress (S) against the number of cycles to failure (N) curve of two different steel composition. The data is obtained applying fixed stress amplitude to two or three specimens until failure. The procedure used is to test first series of specimens at a high peak stress where failure is expected in a fairly short number of cycles. The test stress is decreased for each succeeding series of samples until two specimens do not fail in the specified numbers of cycles, which is  $3 \cdot 10^6$  cycles. The highest stress at which specimens do not fail is taken as the fatigue threshold. Since the amplitude of the cyclic loading has a major effect on the fatigue performance, the S-N relationship is determined for one specific loading amplitude. The amplitude is express as the R ratio value, which is the minimum peak stress divided by the maximum peak stress. ( $R = \sigma_{min} / \sigma_{max}$ ).

In order to test various steels, two different specimens are used:



Figure 4.9 – Tension-tension specimens

- Grade A: Specimen Thickness 4,5mm; Sectional Area = 45 mm<sup>2</sup> Rm = 623 MPa; Rp<sub>0,2</sub> = 530 MPa.
- Grade B: Specimen Thickness 8mm; Sectional Area = 128 mm<sup>2</sup> Rm = 679 MPa; Rp<sub>0,2</sub> = 563 MPa.

Chemical composition Grade A										
Element	C %	Mn + Si %	P %	S %	Mo %	Al %	N (ppm)	Nb %	Ti %	V %
Max	0,1	2	0,1	0,01	0,04	0,1	100	0,1	0,5	0,1

Table 4.3 – Chemical composition Grade A

Chemical composition Grade B										
Element	C %	Mn + Si %	P %	S %	Mo %	Al %	N (ppm)	Nb %	Ti %	V %
Max	0,1	2	0,02	0,005	0,6	0,1	100	0,05	0,05	0,1

Table 4.4 – Chemical composition Grade B

### 4.3 Test rigs for bearing

The fatigue test of the balls was designed in order to single out the failure cause only on the tested balls without damaging the other parts of the bearing, like the inner ring, outer ring and cage. Zaretski [27] noted that balls components were responsible for 44.4 percent of the failures of the bearing, inner race 44.4 percent and outer-race 11.2 percent.

Test rigs (Fig 4.10) consist of electric motor (1), shaft (2), hydraulic piston (3), pneumatic piston (4), vent (5), accelerometer (6), thermocouple (7), protective shell (8), flange (9), command system (10) furthermore there is a computer that control the eight test rigs thanks to a dedicated software (Fig 4.11).

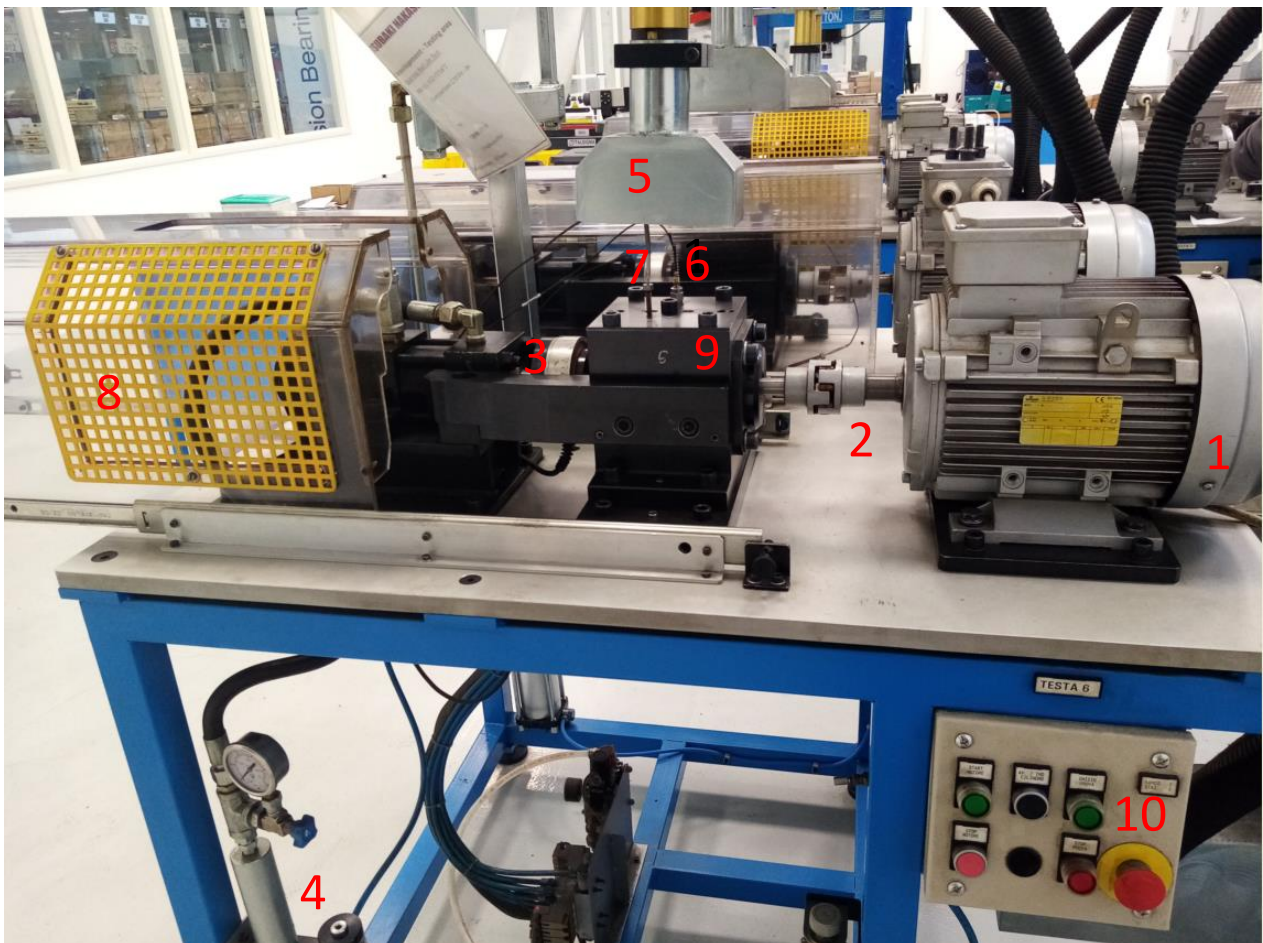


Figure 4.10 - Test rigs for bearing

The shaft is connected to the electric motor that transmit the rotation. A hydraulic piston driven by a pneumatic one, provides the axial load to the bearings. The loaded side of the shaft is the one with  $\phi 11.112\text{mm}$  balls, and the study is focused on those balls, not on the  $\phi 10.500\text{mm}$  ones, that have only a support function. Bearing is mounted on the shaft by interference fit and they are fixed to the structure thanks to the flange. The protective shell covers the shaft and the hydraulic piston allowing the operator to work safely on the others test rigs. A vent is located above the testing bearing to prevent overheating.



Figure 4.11 – Test rigs for ball bearing

The test bench is able to detect:

- Vibrations through an accelerometer
- Temperature through to a thermocouple
- Load level through to a load cell

Both the accelerometer and the thermocouple are placed on tested bearings (balls with  $\phi 11.112\text{mm}$ ). These two sensors are very important for the management of the test, indeed every variation of the nominal condition may have important consequences. For this reason, the three parameters display real time on the computer monitor connected with test rigs and for each minute of the test, temperature and vibrations are recorded.

- A high level of load may produce high pressure on balls that leads to premature failure
- A high temperature can arise due to excessive or limited lubricant, or a marked roundness of the balls and so excessive contact pressure
- A high level of vibrations may suggest a marked roundness of the balls or a failure of one of the bearing components.

The tested bearing mounts only one row of 7 balls (instead of 14 balls) to increase the contact pressure between the rings and the tested balls. Only one row is necessary since there's unidirectional load. Regarding the no-tested bearing, only one cage is assembled (as explained for the tested case) with a complete set of 15 balls.

### *Test procedure*

The test conditions are summarized below:

- Ball diameter:  $\phi 11.112\text{mm}$
- Ball material: 100Cr6
- Ball number in each test bearing: 7
- Ball number in each no-test bearing: 15
- Applied Load: 34400N
- Grease for tested balls: Shell Gadus S3 V220
- Grease for no tested balls: Shell Gadus S2 V100
- Load limit: 37500N
- Vibration limit: 15 mm/s<sup>2</sup>
- Temperature limit: 145 °C
- Shaft speed: 690 Rpm
- Life target: 200h

The test can start when the two bearings are mounted on the shaft and the bench is correctly assembled. During the firsts 10 minutes, the load is only the 30% of the nominal one to obtain a homogeneous distribution of the lubricant and the optimal centering of the shaft. After this short time, the load is raised until the nominal one. Each 20 hours the rigs are stopped and rings, lubricant, cages, and balls of the no-tested bearing are changed in order to prevent failures on different components of the bearing instead of the testing balls.

It is possible to have premature stops due to:

- **High temperature**

If the temperature overcomes 145 °C, the machine stops. This temperature was chosen because 150 °C is the tempering temperature of the steel, over this limit there is the possibility of microstructural changes (hardness reduction) of the rolling elements and then a reduction of fatigue life.

- **Load**

In order to prevent the overload, the test is stopped if the load limit is exceeded.

- **Vibrations**

When the vibrations level is higher than  $15\text{mm/s}^2$ , the machine stops. That level was chosen according to the testing developed experience: if a lower level is set, the machine would stop for external vibrations and if a higher level is set, a ball could be broken but the machine would not stop.

The test is considered finished in three cases:

- Failure of the tested balls.
- Excessive vibrations or temperature due to a marked roundness of the balls, test is considered failed.
- Life target is reached, test is considered survived.

## 4.4 Fracture inspection

### Stereomicroscope inspection

If the test finished because a ball failed a preliminary stereomicroscope inspection is made in order to better understand the origin of the fracture. If a microinclusion is found in the fracture area, also scanning electron microscope inspection is made.



Figure 4.12 - Stereomicroscope

## Scanning electron microscope

A scanning electron microscope (SEM) is a type of electron microscope that produces images of a sample by scanning the surface with a focused beam of electrons. The electrons interact with atoms in the sample, producing various signals that contain information about the surface topography and composition of the sample. Different elements produce different signals, therefore **chemical composition of inclusion is identified.**



Figure 4.13 – Scanning electron microscope

# Chapter 5

## 5 Eshelby model

The Eshelby model [15] allows to compute the stress field around an ellipsoidal inclusion. Eshelby showed that the strain field inside the ellipsoidal inclusion embedded in an infinite matrix is uniform when the inclusion is subject to a uniform eigenstrain. Eigenstrain refers to the stress-free deformation strain (of the free standing inclusion) associated with thermal expansion [30].

Applying a load to a region (inclusion) in an infinite homogeneous, isotropic and elastic medium (matrix), the inclusion undergoes a change of shape and size. Under the constraint of the matrix, the inclusion has an homogeneous strain. Eshelby [15] investigated the elastic fields assuming to cut a generic region and removing it from the matrix. In this way the region can change its shape, since it is unconstrained. Then, applying forces to the region and so restoring it to its original shape, put it back in the matrix. The applied surface tractions are integrated into a layer of body force distributed on the interface between matrix and inclusion. To complete the solution, this layer is removed by applying an equal and opposite layer of body force; the additional elastic field thus introduced is found by integration from the expression for the elastic field of a point force.

It results that if the inclusion is ellipsoidal and the matrix in which it is embedded is subjected to a homogeneous load, the stress within the inclusion is uniform. This means that the elastic stress and strain don't change with the position inside the inclusion.

Mura [17] defined an inclusion as a subdomain  $\Omega$  in a domain  $D$ . The eigenstrain  $\epsilon^*_{ij}(x)$  is given in  $\Omega$  and zero in  $D-\Omega$ . This is the inclusion problem, as the elastic modulus is the same for both subdomain and domain. The displacement  $u_i$ , strain  $\epsilon_{ij}$ , and stress  $\sigma_{ij}$  are expressed by [17]:

$$u_i(\mathbf{x}) = -C_{kjmn} \int_{\Omega} \epsilon^*(x') G_{ijk}(\mathbf{x} - \mathbf{x}') dx' \quad [5.1]$$

$$\epsilon_{ij}(\mathbf{x}) = -\frac{1}{2} \int_{\Omega} (C_{klmn} \epsilon^*_{min}(x') G_{ijk}(\mathbf{x} - \mathbf{x}') + G_{ijk}(\mathbf{x} - \mathbf{x}') dx' \quad [5.2]$$

$$\sigma(\mathbf{x}) = -C_{ijkl} \left( \int_{\Omega} (C_{pqmn} \epsilon^*_{min}(x') G_{kp,ql}(\mathbf{x} - \mathbf{x}') dx' + \epsilon^*_{kl}(x) \right) \quad [5.3]$$

where:

- $C_{ijkl}$  is the stiffness tensor
- $G_{ij}$  is Green's function
- $x$  is the position vector
- $x'$  denotes the position of a point source. A point source is a single identifiable *localised* source of something. A point source has negligible extent, distinguishing it from other source geometries. Sources are called point sources because in mathematical modeling, these sources can usually be approximated as a mathematical point to simplify analysis.

Since the strain and stress fields inside the inclusion are uniform:

$$\epsilon_{ij}(x) = S_{ijkl} \epsilon^*_{kl} \quad \text{for } x \in \Omega \quad [5.4]$$

with  $S_{kl}$  is the Eshelby tensor [16]

Regarding the strain field outside the inclusion:

$$\epsilon_{ij}(x) = S_{ijkl} \epsilon^*_{kl} \quad \text{for } x \in D - \Omega \quad [5.5]$$

Given this expression of the strain for both inside and outside the inclusion, the stress can be obtained as follows:

$$\sigma_{ij} = C_{ijkl} \epsilon_{kl}(x) \quad [5.6]$$

## 5.1 Equivalent inclusion method

If the elastic field that has to be evaluated is characterized by different elastic moduli, as the subdomain moduli is different from the one of the matrix, this makes the problem different. In this case the problem is called 'the inhomogeneity problem', while in the case of the same elastic modulus it is called 'the inclusion problem'. The correlation between the two was argued by Eshelby [15]: the stress perturbation due to the presence of an ellipsoidal inhomogeneity of an homogeneous applied stress  $\sigma^{\infty}_{ij}$ , can be determined by an inclusion problem when the eigenstrain  $\epsilon^*$  is chosen correctly. This is called the equivalent inclusion method [31].

Mura [17] gives the strain and stress fields as follows:

$$\epsilon_{ij} = \epsilon^{\infty}_{ij} + S_{ijmn} \epsilon^*_{mn} \quad [5.7]$$

$$\sigma_{ij} = \sigma^{\infty}_{ij} + C_{ijkl}(S_{klmn}\epsilon^*_{mn}) \quad \text{for } x \in \Omega \quad [5.8]$$

$$\epsilon_{ij}(x) = \epsilon^{\infty}_{ij} + D_{klmn}(x) \epsilon^*_{mn} \quad [5.9]$$

$$\sigma_{ij}(x) = \sigma^{\infty}_{ij} + C_{ijkl} D_{klmn}(x) \epsilon^*_{mn} \quad \text{for } x \in D - \Omega \quad [5.10]$$

Note that equations (5.7)(5.9) are similar to (5.4)(5.5) respectively, but the equations describing the equivalent inclusion method (5.7)(5.9) have the term  $\epsilon^{\infty}_{ij}$  which represents a remote strain induced by the homogeneous stress  $\sigma^{\infty}_{ij}$ . The same goes for the equations regarding the stress (5.8)(5.10), but here the eigenstrain is stress-free, so it has to be subtracted from the total strain when calculating the stress inhomogeneity.

## 5.2 Numerical solver

In order to evaluate the effects of various types of inclusions and matrices, a 3D numerical MATLAB solver that implement the Eshelby solution was used. In particular, it allowed to determine the stress field around the microinclusion. Healy [32] proposed a MATLAB code that was able to consider the Eshelby solution for an inclusion with semiaxes  $a_1 = a_2 \neq a_3$ . The one that was used in this work, allows to consider a general ellipsoidal inclusion or inhomogeneity with three different semiaxes, and it is based on the one developed by Meng et al. [31]. The code has been revisited to adapt it to the particular case of inclusions in ball bearings. As explained by Meng et al. [31], the main script, *incl prob.m* handles the input data structure, calls the Eshelby solver, *Esh sol.m*, and presents the results.

The input structure *incl prob.m* has attributions:

- $E_m$ : Young's modulus of the matrix
- $\nu_m$ : Poisson ratio of the matrix
- $E_h$ : Young modulus of the inhomogeneity
- $\nu_h$ : Poisson ratio of the inhomogeneity
- *dim*: the ellipsoidal dimensions  $a_i$
- *ang*: rotation angles around coordinate axes
- *stressvec*: remote stress  $\sigma^{\infty}_{ij}$
- *eigp*: initial eigenstrain  $\epsilon^p_{ij}$

- *grid*: observation grid(s) where we evaluate the solutions

where the stress and strain tensors are in the form of six-component vectors because of the symmetry. The *Esh\_sol.m* function reads the input data and output arguments, "*disp*", "*stress*" and "*strain*". The routines called by this function in the order of appearance:

- *Ctensord.m* constructs the stiffness tensors  $C_{ijkl}$  and  $C^*_{ijkl}$  for given elastic moduli ( $E_m$ ,  $\nu_m$ ) and ( $E_h$ ,  $\nu_h$ ). From the stress-strain correspondence, (4.6), it's possible to calculate the remote strain  $\epsilon^{\infty}_{ij}$  for the remote stress  $\sigma^{\infty}_{ij}$ . Note that if  $C_{ijkl} = C^*_{ijkl}$ ,  $\sigma^{\infty}_{ij} = 0$  and  $\epsilon_{Pij} \neq 0$ , it is the original inclusion problem.
- *Esh\_int.m* constructs the Eshelby tensor  $S_{ijkl}$  for a given  $\nu_m$  and ellipsoid dimension  $a_i$ . With  $C^*_{ijkl}$ ,  $\epsilon^{\infty}_{ij}$  and  $S_{ijkl}$  it's possible to calculate the fictitious eigenstrain  $\epsilon^*_{ij}$
- *Esh\_D4.m* constructs the tensor  $D_{ijkl}(x)$  for given  $\nu_m$ ,  $a_i$  and coordinates  $x_i$ . With  $D_{ijkl}$ , it's possible to calculate the exterior strain and stress.
- *Esh\_disp.m* constructs the displacements  $u_i$  for given  $\nu_m$ ,  $a_i$ ,  $x_i$ , and  $\epsilon^*_{ij}$
- *Esh\_D4\_disp.m* merges the functionalities of *Esh\_D4* and *Esh\_disp*. Since the objective is to find the stress field perturbation, only *Esh\_D4* routine is chosen, the displacement given by *Esh\_disp* it is not considered at this stage.

# Chapter 6

## 6 Ball frequency

In Chapter 3 it was shown that ball bearing life prediction  $L_{10}$  depend on four different parameters:

- The load-life exponent  $p$
- The dynamic load capacity  $C_d$
- The equivalent load  $P_{eq}$
- The bearing life factor  $LF_c$

$C_d$ ,  $p$  and  $LF_c$  are geometrical parameter, therefore the only parameter that depend on the presence of inclusion is  $P_{eq}$ .

Knowing how often the most critical inclusion will be stressed and the stress at the inclusion boundary, it is possible to define a new  $P_{eq}$ . The new  $P_{eq}$  is a weighted average between a theoretical load and the real load.

- Theoretical load is the fictitious load that it would be applied to a steel matrix without any inclusion, in order to produce the stress peak at the boundary of inclusion compute with eshelby model.
- Real load is the load applied to the bearing

It is important to better understand how a ball in bearing spins, in order to estimate how many times the inclusion will be stressed and in that case it is like it is applied the theoretical load instead the real load

## 6.1 Ball spin frequency

When a bearing spins, any defect or irregularities in the raceway surfaces or the rolling elements such as indentation, spalls, crack, flaking or irregularities in roundness of the rolling element, excites periodic frequencies called fundamental defect frequencies. A machine with a defective bearing can generate at least five frequencies [33]. These frequencies are:

- **Rotating unit frequency or speed ( $f$ ):** this is the frequency at which shaft on which bearing is mounted rotates.
- **Fundamental train frequency (FTF):** it is the frequency of the cage.
- **Ball pass frequency of the outer race (BPFO):** it is the rate at which the ball/roller contacts a defect in the outer race
- **Ball pass frequency of the inner race (BPFI):** it is the rate at which a ball/roller contacts a defect in the inner race.
- **Ball spin frequency (BSF):** it is the circular frequency of each rolling element as it spins. When one or more of the balls or rollers have a defect such as a spall the defect impacts both the inner and outer race each time one revolution of the rolling element is made.

In order to determine, statistically, how often the inclusion is loaded, the inclusion is considered like a fault so it possible to know the frequency with which the inclusion contacts the same race (inner or outer) [34]:

$$BSF = \frac{D}{2d} \left( 1 - \left( \frac{d}{D} \cos \phi \right)^2 \right)$$

- $BSF$  = ball spin frequency
- $D$  = pitch diameter
- $d$  = ball diameter
- $\phi$  = contact angle

$BSF$  provides the total number of cycles that ball element does during a complete shaft cycle. These are however the kinematic frequency assuming no slip, and in actual fact there must always be some slip.

## 6.2 Transversal slip

Since rolling without slipping is impossible, it is necessary to consider also other rotation of the balls; in this work only the transverse slip due to the motion of precession was considered [35].

Transverse slip could be calculated with the following geometrical consideration:

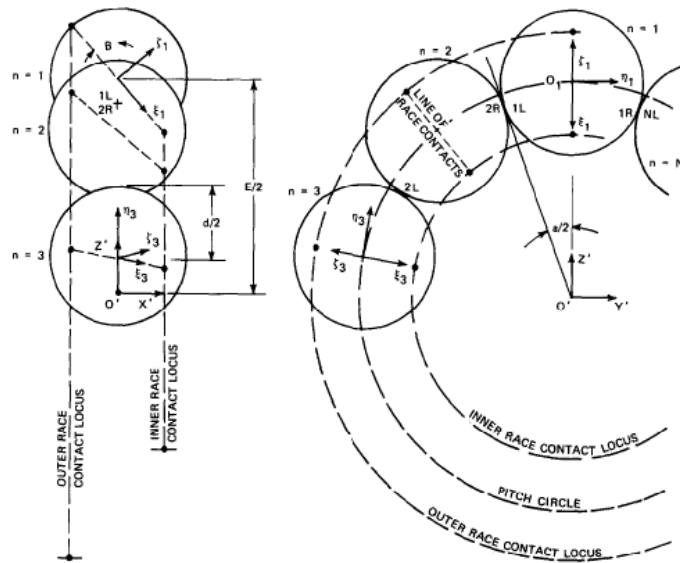


Figure 6.1 - Contact geometry. E.P. Kingsbury. "Precessional slip in angular contact ball bearing"

$O'X'Y'Z$  is the fixed reference system of the bearing,  $(O, \xi, \eta, \zeta)_n$  are reference systems centered one in each ball having  $(i, j, k)_n$  unit vectors.

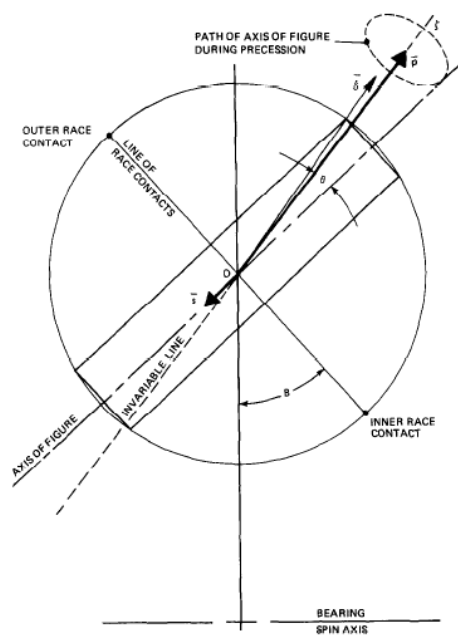


Figure 6.2 - Precession geometry. E.P. Kingsbury. "Precessional slip in angular contact ball bearing"

The angular velocity vector  $\hat{\delta}$  of any ball precessing in counter-rotation has two oblique components: spin  $s$  and precession  $p$ . These include the precession angle  $\alpha$ . The motion is specified with respect to  $(O, \xi, \eta, \zeta)$ , as a function of time  $t$  by:

$$\hat{\delta}_n = (s^* \sin \alpha \cos pt) i_n + (s^* \sin \alpha \sin pt) j_n + (p + s^* \cos \alpha) k_n$$

For the ball with  $n = 1$ , the radius vector to the ball-outer (ball-inner) contact is:

$$r_{b0i} = -(+) \frac{d}{2}$$

the surface velocities on the ball at these contacts are:

$$V_{B0i} = \hat{\delta} \times r_{b0i} = (s^* \sin \alpha \sin pt) j_1 + (p + s^* \cos \alpha) k_1$$

The radius vectors from  $O'$  to the ball-race contacts are:

$$r_{oi} = \frac{1}{2} * (D + d \cos \phi) (-\cos \phi i - \sin \phi k)$$

and the surface velocities on the races are:

$$V_{oi} = \gamma_{O'(i)} * r_{oi} = -\frac{1}{2} \gamma_{O'(i)} * (D + d \cos \phi) j_1$$

$\gamma_O$  = race angular velocity vector.

The ball-race slips, defined as race minus ball surface velocity, are:

$$V_{s0} = \frac{1}{2} (d(p + s^* \cos \alpha) - (D + d \cos \phi) \gamma_O) j_1 - \frac{d}{2} (s^* \sin \alpha \sin(pt)) k_1$$

$$V_{si} = \frac{1}{2} (d(p + s^* \cos \alpha) - (D - d \cos \phi) \gamma_O) j_1 + \frac{d}{2} (s^* \sin \alpha \sin(pt)) k_1$$

First-order bearing theory assumes zero slip in the rolling direction  $j$ , at each ball-race contact. For that condition:

$$\frac{\hat{\delta}}{\gamma_O - \gamma_i} = \frac{\hat{\delta}}{s} = \frac{D^2 - d^2 (\cos \phi)}{2Dd} = p$$

If there is precession, the definition of basic speed ratio can be generalized to:

$$p_p = \frac{p + s^* \cos \alpha}{s} = \frac{D^2 - d^2 (\cos \phi)}{2Dd}$$

$p$ ,  $s$  and  $\alpha$  are related by:

$$\frac{s}{p} = \frac{I_E - I_H}{I_E} \cos \alpha$$

where  $I_H$  and  $I_E$  are ball inertias along and normal to the axis.

The ratio of transverse slip amplitude to surface velocity, so while ball did a complete cycle around the principal axis also did a transverse slip that is around  $\frac{1}{100}$  of the complete cycle.

$$\frac{s \sin \alpha}{p+s \cos \alpha} \sim \frac{1}{100}$$

- $s$  = spin vector
- $p$  = precession vector
- $\alpha$  = precession angle

Bearings used are SKF BAHB-311396 B that have the following geometric parameters:

D [mm]	d [mm]	$\alpha$ [°]	$\phi$ [°]
56,5	11,112	10	28

Table 6.1 – Geometrical parameters of the bearing

It is possible to calculate how often the inclusion will be loaded:

BSF	Transversal slip/ shaft revolution	Shaft revolution/ transversal slip	Times when inclusion is stressed every 40 shaft revolution
2,46	0,0246	40	2

Table 6.2

Since inclusion is loaded two times during a complete rotation (inner race and outer race), the frequency with which there is a stress-riser inside the inhomogeneity is around every **20-shaft revolution**. The assumption that should be taken is that the transverse slip is not random but always in the same direction of rotation.

# Chapter 7

## 7 Statistics of extreme values method

Stress peak at the boundary of the inclusion does not depend on inclusion size however it is important to define a critical dimension, since large oxide inclusions are dangerous for most steel properties, and much more harmful than small inclusions. A critical inclusion size is usually defined, above which inclusions are dangerous and can cause the failure of steel products.

The purpose of the statistical theory of extreme values [36] is to mathematically and explain observed extremes in samples of some specified size, in our case the largest inclusion in a fixed volume and also the probability that in this volume an inclusion could be larger than critical size. This methodology has been applied in many fields relating to metals, Murakami and co-workers [12] were the first to apply this method to estimate the size of the maximum inclusion in a large volume or area of steel from data acquired on the polished surface. The basic concept of extreme value theory is that, when a fixed number of data points following a basic distribution are collected, the maximum and minimum of each of these sets also follow a distribution [37].

The distribution follows the following function [37]:

$$G(z) = e^{-e^{-\frac{z-\lambda}{\alpha}}} \quad (1)$$

where  $G(z)$  is the probability that the largest inclusion is no larger than size  $z$ , and  $\alpha$  and  $\lambda$  are the scale and location parameters. If the reduced variate,  $y$ :

$$y = \frac{z-\lambda}{\alpha} \quad (2)$$

is introduced, then from eq. (1) its distribution function is:

$$H(y) = e^{-e^{-y}} \quad (3)$$

## 7.1 Calculation procedure

In order to find the characteristic size of the maximum inclusion in a defined volume  $V$  you have to follow the written procedure below:

- 1) A standard inspection area  $S_0$  (mm<sup>2</sup>) is defined. The area of the maximum inclusion in  $S_0$  is measured, then the square root of the area of the maximum inclusion,  $(Area_{max})^{1/2}$ , is calculated. This is repeated for  $N$  areas  $S_0$ .
- 2) The values of  $(Area_{max,i})^{1/2}$  are classified, starting from the smallest, and ranked with  $i=1,2,\dots,N$ .
- 3) The cumulative probability of inclusion size  $z_i$  can be calculated:

$$H(y_i) = i / (N+1) \quad (4)$$

- 4) From eq. (3):

$$y_i = -Ln(-Ln(H(y_i))) \quad (5)$$

- 5) Define  $h$  like the mean value of  $(Area_{max,i})^{1/2}$ :

$$h = \frac{\Sigma(Areamax,i)^{1/2}}{N} \quad (6)$$

- 6) The standard inspection volume  $V_0$ :

$$V_0 = h * S_0 \quad (7)$$

- 7) The return period  $T$  is defined as:

$$T = V/V_0 \quad (8)$$

- 8) From equation 1 with  $G(z) = 1 - 1/T$ :

$$y(T) = -Ln(-Ln((T-1)/T)) \quad (9)$$

- 9) Plot  $(Area_{max,i})^{1/2}$  in terms of  $y_i$ , then draw the straight which best approximates the data points.

- 10) Find the intersection between  $y_i = y(T)$  and the straight which best approximates the data points. The abscissa of this point is the square root of the characteristic size of the maximum inclusion.

- 11) From eq. (2) and the experimental straight it possible to calculate  $\alpha$  and  $\lambda$ , then from eq. (1) the probability that the largest inclusion is no larger than critical size  $z$ .

## 7.2 Cleanliness analysis

Cleanliness analysis consist of microscopic inspection of a polish surface in order to find all the inclusions in a section area of raw material.

According to ASTM E45 [29] a microscopic method of examination is used, inclusions are assigned to a category based on similarities in morphology and not necessarily on their chemical identity.

Inclusions are characterized by size, shape, concentration, and distribution rather than chemical composition. Although compositions are not identified, Microscopic methods place inclusions into one of several composition-related categories:

- Sulfides
- Aluminates
- Silicates
- Oxides

Microscopic methods are used to characterize the size, distribution, number, and type of inclusion on a polished specimen surface. This may be done by examining the specimen with a light microscope and reporting the types of inclusion encountered, accompanied by a few representative photomicrographs. Standard reference charts depicting a series of typical inclusion configurations (size, type and number) were created for direct comparison with the microscopic field of view.

The minimum polished area of a specimen for the microscopic determination of inclusion content is 170 mm<sup>2</sup>.

Methods of specimen preparation must be such that a polished, microscopically flat section is achieved in order that the sizes and shapes of inclusions are accurately shown.

To obtain satisfactory and consistent inclusion ratings, the specimen must have a polished surface free of artifacts such as pitting, foreign material and scratches. When polishing the specimen, it is very important that the inclusion not be pitted, dragged, or obscured. Specimens must be examined in the as-polished condition, free from the effects of any prior etching (if used). Inclusion retention is generally easier to accomplish in hardened steel specimens than in the annealed condition. If inclusion retention is inadequate in annealed

specimens, they should be subjected to a standard heat treatment cycles using a relatively low tempering temperature. After heat treatment, the specimens must be descaled, and longitudinal plane must be reground and below any decarburization.

Sample is divided in standard inspection area. Every standard inspection area are examined in order to found non metallic inclusions.

### 7.3 Experimental data

A sample of steel 100Cr6 was chosen. It was divided in standard inspection area  $S_0$  (fig 7.1.)

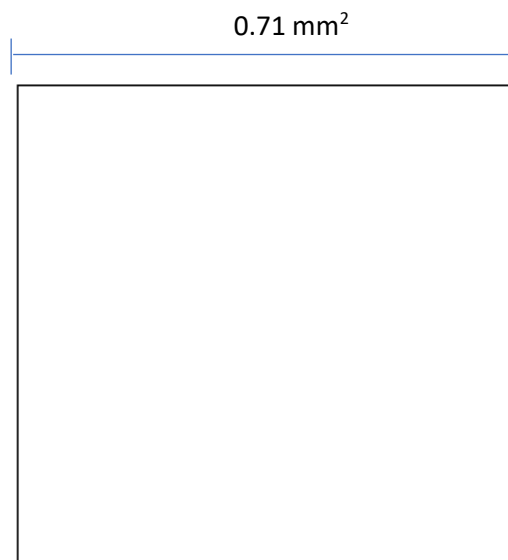


Figure 7.1 - Standard inspection area  $0.5 \text{ mm}^2$

After inspection 36 iclusions were found. They are listed in table 6.1

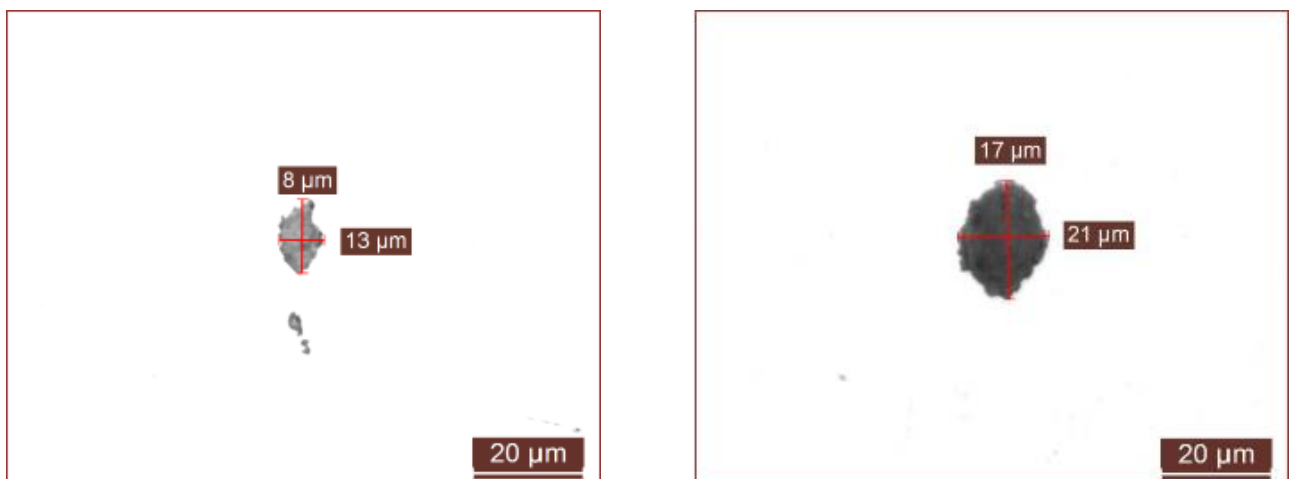


Figure 7.2-7.3 – Examples of inclusion found

Area <sub>max</sub> <sup>1/2</sup> [um]	H(y <sub>i</sub> )	y <sub>i</sub>
7,2	0,03	-1,28
7,9	0,05	-1,07
8,0	0,08	-0,92
8,4	0,11	-0,80
8,4	0,14	-0,69
8,5	0,16	-0,60
8,7	0,19	-0,51
8,8	0,22	-0,43
8,8	0,24	-0,35
8,9	0,27	-0,27
9,0	0,30	-0,19
9,3	0,32	-0,12
9,3	0,35	-0,04
9,7	0,38	0,03
9,7	0,41	0,10
9,7	0,43	0,18
11,1	0,46	0,25
11,1	0,49	0,33
11,7	0,51	0,41
12,0	0,54	0,49
12,6	0,57	0,57
12,7	0,59	0,65
12,8	0,62	0,74
13,3	0,65	0,84
13,7	0,68	0,94
13,9	0,70	1,04
14,2	0,73	1,15
14,6	0,76	1,28
15,5	0,78	1,41
15,5	0,81	1,56
16,7	0,84	1,73
16,8	0,86	1,93
19,5	0,89	2,17
21,7	0,92	2,47
23,0	0,95	2,89
23,5	0,97	3,60

Table 7.1 – Data collected after inspection

From data collected the following parameters were calculated:

V <sub>0</sub> [mm <sup>3</sup> ]	V [mm <sup>3</sup> ]	h [um]	N	T	Y(T)
6,2	267,79	12,4	36	42,9	3,75

Table 7.2 – Parameters used in Sev method

It was chosen a volume V of annulus bounded by external diameter of steel balls (11.112mm) and the depth threshold (800  $\mu\text{m}$ ) which the stress peak of inclusion remains below the maximum stress of the steel matrix.

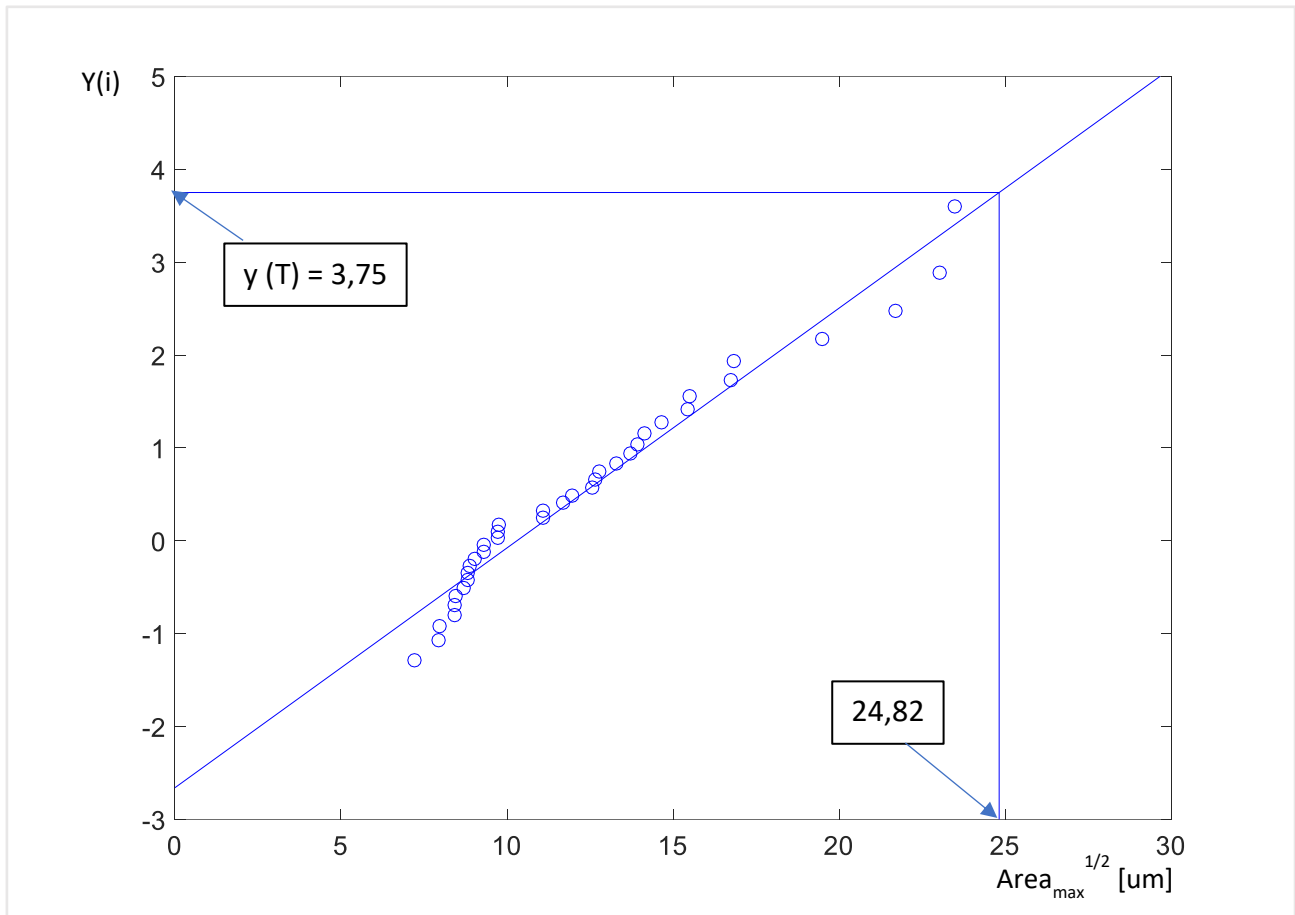


Figure 7.4 - Schematic illustration of the estimation of the maximum inclusion size in a large volume of steel by the SEV method.

- Slope of the approximates line =  $\frac{1}{\alpha} = 0.2582$
- Intersection between vertical axis and the approximates line =  $\frac{\lambda}{\alpha} = -2,658$
- $\text{Area}_{\text{max}} = 616 \text{ mm}^2$

In table 7.3 is interesting to see how the probability that the largest inclusion is no larger than a fixed  $\text{Area}_{\text{max}}^{1/2}$ , changes.

Fixed sizes used are 5,10,15,20 and 25  $\mu\text{m}$ .

$\text{Area}_{\text{max}}^{1/2} [\mu\text{m}]$	5	10	15	20	25
$G(\text{Area}_{\text{max}}^{1/2})$	2%	34%	74%	92%	98%

Table7.3 – Probability that the largest inclusion is no larger than a fixed  $\text{Area}_{\text{max}}^{1/2}$

# Chapter 8

## 8 Results

### 8.1 Raw Material results

Four different steel composition has been tested, two of them are low carbon content, the other two are high carbon content. Low carbon content steels have been tested with a tension-tension test instead the others with rotating bending test.

Testing different steels and using various methodology has enabled us to better understand the effect of non metallic inclusions with different conditions.

#### 8.1.1 Rotating bending test

Target of the test is to establish fatigue limit of the steel.

Before testing the two materials it was expected that 100CrSiMn6-5-4 would have better fatigue limit, in fact a high percentage of Silicon (Si) improves fatigue resistance. Contrary to the expectations test results showed that the fatigue limit of 100CrSiMn6-5-4 is lower than that of 100Cr6. After failure analysis displayed that **100CrSiMn6-5-4 has more critical inclusions than 100Cr6**, that is why fatigue limit is reduced.

Results of two different steel composition are shown below:

### *Campaign 1*

The test characteristics were:

- Material tested: 100Cr6 (AISI 52100)
- Stress frequency: 58.3Hz (3500 rpm)
- Life target:  $5 \cdot 10^6$  cycles
- Starting applied stress: 1100 MPa
- $\Delta\sigma = 25$  MPa

Test n.	Stress Applied to Minimum Cross Section [MPa]	Failed / Survived	Cycles [ $10^6$ ]	Test duration [h]
1	1100	F	1,24	5,9
2	1075	F	4,20	20,0
3	1050	F	1,06	5,1
4	1025	S	5,00	23,8
5	1050	F	3,11	14,8
6	1025	S	5,00	23,8
7	1050	S	5,00	23,8
8	1075	S	5,00	23,8
9	1100	F	4,00	19,0
10	1075	S	5,00	23,8
11	1100	S	5,00	23,8
12	1125	S	5,00	23,8
13	1150	F	1,73	8,2
14	1125	S	5,00	23,8
15	1150	S	5,00	23,8

Table 8.1 – Staircase 100Cr6

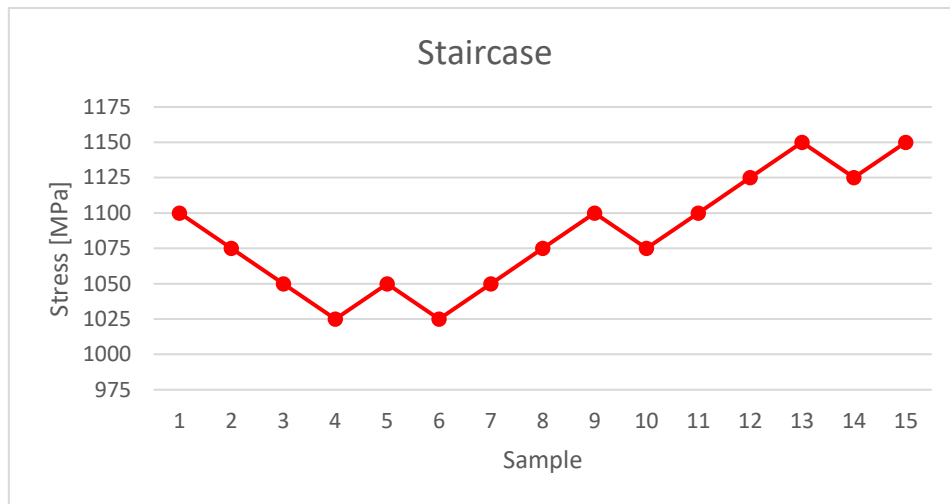


Figure 8.1 – Staircase 100Cr6

Fatigue limit obtained is  $1075 \pm 32.2$  MPa.

Visual inspection has been made on failed specimens, as expected in all the test the starting point is an inclusion just below the surface.

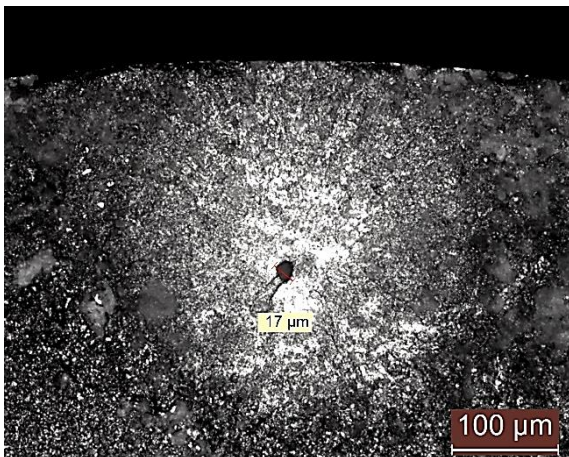


Figure 8.2 - Test n.1 – 1100 MPa – 200x

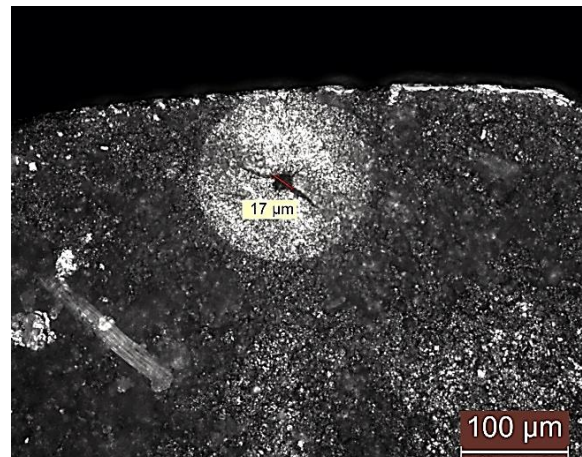


Figure 8.3 - Test n.2 – 1075 MPa – 200x

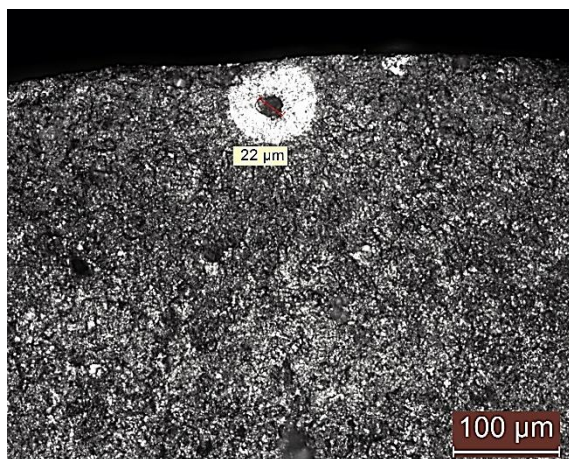


Figure 8.4 - Test n. 3 – 1050 MPa – 200x

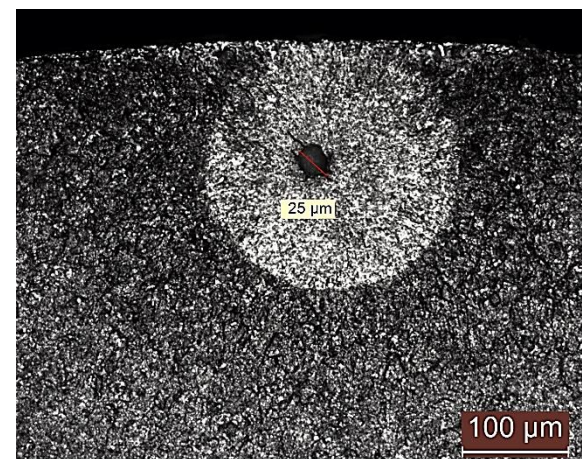


Figure 8.5 - Test n.5 – 1050 MPa – 200x

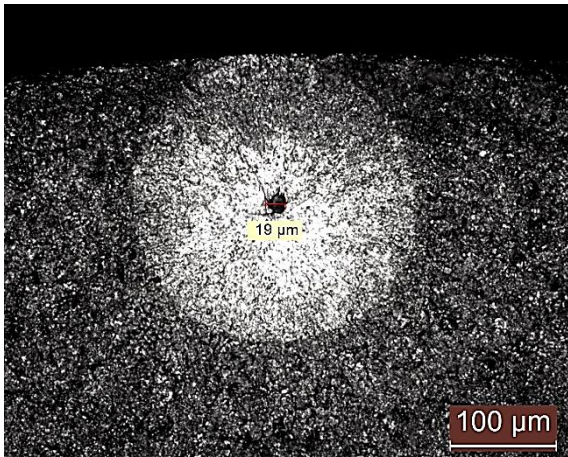


Figure 8.6 - Test n.9 – 1100 MPa - 100x

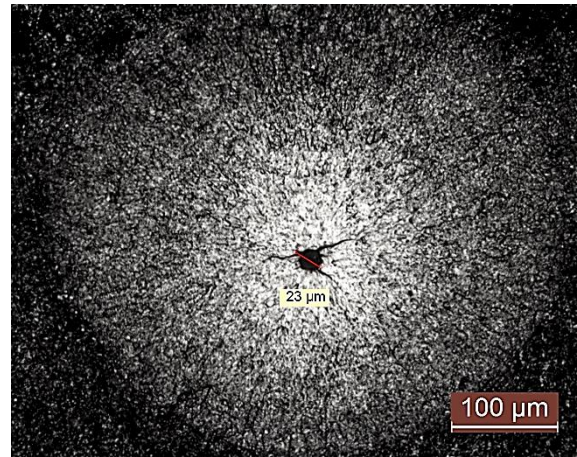


Figure 8.7 - Test n.13– 1150 MPa – 200x

## Campaign 2

The test characteristics were:

- Material tested: 100CrSiMn6-5-4
- Stress frequency: 58.3Hz (3500 rpm)
- Life target:  $5 \cdot 10^6$  cycles
- Starting applied stress: 1025 MPa
- $\Delta\sigma = 25$  MPa

Test n.	Stress Applied to Minimum Cross Section [MPa]	Failed / Survived	Cycles [ $10^6$ ]	Test duration [h]
1	1025	F	0,24	1,1
2	1000	S	5	23,8
3	1025	F	0,3	1,4
4	1000	F	0,05	0,3
5	975	S	5	23,8
6	1000	F	1,56	7,4
7	975	F	0,01	0,1
8	950	F	1,48	7
9	925	S	5	23,8
10	950	F	1,92	9,1
11	925	F	0,44	2,1
12	900	S	5	23,8
13	925	S	5	23,8
14	950	S	5	23,8
15	975	S	5	23,8

Table 8.2 – Staircase 100CrSiMn6-5-4

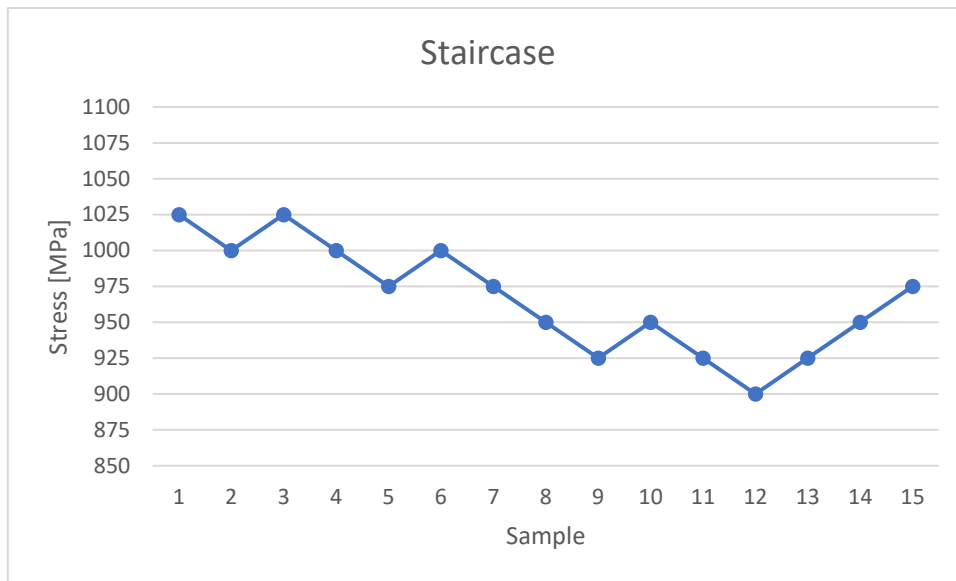


Figure 8.8 – Staircase 100CrSiMn6-5-4

Fatigue limit obtained is  $937.5 \pm 22.3$  MPa.

Visual inspection has been made on failed specimens, as expected in all the tests the starting point is an inclusion just below the surface.

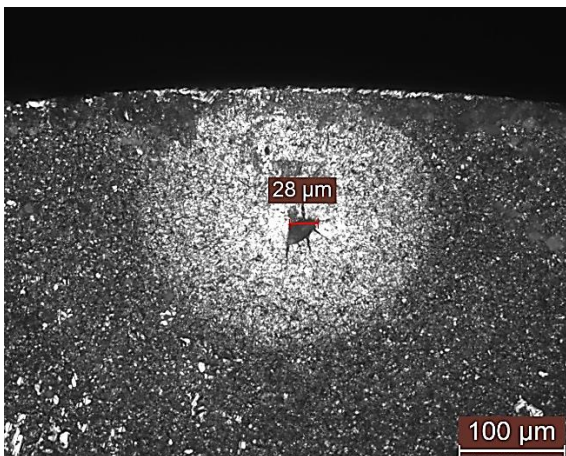


Figure 8.9 - Test n.1 – 1025 MPa – 200x

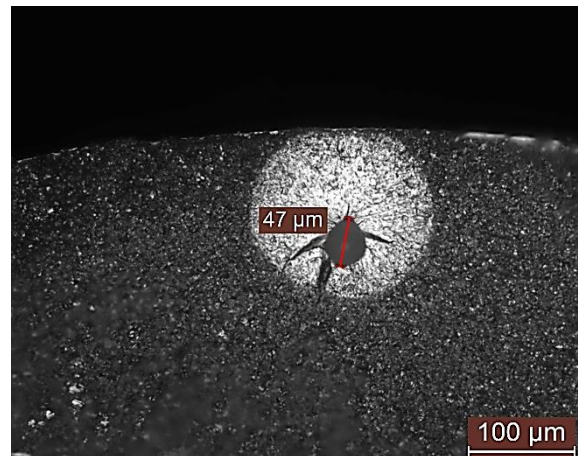


Figure 8.10 - Test n.3 – 1025 MPa – 200x

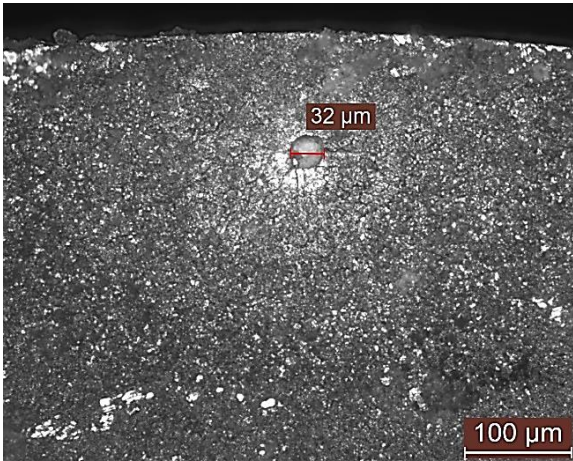


Figure 8.11 - Test n.4 – 1000 MPa – 200x

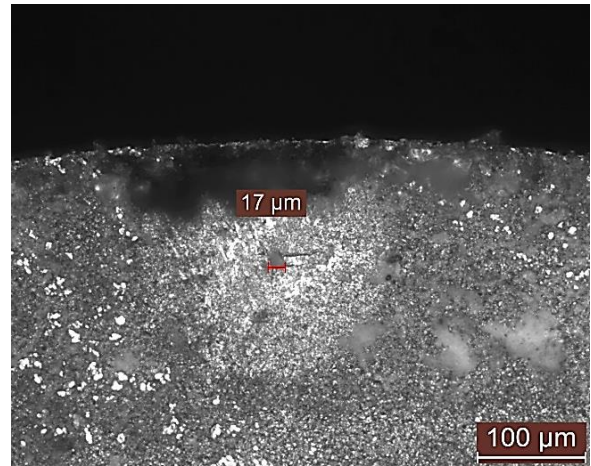


Figure 8.12 - Test n.6 – 1000 MPa – 200x

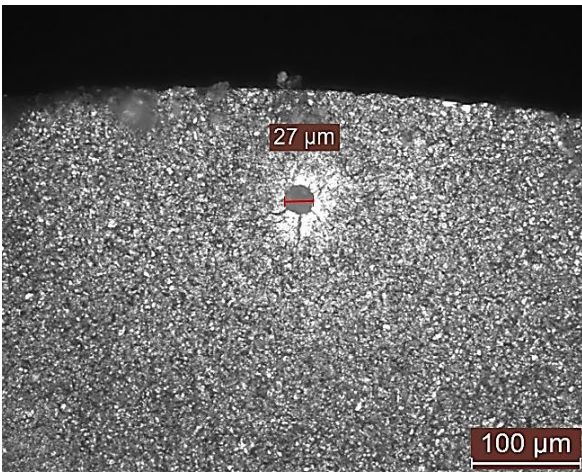


Figure 8.13 - Test n.7 – 975 MPa – 200x

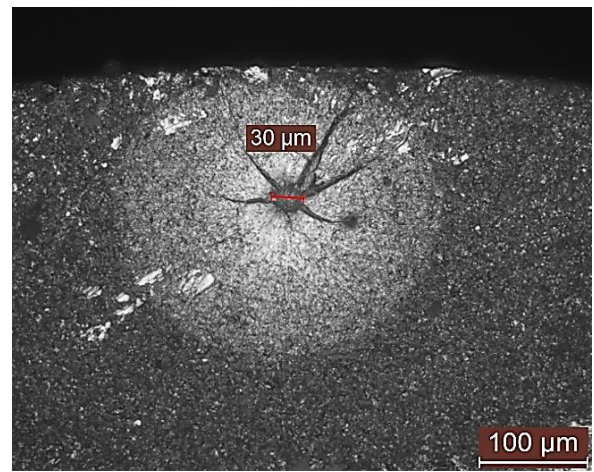


Figure 8.14 - Test n.8 – 950 MPa – 200x

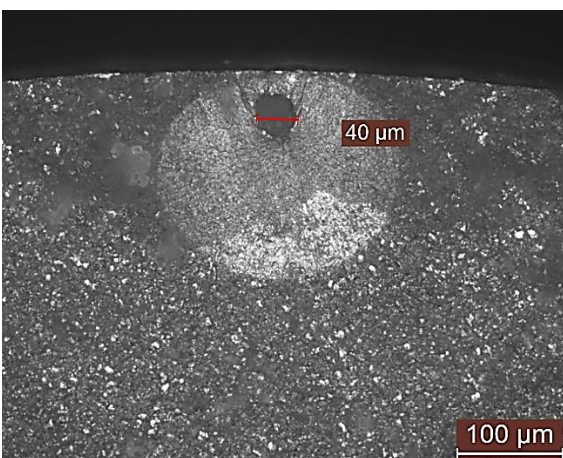


Figure 8.15 - Test n.10 – 950 MPa – 200x

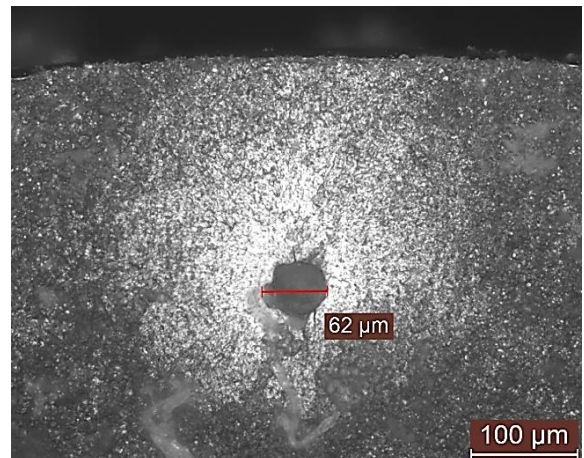


Figure 8.16 - Test n.11 – 925 MPa – 200x

## 8.1.2 Implementation of numerical model

Four Rotating bending specimens (two for each campaign) have been analysed with SEM inspection. The inclusion from which the fracture started, was composed by  $\text{Al}_2\text{O}_3$  plus other oxides for example calcium aluminate. It has to be noticed that when  $\text{Al}_2\text{O}_3$  was present, the Young modulus and the Poisson ratio were the ones of the  $\text{Al}_2\text{O}_3$  itself, since they are the most critical in this case and it's very difficult to determine the factors taking into account every element. The inclusions were all similar also in terms of dimensions and depth, and basically they can be approximated as circular.

### 100Cr6

Test 5: failed after  $3.11 \cdot 10^6$  cycles

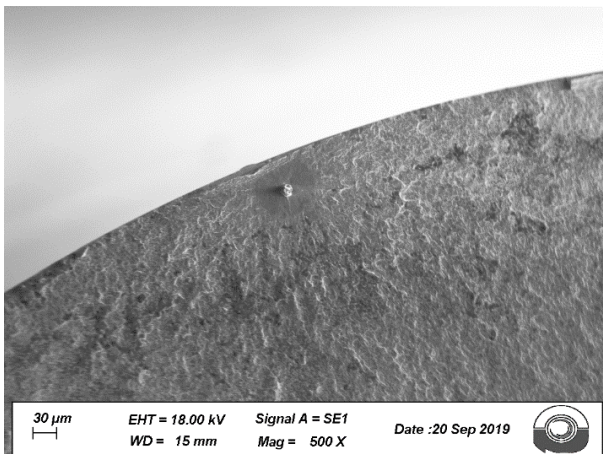


Figure 8.21 - Test n.5 – 500x

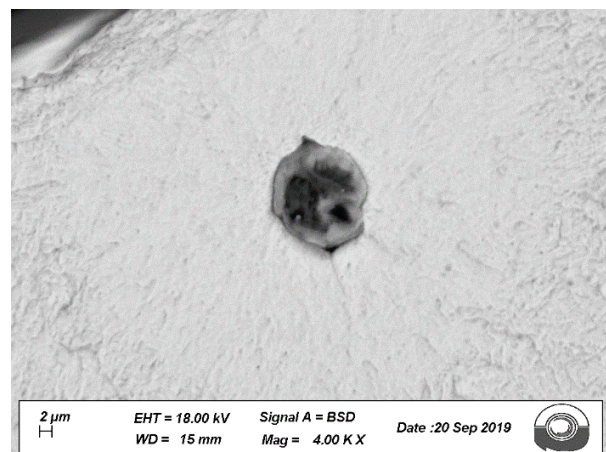


Figure 8.22 – Test n.5 – 4000x

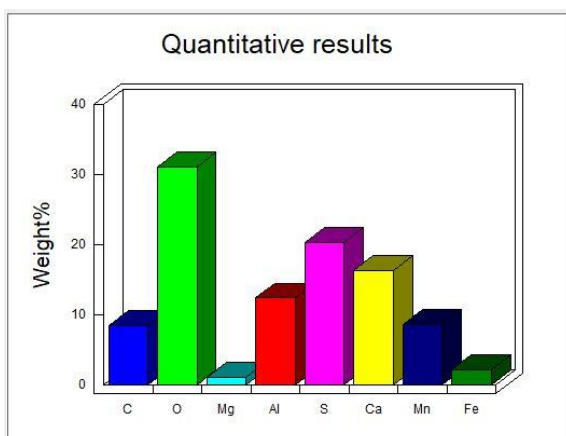


Figure 8.23 – Chemical composition of inclusion

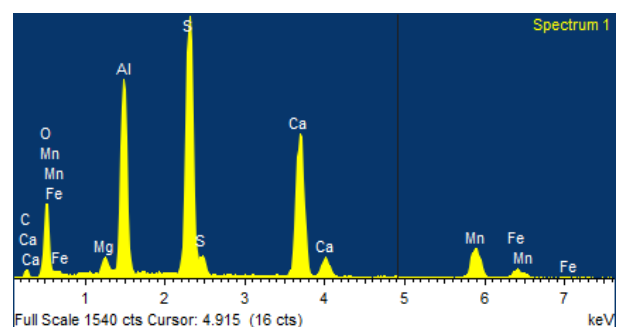


Figure 8.24 – Spectrum of inclusion

Stress applied [Mpa]	1050		
Original Stress at the depth of inclusion [MPa]	1025		
Maximum Stress at the depth of inclusion [MPa]	1268		
Inclusion dimension [ $\mu\text{m}$ ]	X	Y	Z
	12.5	12.5	12.5
Depth [ $\mu\text{m}$ ]	54		

Table 8.5 – Results

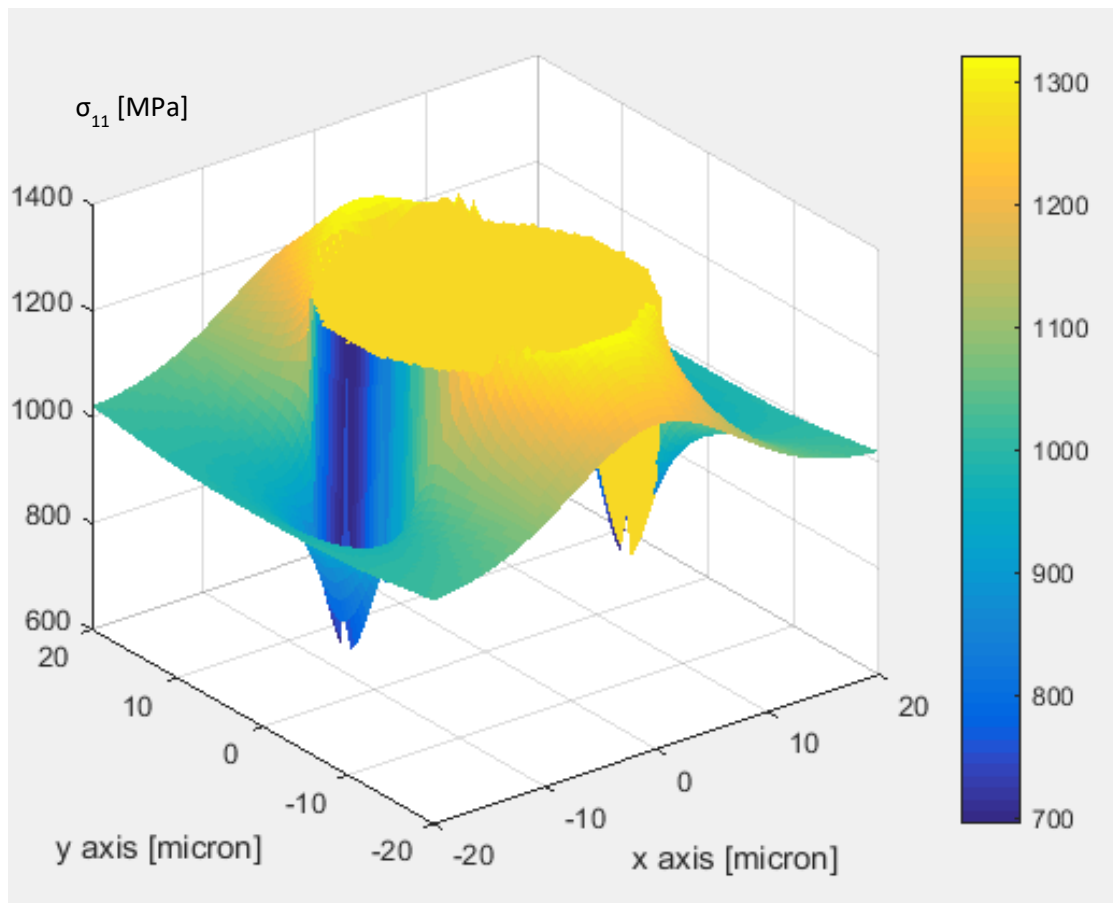


Figure 8.25 - Stress peak - Test n.5

Test 9: Failed after  $4 \times 10^6$

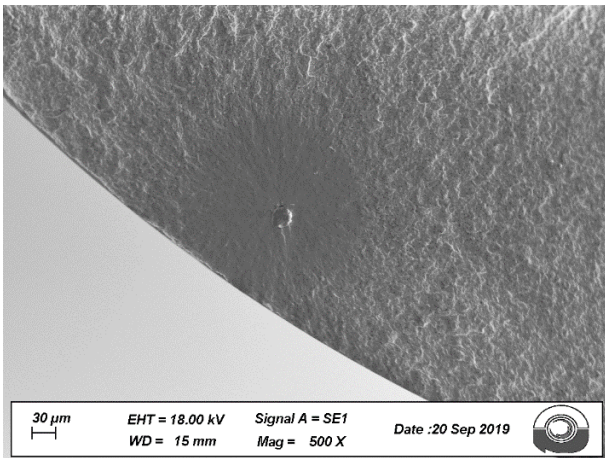


Figure 8.26 – Test n.9 – 500x

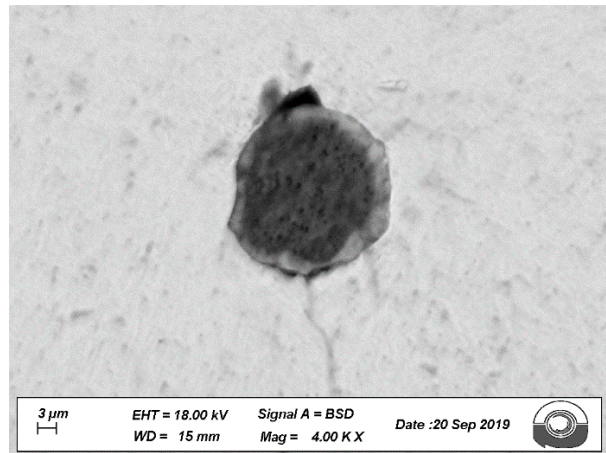


Figure 8.27 – Test n.9 – 4000x

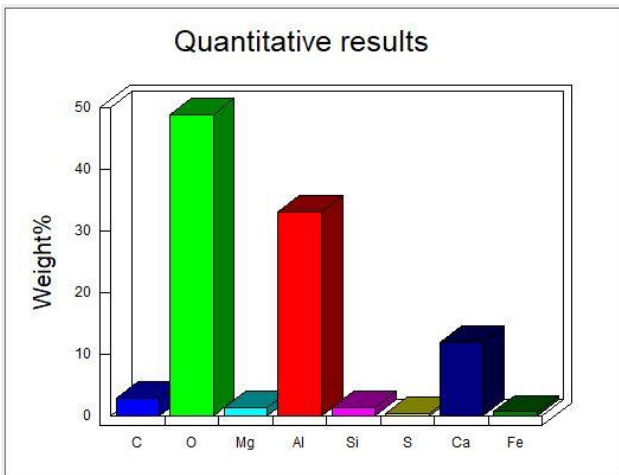


Figure 8.28 – Chemical composition of inclusion

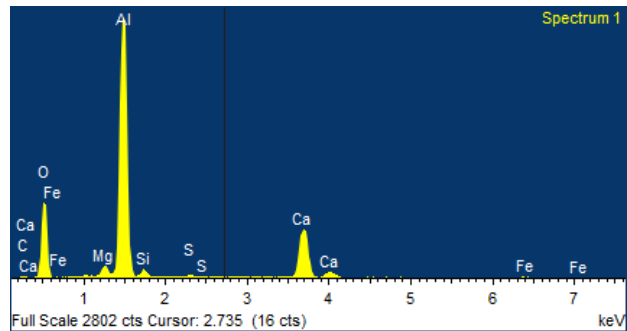


Figure 8.29 – Spectrum of inclusion

Stress applied [Mpa]	1100		
Original Stress at the depth of inclusion [MPa]	1038		
Maximum Stress at the depth of inclusion [MPa]	1284		
Inclusion dimension [ $\mu\text{m}$ ]	X	Y	Z
	9.5	9.5	9.5
Depth [ $\mu\text{m}$ ]	126		

Table 8.6 – Results

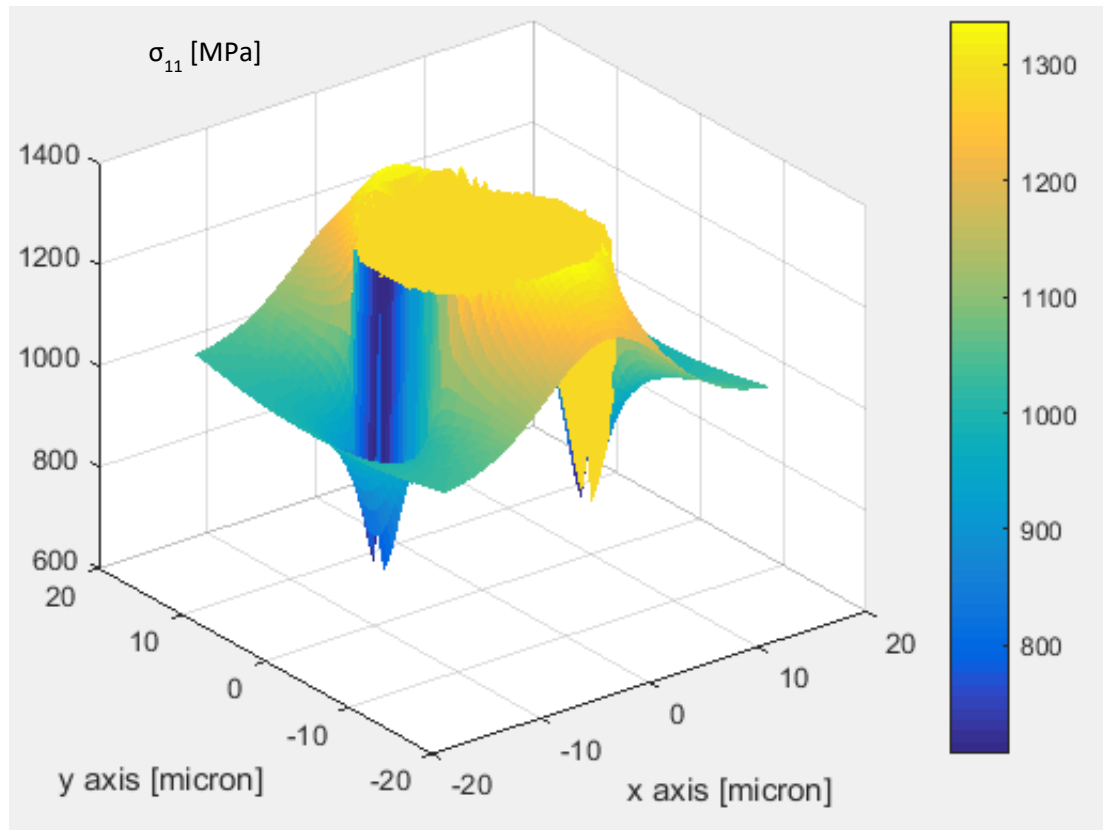


Figure 8.30 - Stress peak - Test n.9

100CrSiMn6-5-4

Test 3: Failed after  $0.3 \cdot 10^6$  Cycles

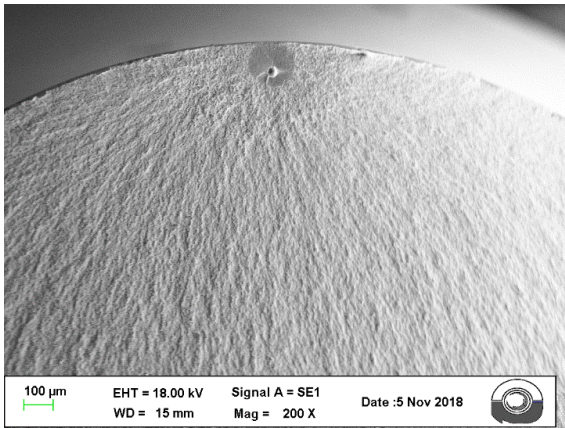


Figure 8.31 - Test n.3 – 200x

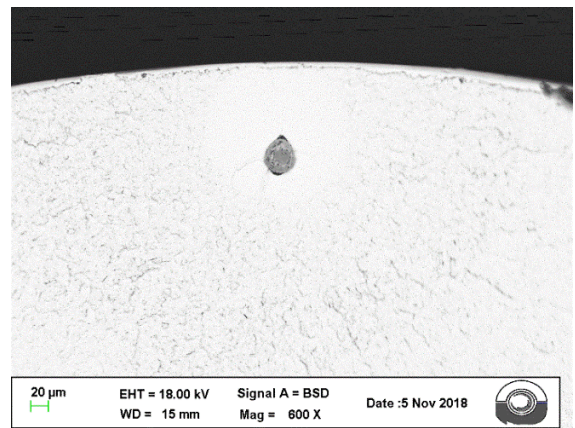


Figure 8.32 – Test n.3 – 600x

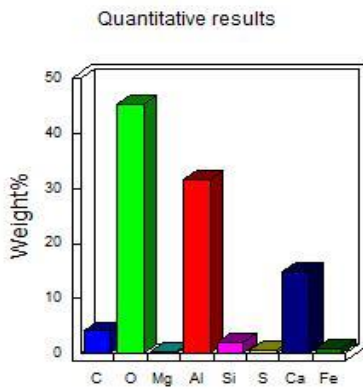


Figure 8.33 – Chemical composition of inclusion

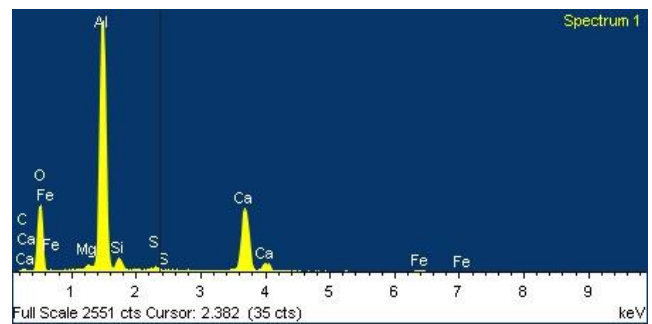


Figure 8.34 – Spectrum of inclusion

Stress applied [Mpa]	1025		
Original Stress at the depth of inclusion [MPa]	979		
Maximum Stress at the depth of inclusion [MPa]	1211		
Inclusion dimension [ $\mu\text{m}$ ]	X	Y	Z
	23.5	23.5	23.5
Depth [ $\mu\text{m}$ ]	100		

Table 8.7 – Results

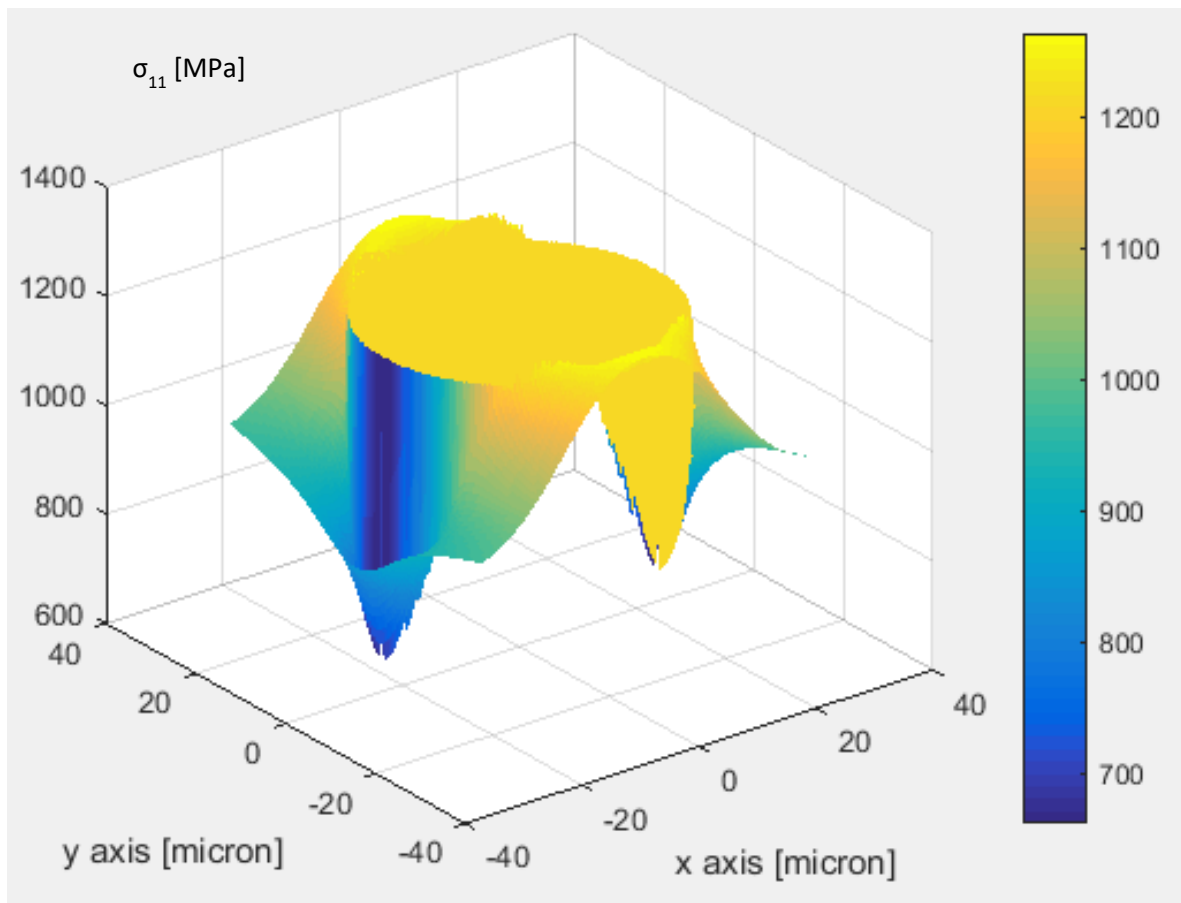


Figure 8.35 - Stress peak - Test n.3

Test 11: Failed after  $0.44 \cdot 10^6$  Cycles

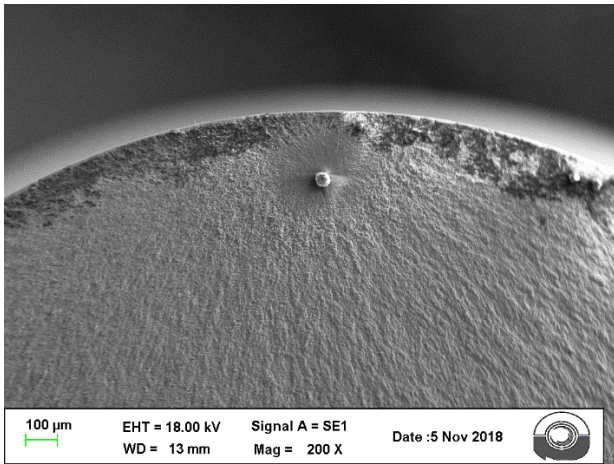


Figure 8.36 - Test n.11 – 200x

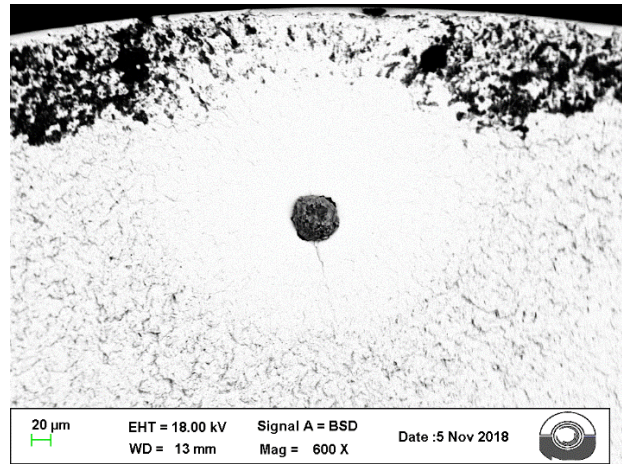


Figure 8.37 – Test n.11 – 600x

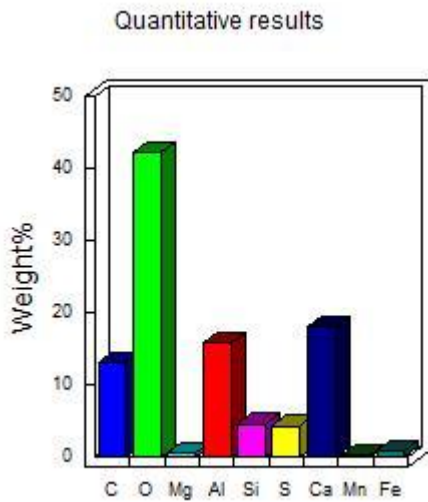


Figure 8.38 – Chemical composition of inclusion

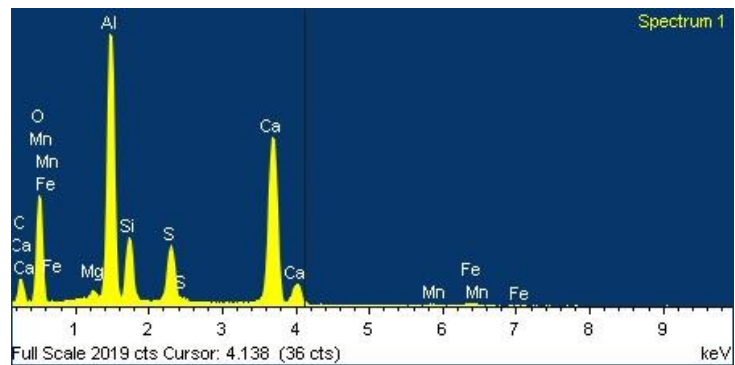


Figure 8.39 – Spectrum of inclusion

Stress applied [Mpa]	925		
Original Stress at the depth of inclusion [MPa]	832		
Maximum Stress at the depth of inclusion [MPa]	1134		
Inclusion dimension [ $\mu\text{m}$ ]	X	Y	Z
	31	31	31
Depth [ $\mu\text{m}$ ]	227		

Table 8.8 – Results

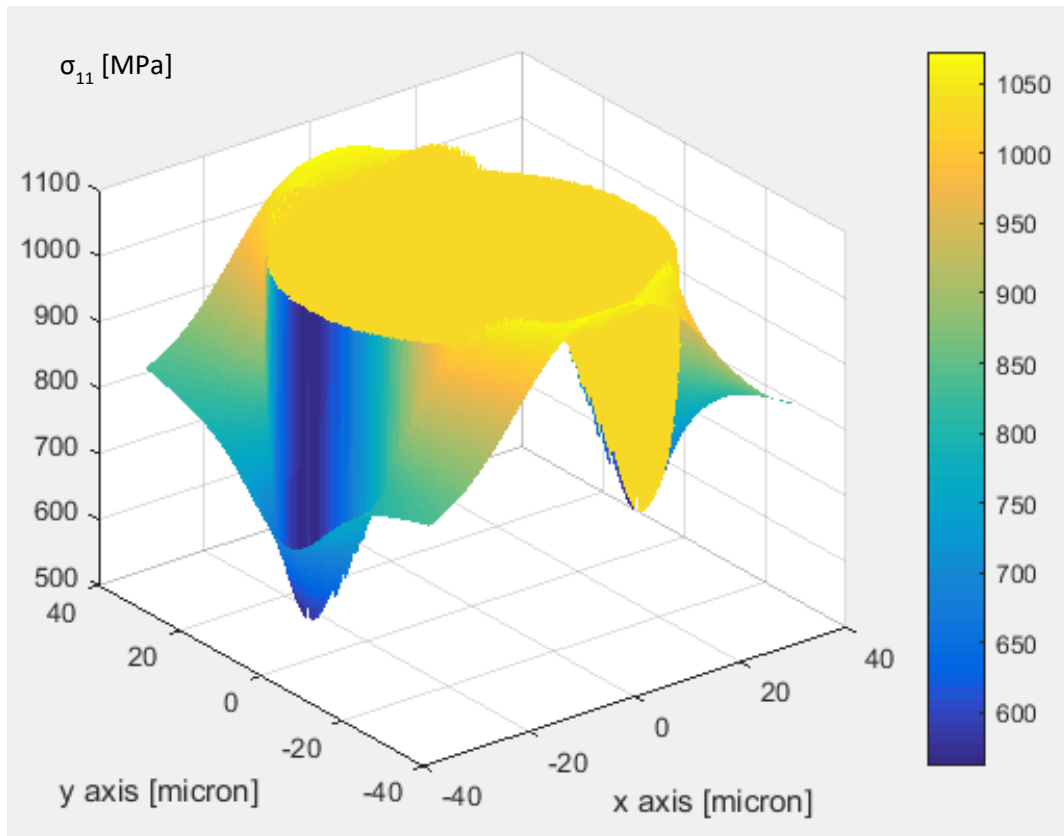


Figure 8.40 - Stress peak - Test n.11

## 8.2 Tension-tension test

Target of the test is to establish fatigue limit of the steel. Before testing the two materials it was expected that Grade B would have better fatigue limit, in fact a higher percentage of Molybdenum (Mo) improves fatigue limit. Results obtained are in agreement with expectation, in fact, differently to rotating bending tests, no critical inclusions have been identified as starting point.

Results of the two different steel composition are shown below:

### Campaign 1

The test characteristics were:

- Material tested: Grade A
- Starting maximum applied stress: 609.7 MPa
- $R = 0.1$
- Stress frequency: 15Hz
- Life target:  $3 \cdot 10^6$  cycle

Test	$\sigma_{\max}$ [Mpa]	$\sigma_{\min}$ [Mpa]	$\sigma_a$ [Mpa]	Cycles to Failure [ $10^6$ ]	Test duration [h]	F/S
1	609,7	60,97	274,37	0.04	0,08	F
2	609,7	60,97	274,37	0.06	0,12	F
3	583,2	58,32	262,44	0.4	0,74	F
4	524,9	52,49	236,21	0.11	2,07	F
5	524,9	52,49	236,21	0.17	3,11	F
6	524,9	52,49	236,21	0.19	3,44	F
7	514,3	51,43	231,44	0.25	4,67	F
8	514,3	51,43	231,44	0.27	5,08	F
9	514,3	51,43	231,44	0.34	6,29	F
10	498,4	49,84	224,28	0.31	5,80	F
11	498,4	49,84	224,28	0.36	6,61	F
12	498,4	49,84	224,28	0.43	7,97	F
13	498,4	49,84	224,28	3	55,56	S
14	487,8	48,78	219,51	0.55	10,14	F
15	487,8	48,78	219,51	0.58	10,77	F
16	487,8	48,78	219,51	0.64	11,87	F
17	477,2	47,72	214,74	0.48	8,84	F
18	477,2	47,72	214,74	0.76	14,04	F
19	477,2	47,72	214,74	2.06	38,14	F
20	466,5	46,65	209,93	3	55,56	S
21	466,5	46,65	209,93	3	55,56	S
22	466,5	46,65	209,93	3	55,56	S

Table 8.3 – S-N Grade A

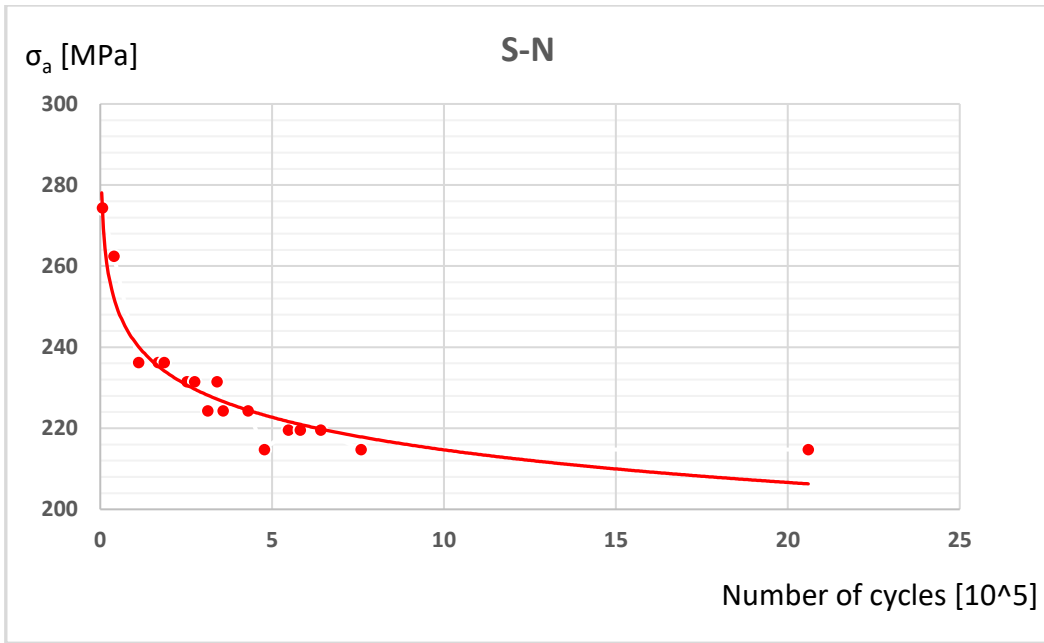


Figure 8.17 – S-N curve Grade A

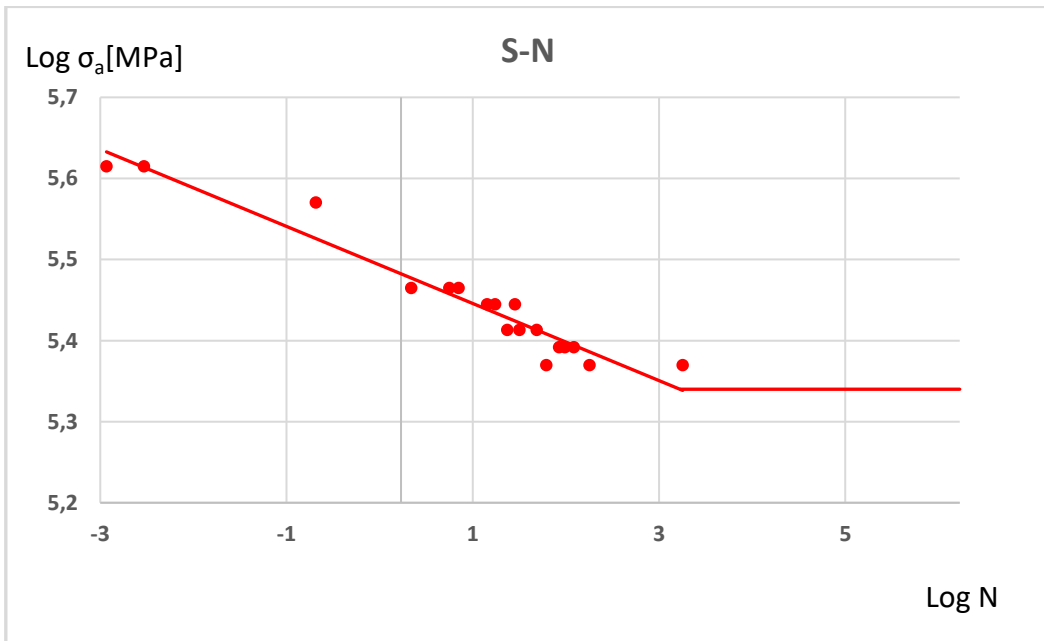


Figure 8.18 – Log S-N curve Grade A

Fatigue limit obtained is **210 MPa**.

**Campaign 2**

The test characteristics were:

- Material tested: Grade B
- Starting maximum applied stress: 609.7 MPa
- $R = 0.1$
- Stress frequency: 15Hz
- Life target:  $3 \cdot 10^6$  cycles

Test	$\sigma_{\max}$ [Mpa]	$\sigma_{\min}$ [Mpa]	$\sigma_a$ [Mpa]	Cycles to Failure [ $10^6$ ]	Test duration [h]	f/s
1	608,4	60,84	273,78	0.1	1,92	F
2	608,4	60,84	273,78	0.14	2,58	F
3	608,4	60,84	273,78	0.21	3,93	F
4	597,1	59,71	268,70	0.17	3,07	F
5	597,1	59,71	268,70	0.18	3,42	F
6	597,1	59,71	268,70	0.21	3,95	F
7	585,9	58,59	263,66	0.2	3,75	F
8	585,9	58,59	263,66	0.2	3,76	F
9	585,9	58,59	263,66	0.21	3,98	F
10	574,6	57,46	258,57	0.28	5,13	F
11	574,6	57,46	258,57	0.31	5,78	F
12	574,6	57,46	258,57	0.65	11,99	F
13	563,3	56,33	253,49	0.38	6,95	F
14	563,3	56,33	253,49	0.42	7,81	F
15	563,3	56,33	253,49	3	55,56	S
16	552,1	55,21	248,45	0.22	4,12	F
17	552,1	55,21	248,45	0.48	8,91	F
18	552,1	55,21	248,45	3	55,56	S
19	540,8	54,08	243,36	3	55,56	S
20	540,8	54,08	243,36	3	55,56	S
21	540,8	54,08	243,36	3	55,56	S

Table 8.4 – S-N Grade B

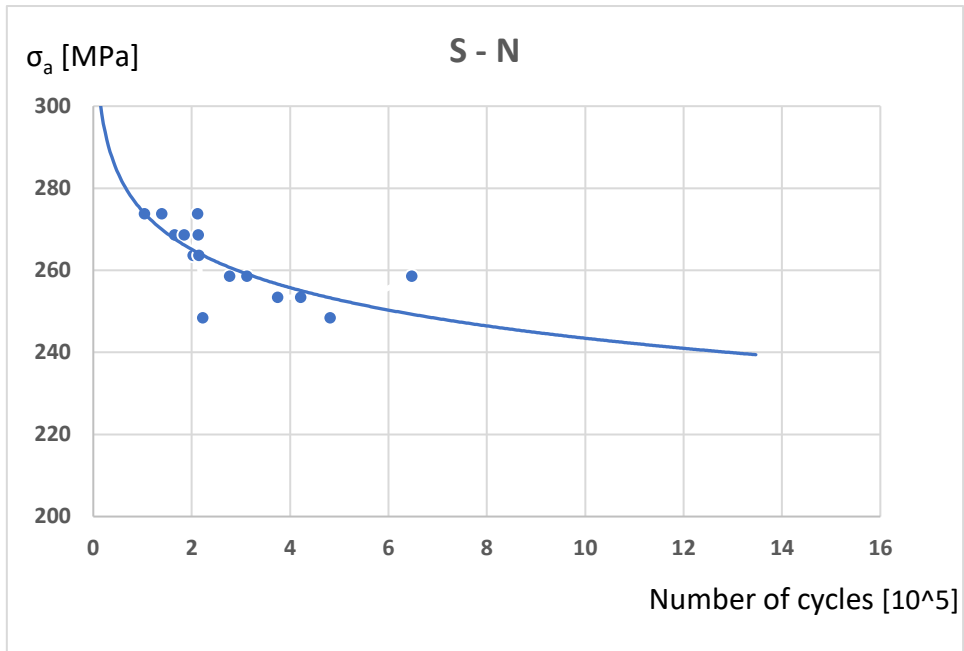


Figure 8.19 – S-N curve Grade B

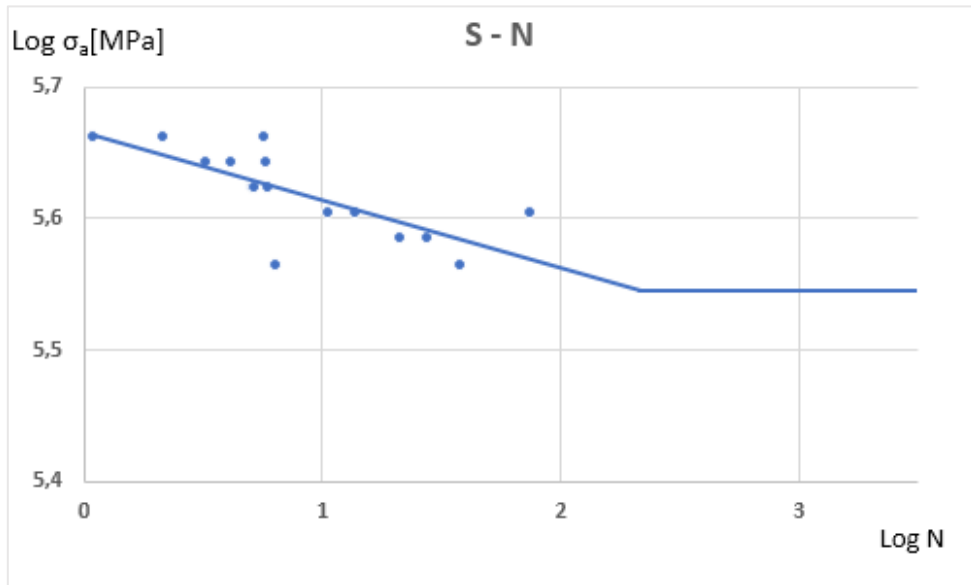


Figure 8.20 – Log S-N curve Grade B

Fatigue limit obtained is **243 MPa**.

## 8.2.1 Cleanliness analysis

Sem analysis were made on test 4,9,14,17 and 19 for Grade A and on test 1,5,7,11 and 13 for Grade B in order to evaluate the effect of fatigue and the presence of non metallic inclusions for different number of cycles.

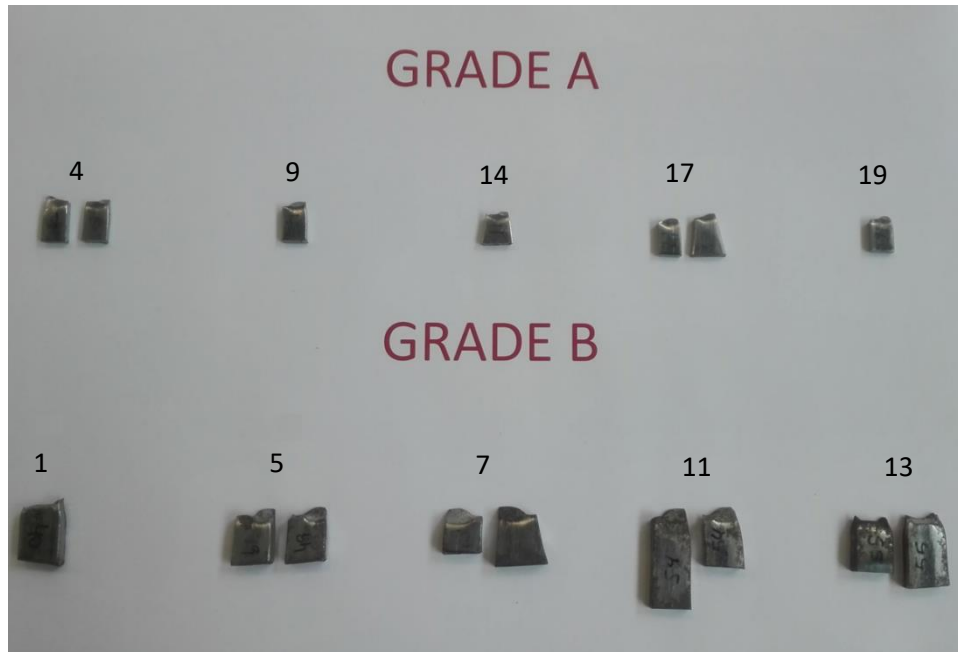


Figure 8.41 – Tension-tension specimens

No critical inclusions were found, nevertheless flakes of non metallic materials were found near the starting points in some specimens (Fig 7.54-7.55-7.56-7.57). It is impossible to say that these inhomogeneities are the cause of the failure but they may have contributed to increase the stress and leading to crack.

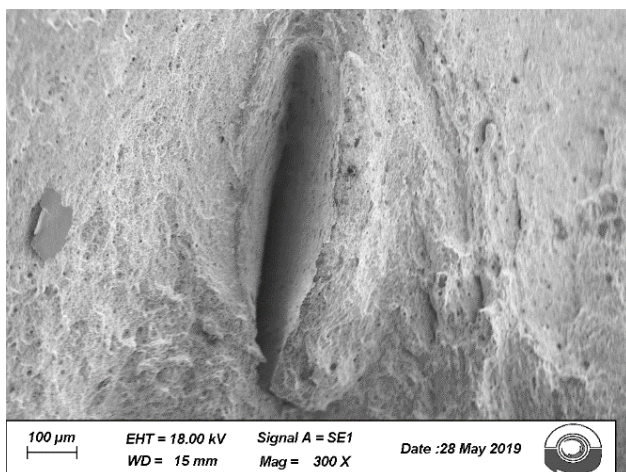


Figure 8.42 – Test 4 – Starting point 300x

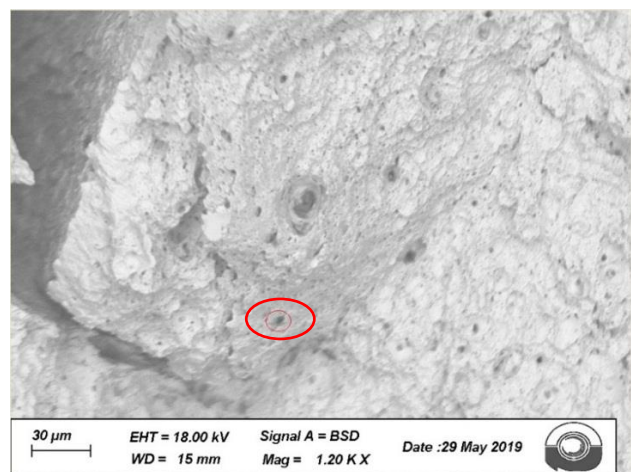


Figure 8.43 - Test 4 – Starting point 1200x

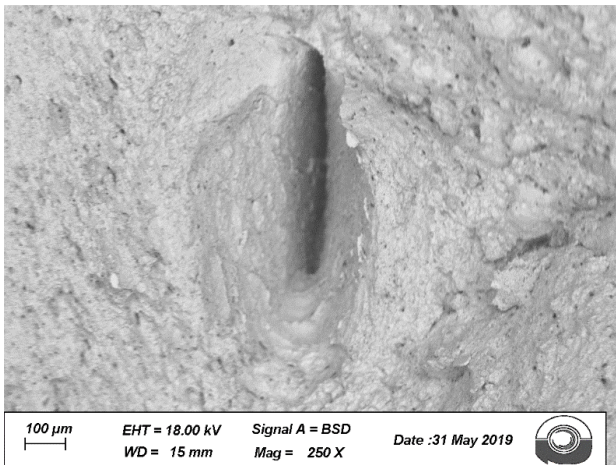


Figure 8.44 – Test 9 – Starting point 250x

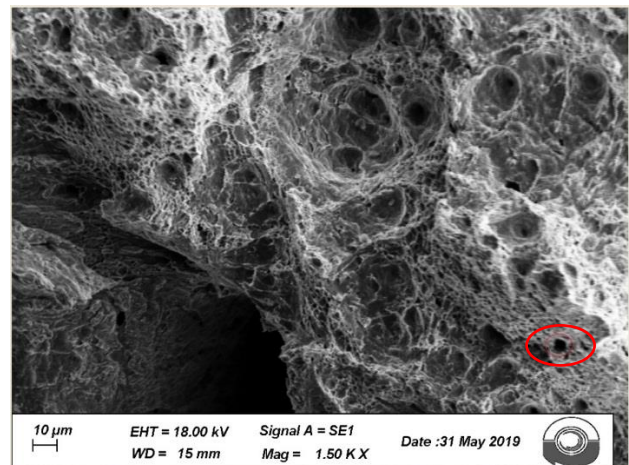


Figure 8.45 - Test 9 – Starting point 1500x

Since any inclusion were found near the starting points cleanliness analysis were made on a section of tension-tension specimens in order to verify the low contents of critical inclusions.

An inspectional area of 14.5 cm<sup>2</sup> were analysed both grade A and B, critical inclusions found are shown below.

### Grade A

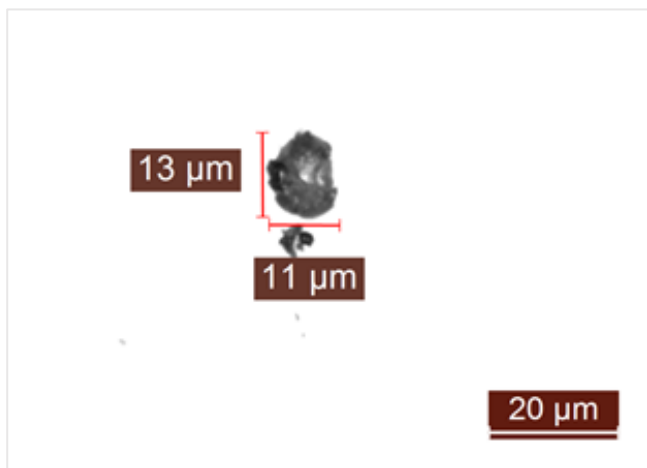


Figure 8.46 - Oxides type - grade A - 1000x

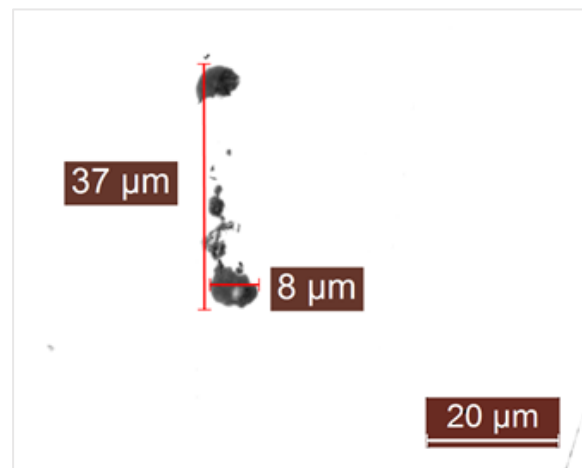


Figure 8.47– Aluminates type - grade A – 1000x

## Grade B

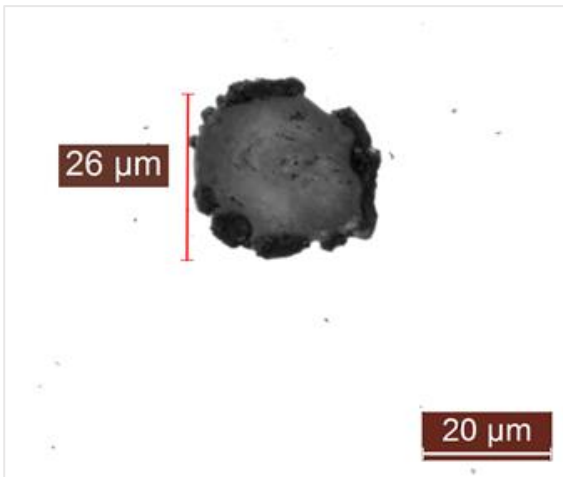


Figure 8.48 - Oxides type - grade B - 1000x

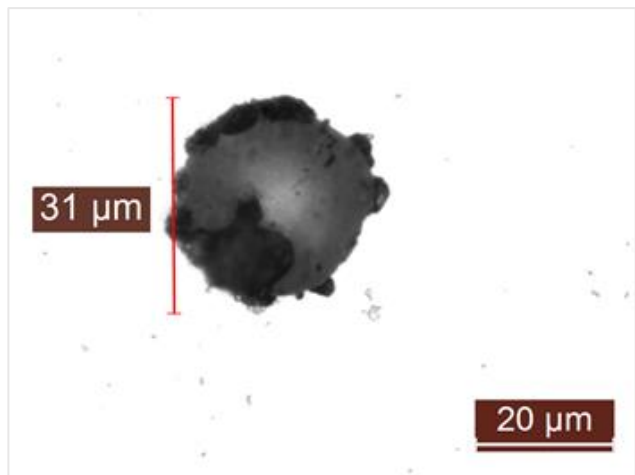


Figure 8.49– Oxides type - grade B – 1000x

Other inclusions were found, however they were not reported since they are very small. Results showed that both grade A and grade B are low contents of critical inclusions as expected.

A numerical simulation was made evaluating the increase of stress that would cause the inclusion in figure 8.49 if it was present in the fracture area.

It was decided to make the simulation with the stress of fatigue limit and  $Al_2O_3$  composition.

Maximum stress applied [Mpa]	540.8		
Maximum stress [MPa]	669		
Inclusion dimension [ $\mu$ m]	X	Y	Z
	31	31	31

Table 8.9 – Results

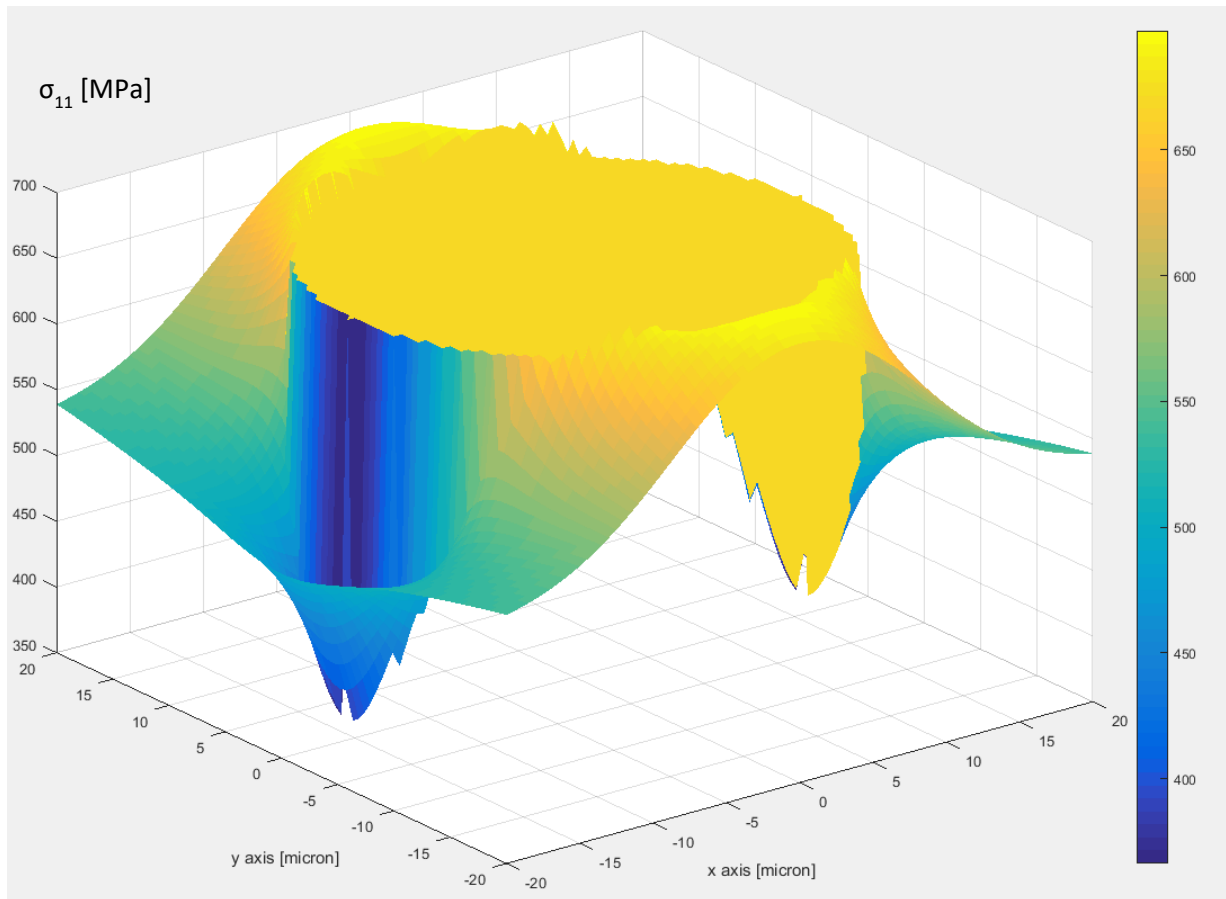


Figure 8.50 - Stress peak

Maximum stress evaluated at the boundary of the inclusion is more than the maximum stress applied in tension-tension test.

### 8.3 Balls test results

In order to define a new ball bearing life prediction  $L_{10}$  considering the effect of non metallic inclusion the following procedure has been applied:

- **Numerical model** is used in order to determine the increased of stress at the boundary of the critical inclusion.
- **The frequency** with which the inclusion strikes a race (inner and outer) is calculated (chapter 6), therefore it is known how often critical inclusion will be stressed compared to shaft revolutions.
- **Equivalent load  $P_{eq}$**  is found considering the inclusion presence.
- $L_{10}$  is calculated using  $P_{eq}$  found previously.

#### 8.3.1 Implementation of numerical model

Seven cases of different campaigns were analysed with Sem inspection, in each case fracture starts from a non metallic inclusion. In five cases more than one inclusion was present in the fractured area: for this reason the considered one was the one with the major increase of stress, since it was the worse from the fatigue life point of view. Probably, also in the other two cases the balls had few inclusions, but it could happen that they remained under the material that was peeling. Regarding the chemical composition, if the presence of some elements was negligible (evaluating the spectrum) these elements were neglected when considering the composition.

Original Hertzian matrix for ball-ring contact was calculated starting from data input below:

	Balls		Ring	
Young modulus [GPa]	210		210	
Poisson ratio	0.35		0.35	
Radius [mm]	1x	1y	2x	2y
	5.556	5.556	22.25	-6.322

Table 8.10 –Ball and ring characteristic

The force that acts on the normal direction of the contact for each ball has been calculated from this consideration:

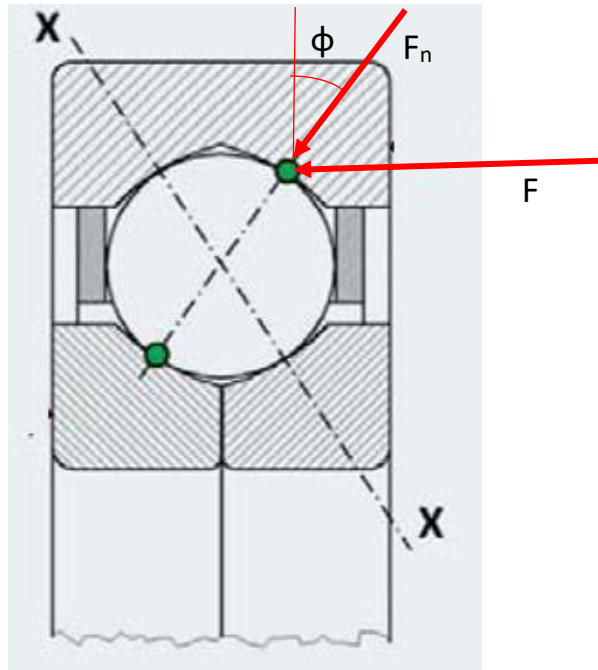


Figure 8.51 – Scheme of the ball-ring contact

- Test load: 34400 N
- Balls tested: 7
- $F$  = Axial force applied on each ball: 34400/7 N
- $F_n$  = Force that acts on the normal direction of the contact
- $\Phi$  = Angular contact: 28°

$$F_n = F \cdot \cos(90 - \Phi) = 2819 \text{ N}$$

In table 8.11 the values of the stress at the depth of the critical inclusion for each case are shown.

Stress Test	$\sigma_{11}$ [Mpa]	$\sigma_{12}$ [Mpa]	$\sigma_{13}$ [Mpa]	$\sigma_{21}$ [Mpa]	$\sigma_{22}$ [Mpa]	$\sigma_{23}$ [Mpa]	$\sigma_{31}$ [Mpa]	$\sigma_{32}$ [Mpa]	$\sigma_{33}$ [Mpa]	Tresca [Mpa]
1 [-453 um]	-480	0	-688	0	-45	-906	-688	-906	-1857	1432
2 [-562 um]	-340	0	-603	0	-2	-773	-603	-773	-1547	1228
3 [-600 um]	-304	0	-578	0	6	-733	-578	-733	-1459	1167
4 [-284 um]	-888	0	-848	0	-281	-1151	-848	-1151	-2583	1807
5 [-436 um]	-510	0	-704	0	-57	-930	-704	-930	-1917	1469
6 [-326 um]	-782	0	-816	0	-203	-1106	-816	-1106	-2415	1737
7 [-450 um]	-495	0	-695	0	-50	-915	-695	-915	-1880	1446

Table 8.11 – Stress at the depth of the inclusion

**Case 1: failed after 11.2h**

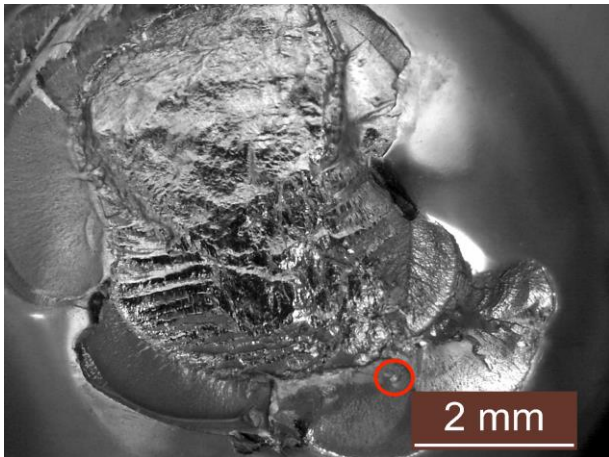


Figure 8.52 – Case 1 – Starting point 16x

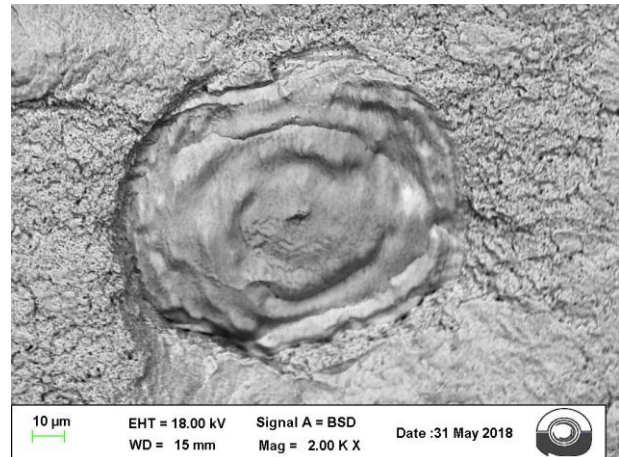


Figure 8.53 – Case 1 – Starting point 2000x

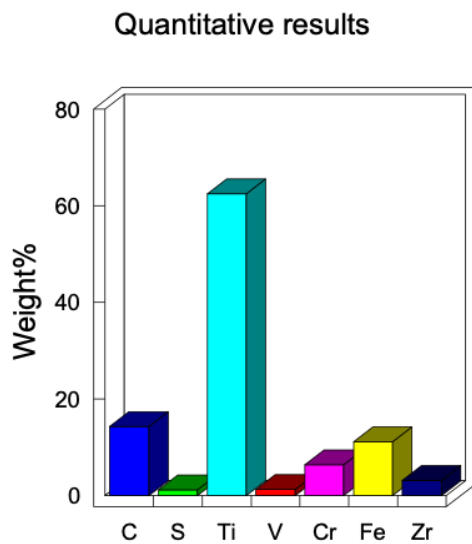


Figure 8.54 – Case 1 – Chemical composition

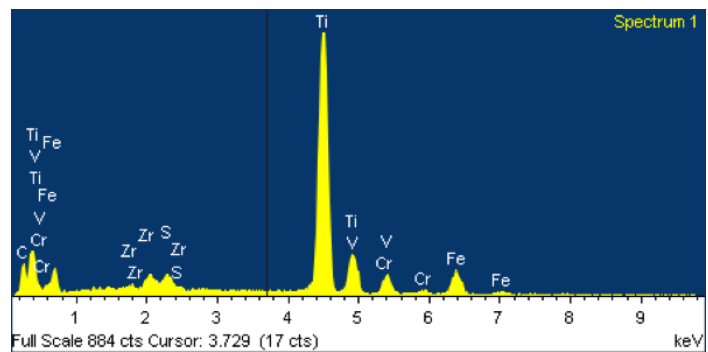


Figure 8.55 – Case 1 – Spectrum

Original Stress at the depth of inclusion [MPa]	1432		
Maximum Stress at the depth of inclusion [MPa]	1994		
Chemical composition	TiC		
Inclusion dimension [μm]	X	Y	Z
	1.67	4.34	1.67
Depth [μm]	453		

Table 8.12 – Results

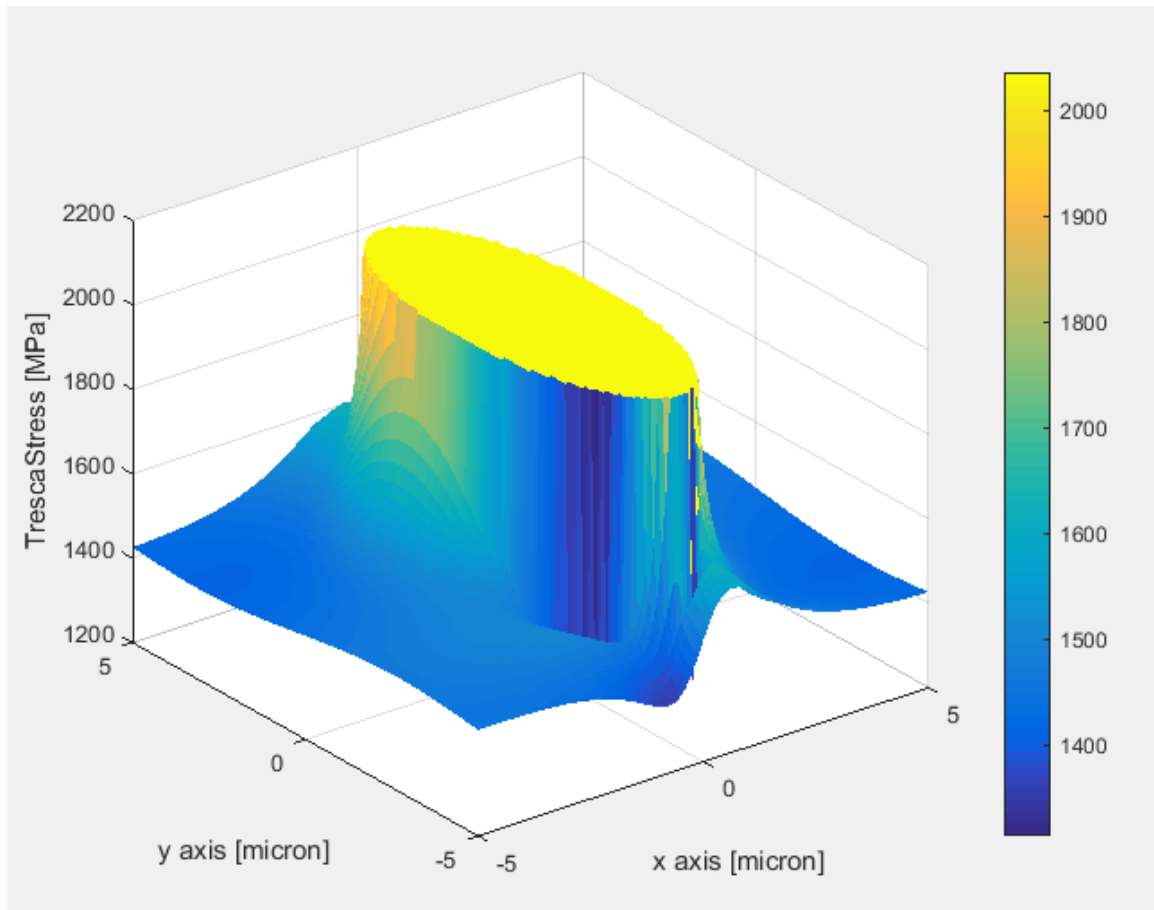


Figure 8.56 - Stress peak

**Case 2: failed after 33.9h**

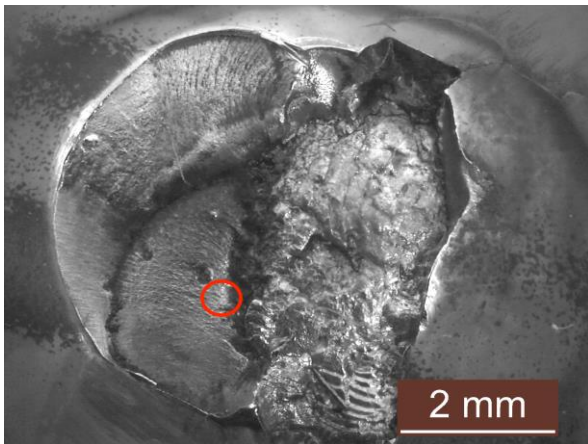


Figure 8.57 – Case 2 – Starting point 16x

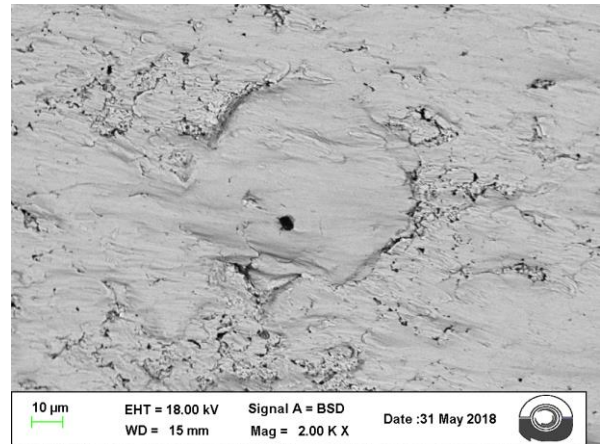


Figure 8.58 – Case 2 – Starting point 2000x

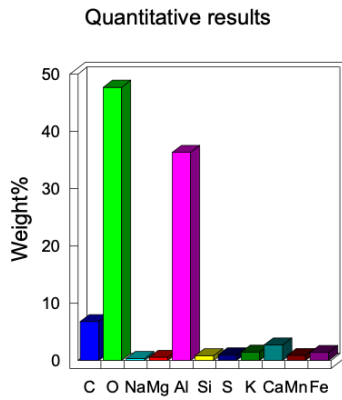


Figure 8.59– Case 2 – Chemical composition

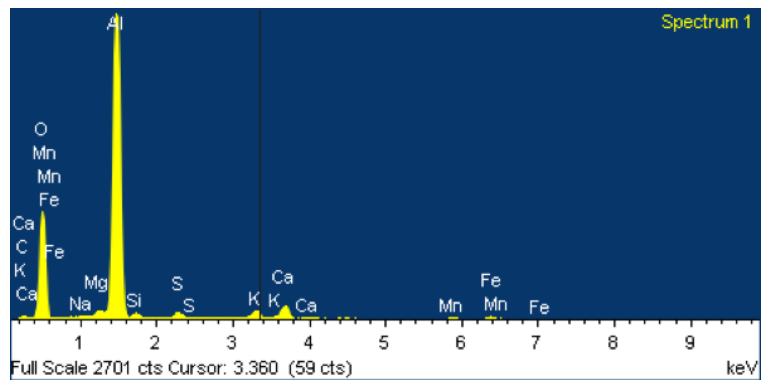


Figure 8.60 – Case 2 – Spectrum

Original Stress at the depth of inclusion [MPa]	1228		
Maximum Stress at the depth of inclusion [MPa]	1682		
Chemical composition	Al <sub>2</sub> O <sub>3</sub>		
Inclusion dimension [μm]	X	Y	Z
	1.67	2.67	1.67
Depth [μm]	562		

Table 8.13 - Results

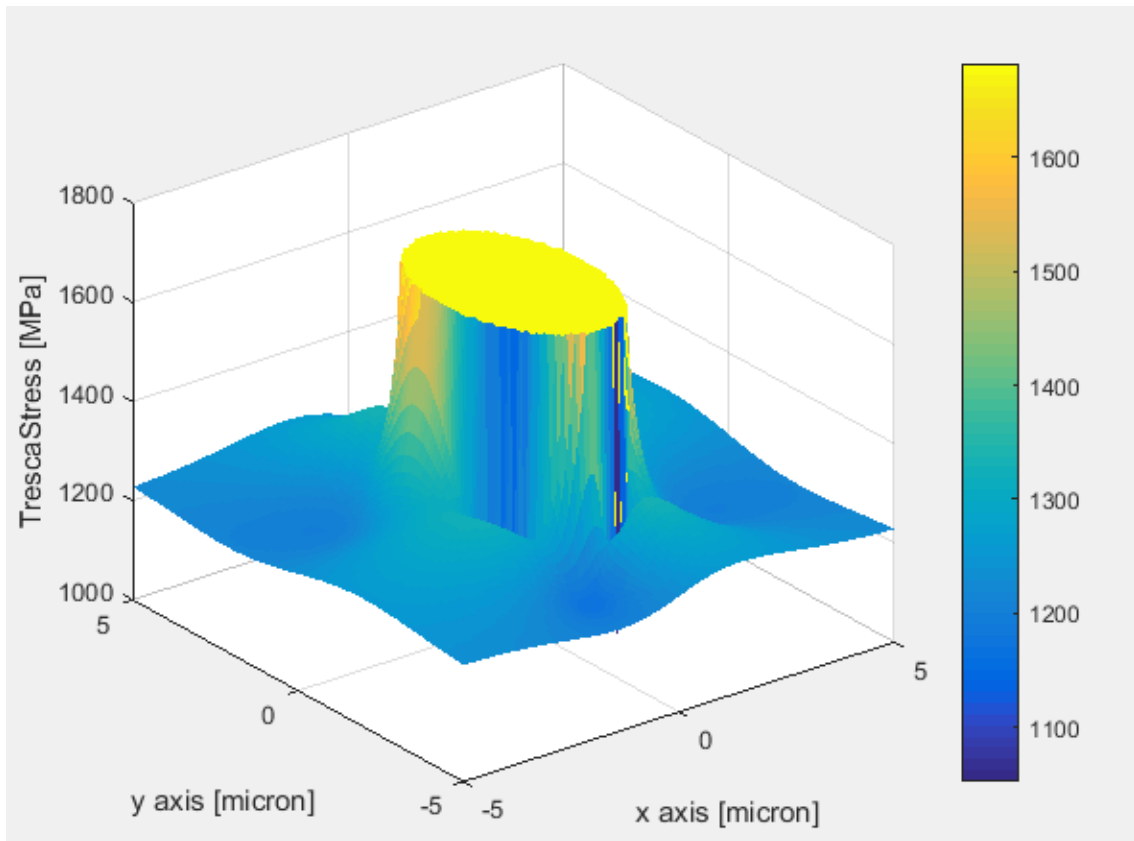


Figure 8.61 – Stress peak

**Case 3: failed after 46.9h**

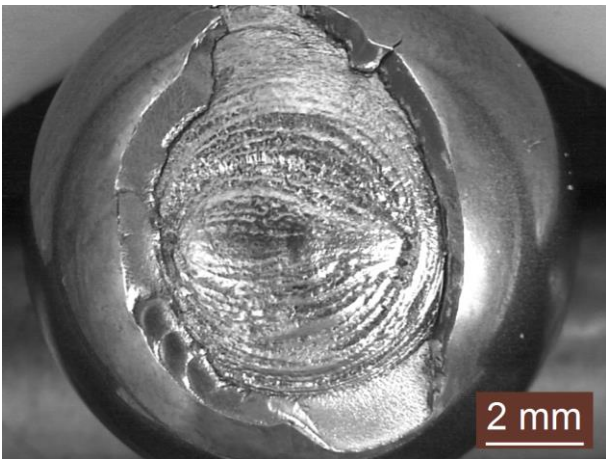


Figure 8.62 – Case 3 – Starting point 10x



Figure 8.63 – Case 3 – Starting point 700x

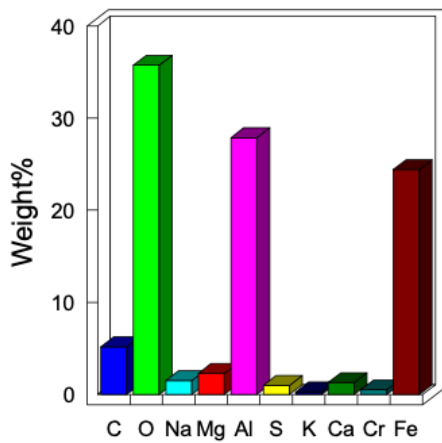


Figure 8.64 – Case 3 – Chemical composition

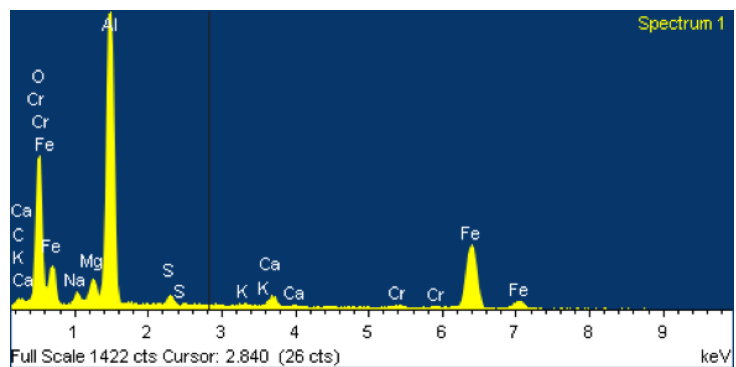


Figure 8.65 – Case 3 - Spectrum

Original Stress at the depth of inclusion [MPa]	1167		
Maximum Stress at the depth of inclusion [MPa]	1643		
Chemical composition	Al <sub>2</sub> O <sub>3</sub>		
Inclusion dimension [μm]	X	Y	Z
	7	49	7
Depth [μm]	600		

Table 8.14 - Results

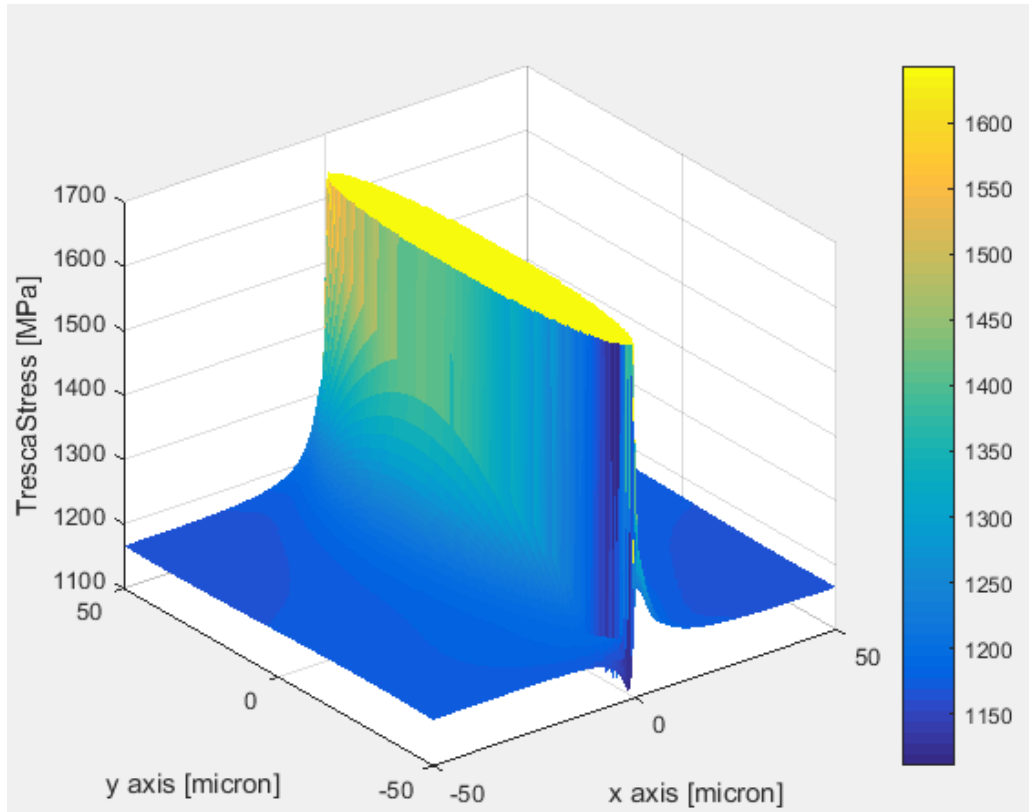


Figure 8.66 – Case 3 – Stress peak

**Case 4: failed after 21h**

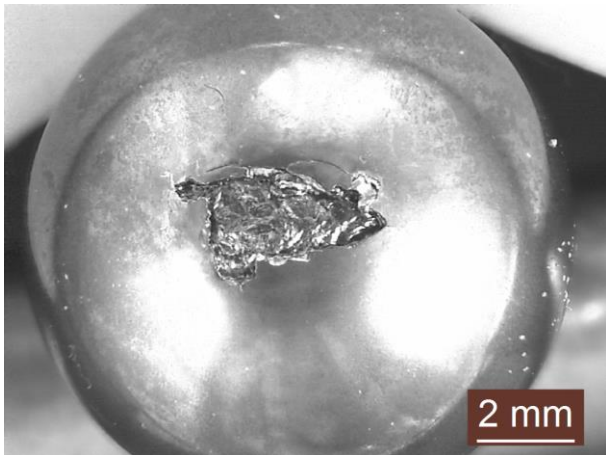


Figure 8.67 – Case 4 – Starting point 10x

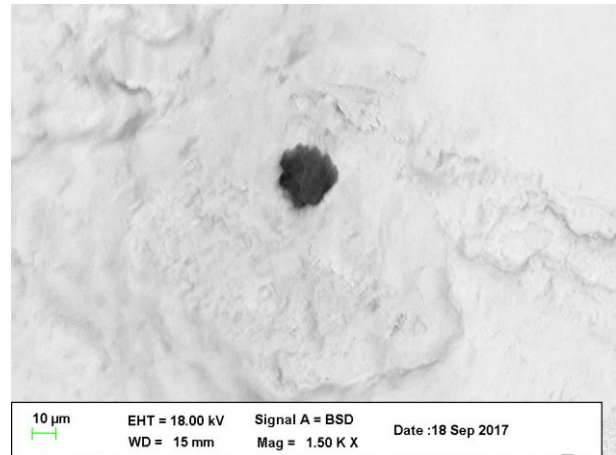


Figure 8.68 - Case 4 – Starting point 1500x

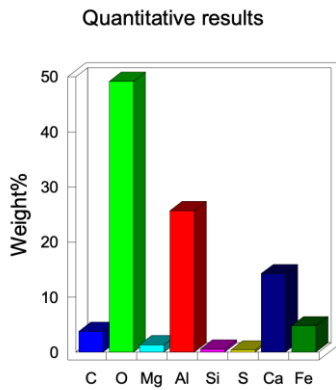


Figure 8.69 – Case 4 – Chemical composition

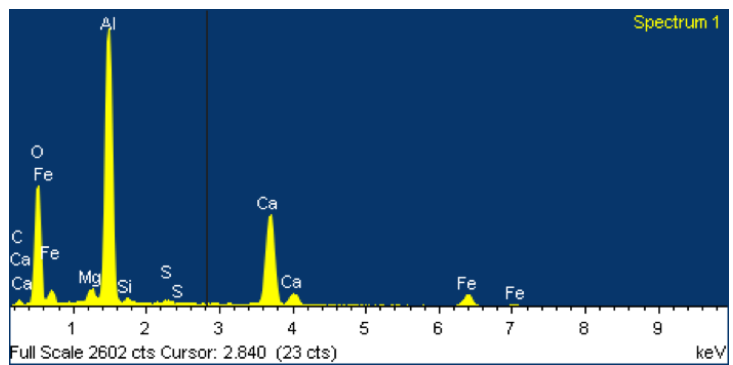


Figure 8.70 - Case 4 – Spectrum

Original Stress at the depth of inclusion [MPa]	1807		
Maximum Stress at the depth of inclusion [MPa]	2463		
Chemical composition	Al <sub>2</sub> O <sub>3</sub>		
Inclusion dimension [µm]	X	Y	Z
	12.5	12.5	12.5
Depth [µm]	284		

Table 8.15 - Results

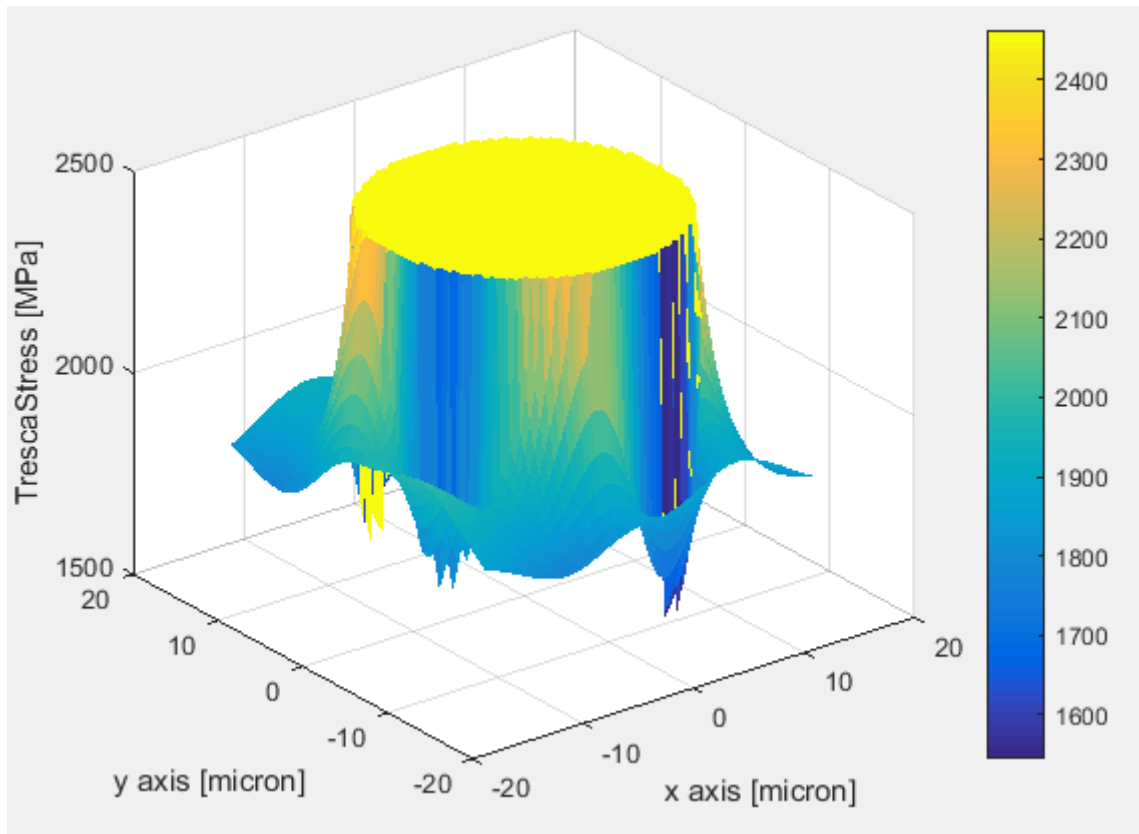


Figure 8.71 – Case 4 – Stress peak

Case 5: failed after 35h

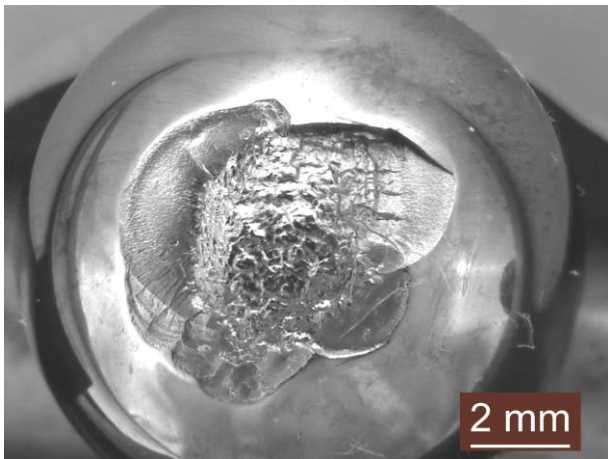


Figure 8.72 – Case 5 – Starting point 10x

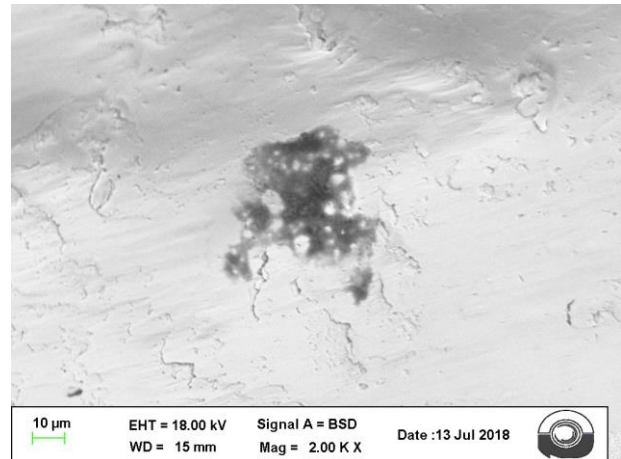


Figure 8.73 – Case 5 – Starting point 2000x

Quantitative results

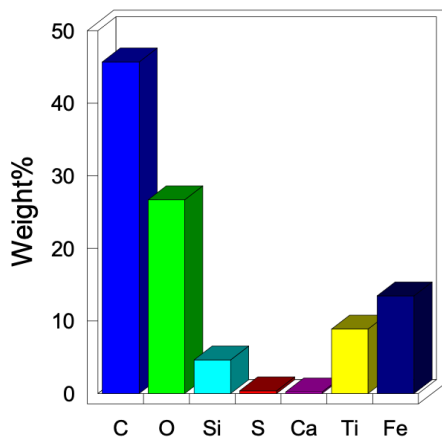


Figure 8.74 – Case 5 – Chemical composition

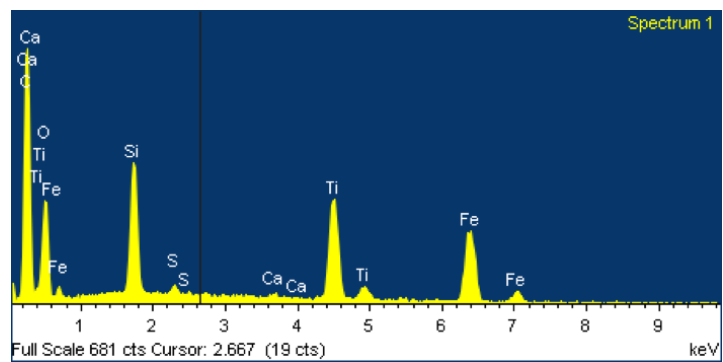


Figure 8.75 – Case 5 – Spectrum

Original Stress at the depth of inclusion [MPa]	1469		
Maximum Stress at the depth of inclusion [MPa]	1777		
Chemical composition	TiC		
Inclusion dimension [μm]	X	Y	Z
	4.5	4.5	4.5
Depth [μm]	436		

Table 8.16 - Results

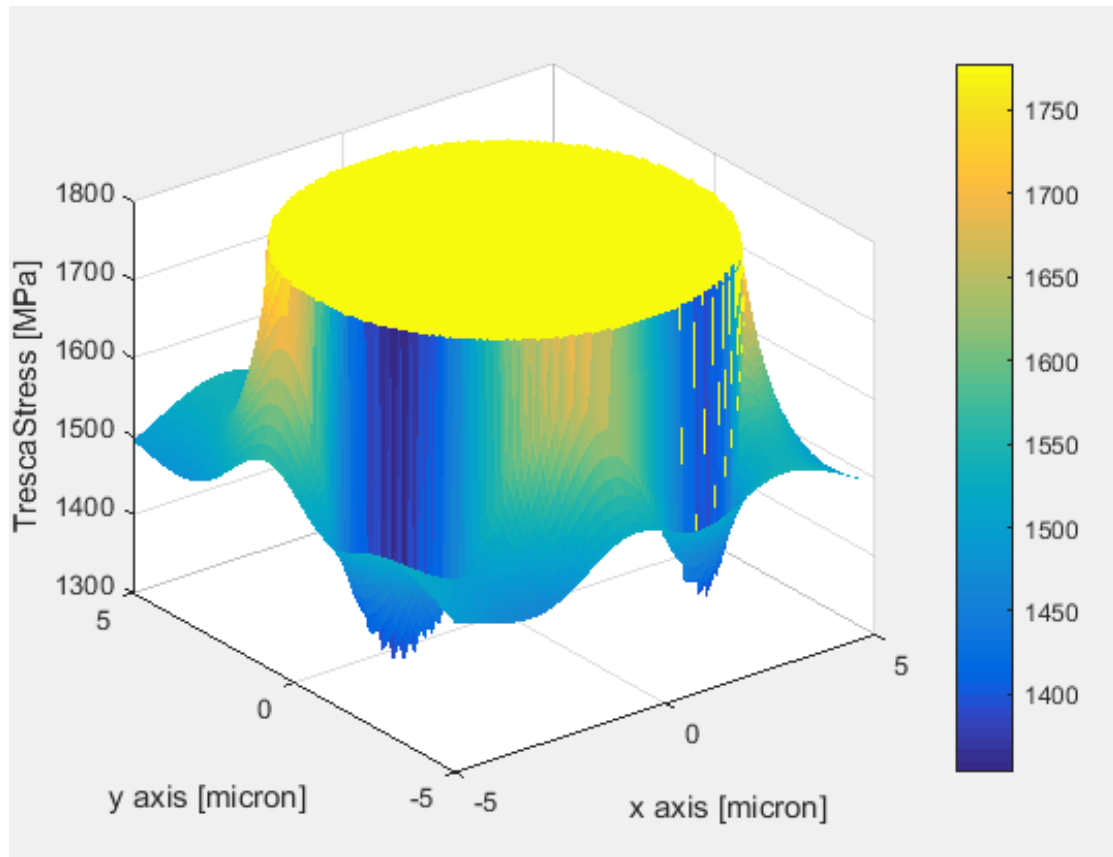


Figure 8.76 – Stress peak

Case 6: failed after 11.2h

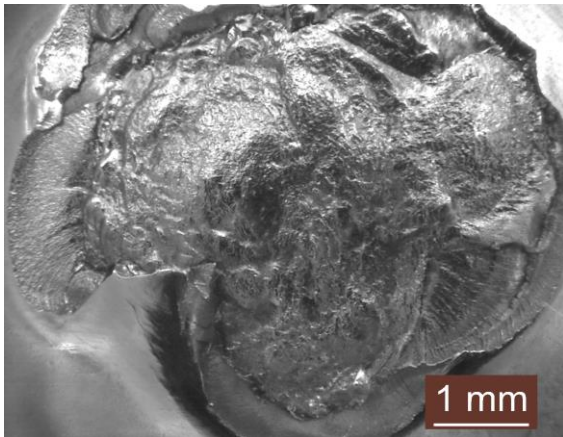


Figure 8.77 – Case 6 – Starting point 20x

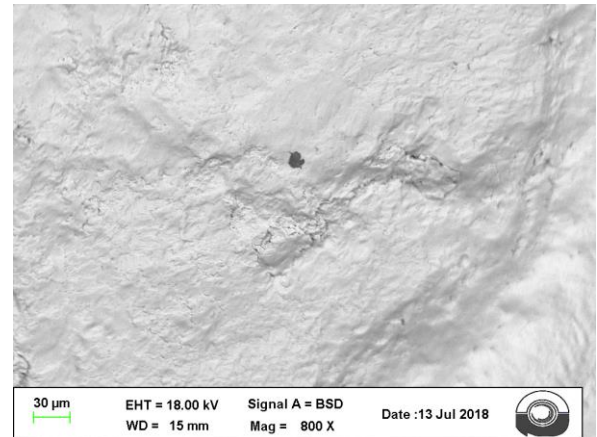


Figure 8.78 – Case 6 – Starting point 800x

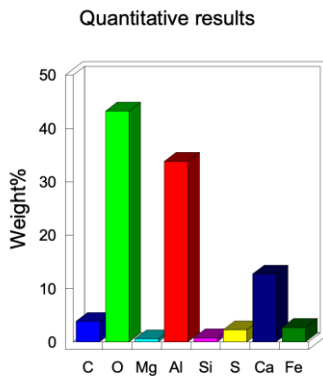


Figure 8.79 – Case 6 – Chemical composition

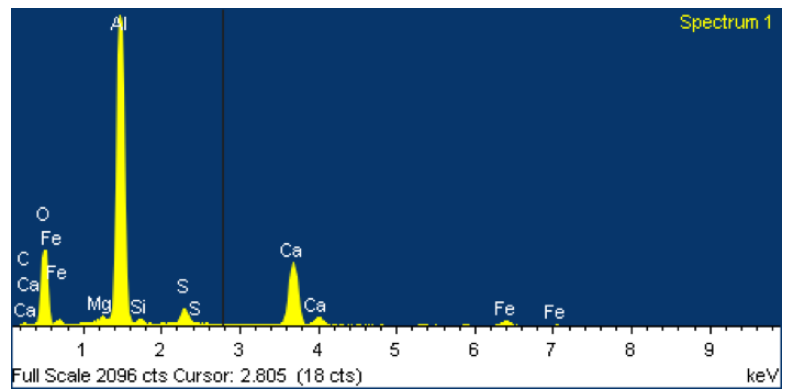


Figure 8.80 – Case 6 – Spectrum

Original Stress at the depth of inclusion [MPa]	1737		
Maximum Stress at the depth of inclusion [MPa]	2334		
Chemical composition	Al <sub>2</sub> O <sub>3</sub>		
	X	Y	Z
Inclusion dimension [μm]	12.34	10	10
Depth [μm]	326		

Table 8.17 - Results

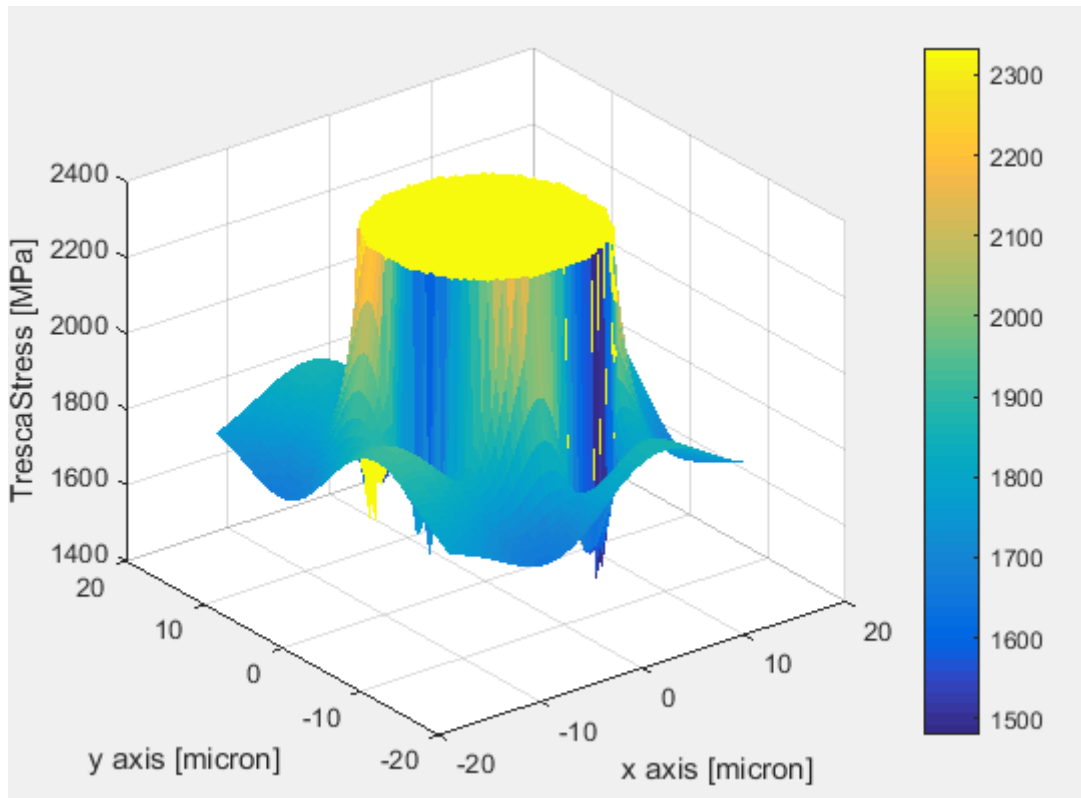


Figure 8.81 – Stress peak

Case 7: failed after 90.7h

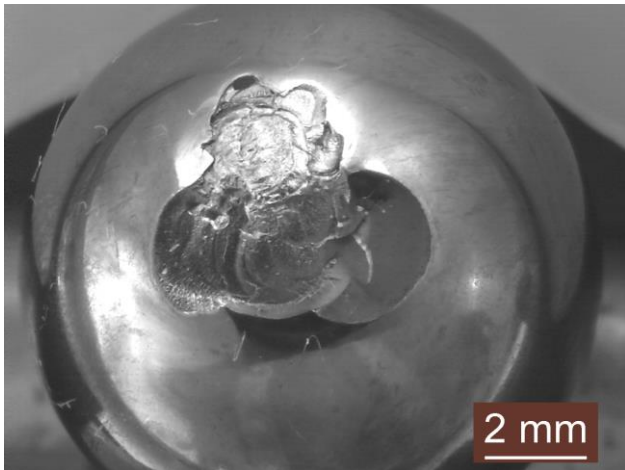


Figure 8.82 – Case 7 – Starting point 10x

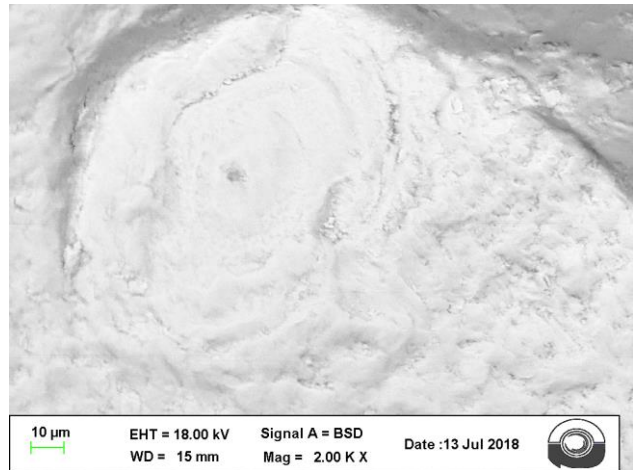


Figure 8.83 – Case 7 – Starting point 2000x

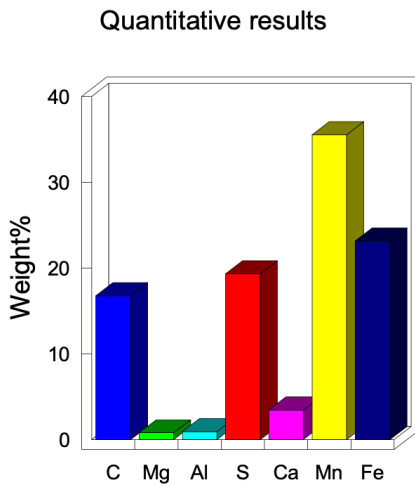


Figure 8.84 – Case 7 – Chemical composition

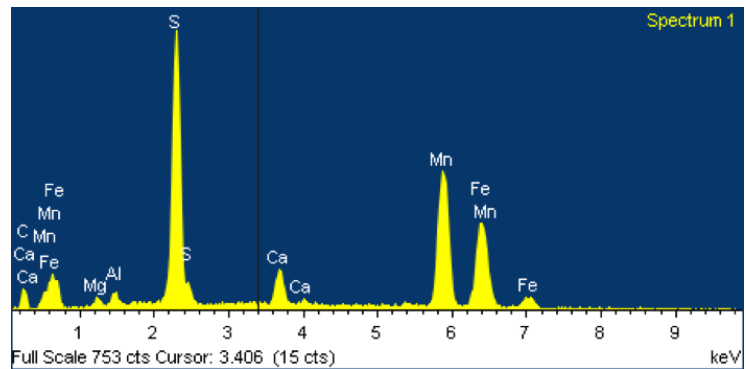


Figure 8.85 – Case 7 – Spectrum

Original Stress at the depth of inclusion [MPa]	1446		
Maximum Stress at the depth of inclusion [MPa]	1773		
Chemical composition	Al <sub>2</sub> O <sub>3</sub> /Carbides		
	X	Y	Z
Inclusion dimension [μm]	3.5	2	2
Depth [μm]	326		

Table 8.18 - Results

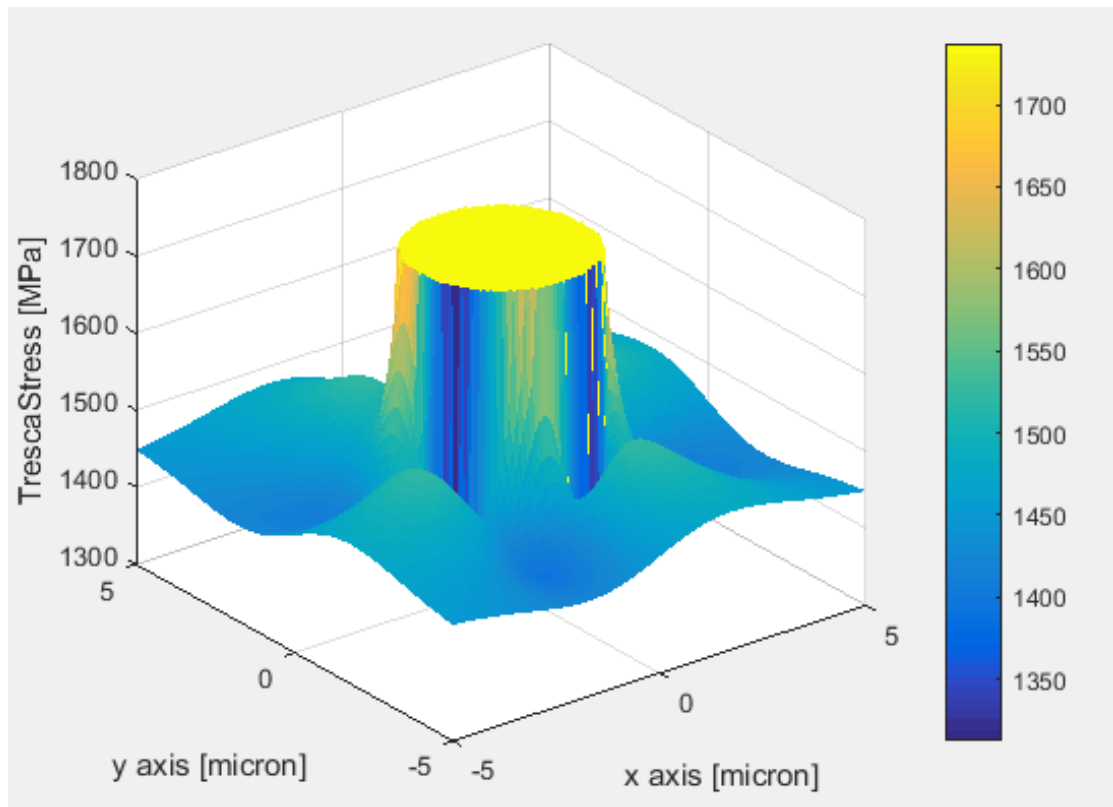


Figure 8.86– Stress peak

### 8.3.2 Ball bearing life prediction ( $L_{10}$ )

Since it is known the Tresca stress at the boundary of the inclusion, it is possible to calculate the inclusion theoretical load that would produce the stress peak at the boundary of the inhomogeneities if it was applied to a matrix without inclusion.

Case	1	2	3	4	5	6	7
Real load	34400	34400	34400	34400	34400	34400	34400
Theoretical load [N]	74552	70079	71570	84989	55168	74552	56659

Table 8.19 – Real load and theoretical load for all 7 cases

In order to calculate equivalent load that depend on inclusion presence a weighted average between Real Load and Theoretical load is made.

In chapter 6 it was estimated that inclusion is stressed every 20 shaft-rotation for the test condition used in this work, therefore weighted average could be calculate:

$$P_{eq} = (19 * \text{Theoretical Load} + \text{Real load}) \frac{1}{20}$$

Since  $L_{10}$  life is the time that 90 percent of a group of bearings will exceed without failing by rolling-element fatigue,  $L_{10}$  life show below are for group of balls that have the same critical inclusion at the same depth.

Case	1	2	3	4	5	6	7
$P_{eq}$ [N]	36408	36184	36258	36929	35438	36408	35513
$L_{10}$ [h]	27,4	27,4	27,4	27,4	27,4	27,4	27,4
$L_{10}$ with inclusion [h]	23,12	23,55	23,40	22,15	25,06	23,12	24,91
Percentage decrease [%]	-15,64	-14,07	-14,60	-19,16	-8,53	-15,64	-9,11

Table 8.20 –  $L_{10}$  life

Test results show that  $L_{10}$  life percentage decrease range is between 8.5% and 19% and and they are in agreement with the experimental data collected over the years in Pinerolo Plant of Tsubaki Nakashima Co., Ltd.

### 8.3.3 Simulation of worst cases

Simulation of the worst cases possible has been done for different ratio of semiaxis (a;b) :

- Larger inclusion possible (statistics of extreme values): Area  $616 \mu\text{m}^2$
- Chemical composition:  $\text{Al}_2\text{O}_3$
- Inclusion located at the depth of maximum Tresca stress:  $202 \mu\text{m}$

**Case 1:**  $a=14 \mu\text{m}$ ;  $b=14 \mu\text{m}$

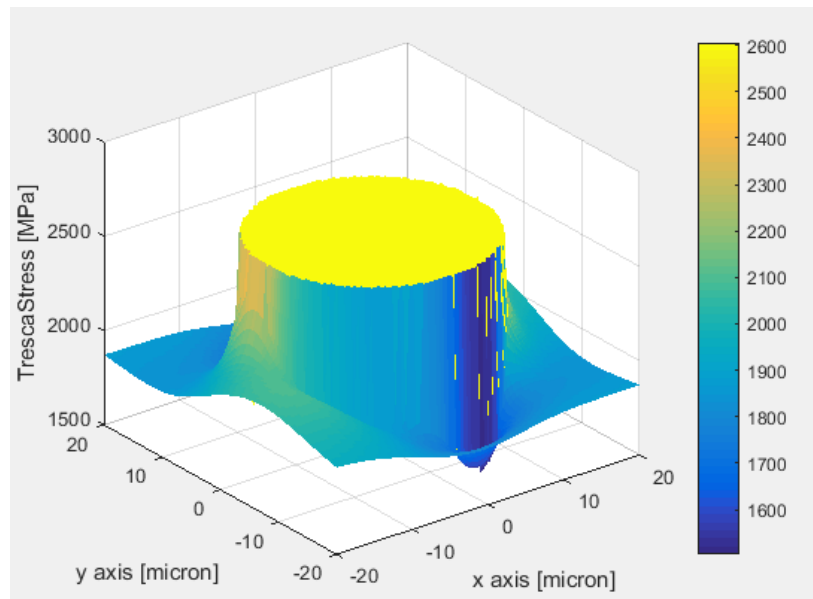


Figure 8.87 – Case 1 - Stress peak

**Case 2:**  $a=8.9 \mu\text{m}$ ;  $b=22 \mu\text{m}$

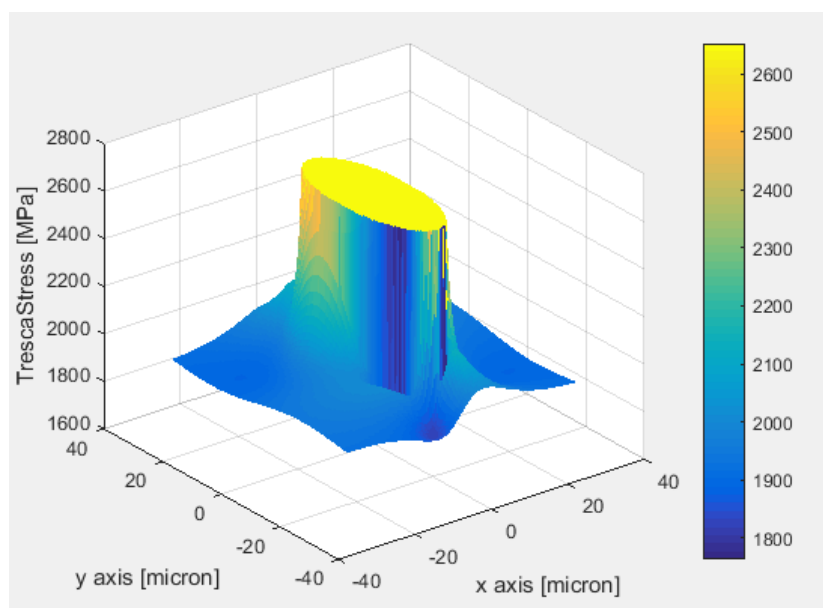


Figure 8.88 – Case 2 - Stress peak

Case 3:  $a=3\ \mu\text{m}$ ;  $b=65\ \mu\text{m}$

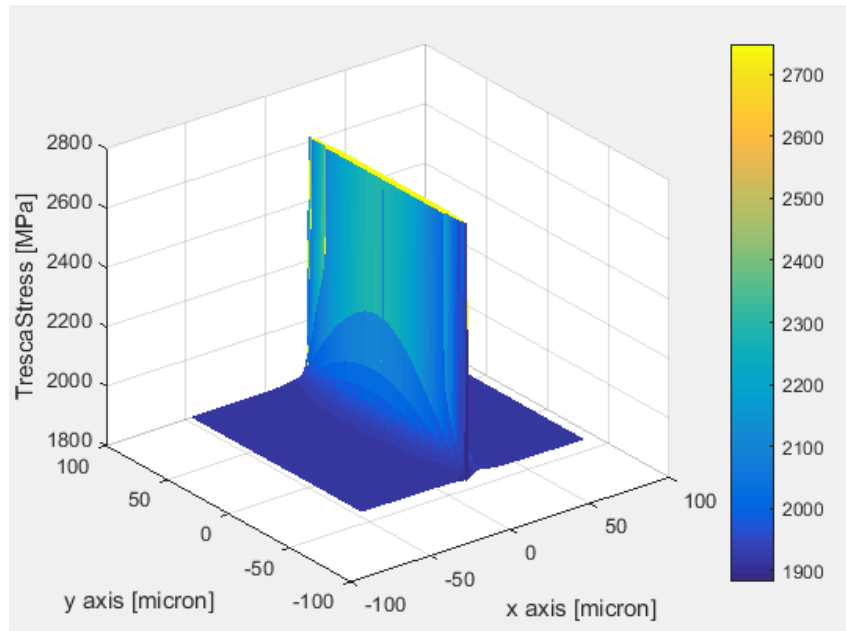


Figure 8.89 – Case 3 - Stress peak

Results in table 8.21 show that L10 life percentage decrease range is between 29.5% and 35%.

Case	1	2	3
Tresca stress original [Mpa]	1912	1912	1912
Tresca stress inclusion [Mpa]	2605	2652	2749
Real load [N]	34400	34400	34400
Theoretical load [N]	119283	125247	141649
Depth [ $\mu\text{m}$ ]	202	202	202
$P_{eq}$ [N]	38644	38942	39762
L10 [h]	27,4	27,4	27,4
L10 with inclusion [h]	19,30	18,89	17,74
Percentage decrease [%]	-29,57	-31,06	-35,24

Table 8.21 - Results

# Chapter 9

## 9 Conclusion

Aim of the project was to evaluate the effect of inclusion on ball bearing life prediction ( $L_{10}$ ). Different tests on different steel composition and a numerical simulation were made in order to better understand the influence of inclusions on the fatigue life. Both raw material and finished product (balls for bearings application) were evaluated: raw material was tested on rotating bending machine and tension-tension machine, while balls on special test rigs for bearings.

Numerical simulation of Eshelby model enabled to evaluate the increase of stress at the boundary of the inclusion for different shape, chemical composition, dimension. Results showed that shape and chemical inclusion are the most important factor, since a big difference between the length of the axis of inclusion or between the young's modulus of the inclusion and the steel matrix produced a high stress peak, instead dimension of the inclusion is not relevant since the stress peak was the same for different size. However in real case size of inclusion is a key factor for fatigue limit, since only inhomogeneties larger than critical dimension could be detrimental for bearing life and also bigger is the inclusion bigger is the stressed area and the probability of failure. An other important factor in rolling contact fatigue is the depth of inclusion since if the inclusion is shallower than a certain value are not critical for failures, on the other point an inclusion located at the depth of maximum Tresca stress is more dangerous.

Tests on raw material have been conducted on different steels composition. Results have shown that presence of inclusions has a primary importance on fatigue life, since, contrary to the expectation, the fatigue limit of the steel with more alloy elements was lower. Cleanliness analysis showed that higher alloy steel has a lot of critical inclusions so there wasn't the positive effect on fatigue life of silicon and other alloy elements.

A lot of test on finished products were made, in this work only seven of the failed balls are considered, in all the cases the starting point was a microinclusion, the chemical composition, shape, dimension and depth of which were determine with Sem Inspection.

After defining the characteristics of inclusions Eshelby model [15] was applied in order to calculate the stress peak at the boundary of the inhomogeneties, from the stress it is possible to evaluate the inclusion theoretical load that would produce the stress at the boundary of the inclusions if it was applied. Then the frequency with which the inclusion strikes a race, inner and outer, was calculated in order to evaluate the number of times that inclusion is stressed compared to bearing revolution.  $L_{10}$  life, that are for group of balls that have the same critical inclusion at the same depth, were determined with Zaretski model [27] using an equivalent load depending on inclusion presence. Equivalent load was defined as weighted average between Real Load and Theoretical load.

Test results show that  $L_{10}$  percentage decrease range is between 8.5% and 19% and are in agreement with the experimental data collected over the years in Pinerolo Plant of Tsubaki Nakashima Co., Ltd.

Simulation of the worst cases possible has been done. It was chosen the largest inclusion possible (determined by statistics of extreme values) of  $Al_2O_3$  (highest young's modulus among the common inhomogeneties that are found in AISI 52100) located at the depth of the maximum Tresca stress. Results show that  $L_{10}$  percentage decrease range is 29% for sphere shape, that increases until 35% for big difference of the length of axis.

# Chapter 10

## 10 Future Works

Results obtained in this works are satisfactory, however two great aspects were not considered in  $L_{10}$  life evaluation:

- The effect of inclusions was analysed only in terms of shape, depth and chemical composition. From the state of art it is known that also the size has a great relevance, statistics of extreme values enables to identify the larger inclusion but it would be necessary to define a coefficient that includes the size effect.
- It is difficult to define exactly how a ball spins, in this works a first attempt was made but a better model should be developed in order to calculate precisely the frequency with which the inclusion strikes a race, inner and outer.

As regards the numerical model could be improved introducing Moschovidis-Mura [17] consideration on interaction of ellipsoidal inhomogeneties, since in this project a sequence of inclusions are considered as a stand-alone inclusion with an elongated semiaxes that covers the distance from the first to the last inclusion of the stringer.

# Bibliography

- [1] H.K.D.H. Bhadeshia. *"Steels for bearings"*, SKF University Technology Centre for Steels, University of Cambridge, and UK, 2012.
- [2] Hashimoto K. et al. *"Study of rolling contact fatigue of bearing steels in relation to various oxide inclusions"*. In: Materials and Design, 2010.
- [3] P.K. Pearson J.F. Braza and C.J. Hannigan. *"The performance of 52100, M-50 and M-50 NiL steels in radial bearings"*. In: International OffHighway and Powerplant Congress SAE Technical Paper Series,1993.
- [4] P. Lamagnere et al. *"A Physically based model for endurance limit of bearing steels"*, In: Journal of Tribology ,1998.
- [5] Moghaddam S. M. et al. *"Effect of non-metallic inclusions on butterfly wing initiation, crack formation, and spall geometry in bearing steels"*, In: International Journal of fatigue (2015).
- [6] Nagao M., Hiraoka K., and Unigame Y. *"Inuence of non metallic inclusion size on rolling contact fatigue life in bearing steel"*, In: Sanyo Tech. Rep. ,2005.
- [7] Seki T. *"Evaluation procedures of nonmetallic inclusions size by statistics and extreme value and prediction of fatigue life in bearing steels"*, In: Aichi Tech. rep. ,1995.
- [8] Guan J. et al. *"Effects of non metallic inclusions on the crack propagation in bearing steel"*. In: Tribology International ,2016.
- [9] Michele Cerullo and Viggo Tvergaard *"Micromechanical study of the effect of inclusions on fatigue failure in a roller bearing"*, Kgs. Lyngby, Denmark, 2014.
- [10] Stienon A. et al. *"A new methodology based on X-ray micro tomography to estimate stress concentrations around inclusions in high strength steels"*. In: Mater Sci Eng A ,2009.
- [11] Yutaka Neishi et al. *"Influence of the inclusion shape on the rolling contact fatigue life of carburized steels"*, The Minerals, Metals & Materials Society and ASM International, 2012.
- [12] Y. Murakami, *"Inclusion Rating by Statistics of Extreme Values and Its Application to Fatigue Strength Prediction and Quality Control of Materials"*, Journal of Research of the National Institute of Standards and Technology, 1994.

- [13] W. Weibull. *"A statistical theory of the strength of Materials"*, Royal Swedish Institute for Engineering Research, 1939.
- [14] E. Ioannides and T.A. Harris. *"A Physically based model for endurance limit of bearing steels"*, In: *Journal of Tribology*, 1985.
- [15] J.D. Eshelby. *"The determination of the elastic field of an ellipsoidal inclusion, and related problems"*, Department of physical metalurgy, University of Birmingham, 1957.
- [16] Courbon J. et al. *"Inuence of inclusion pairs, clusters and stringers on the lower bound of the endurance limit of bearing steels"*. In: *Tribology International*, 2003.
- [17] Mura T. *"Micromechanics of defects in solid"*, Dordrecht, 1987.
- [18] Vincent et al. *"A Physically based endurance limit model for through hardened and surface hardened bearing steels"*. ASTM International: Bearing Steel Technology; 2002.
- [19] Bryan Allison and Anup Pandkar, *"Critical factors for determining a first estimate of fatigue limit of bearing steels under rolling contact fatigue"*, Usa, 2018.
- [20] Jalalahmadi and Sadeghi, *"Material Inclusion Factors for Lundberg-Palmgren–Based RCF Life Equations"*, *Tribology Transactions*, 2011.
- [21] Lundberg G. and Palmgren A., *"Dynamic capacity of roller bearings"*, Sweden, 1952.
- [22] T.A. Harris, M.N.Kotzalas. *"Rolling Bearing Analysis: Essential Concepts of Bearing Technology"* CRC Press, Florida, USA, 2007.
- [23] Sadeghi F. et al. *"Microstructural Alterations in Bearing Steels under Rolling Contact Fatigue Part 1—Historical Overview"*, 2012.
- [24] W. Cheng, *"Spalling mechanism of bearings and gears"*, USA, 2001
- [25] Sadeghi F. et al. *"A review of rolling contact fatigue"*, *Journal of Tribology*, 2009.
- [26] M.A. Raegan T.A. Harris and R.F. Spitzer. *"The effect of hoop and material residual stresses on the fatigue life of high speed, rolling bearings"*, In: *Tribology Transactions*, 1992.
- [27] E. Zaretsky. *"Rolling bearing life predictions, theory and application"*, Glenn research center, Cleveland, Ohio, 2013.
- [28] [https://en.wikipedia.org/wiki/Non-metallic\\_inclusions](https://en.wikipedia.org/wiki/Non-metallic_inclusions)
- [29] ASTM E45 Int. *"Standard Methods for Determining the Inclusion Content of Steel"*.

- [30] Sangryun Lee et al. *"Modified Eshelby tensor for an anisotropic matrix with interfacial damage"*, Department of Mechanical Engineering and Department of Mathematical Sciences, Korea, 2018.
- [31] Pollard D. D. Meng C. Heltsley W. *"Evaluation of the Eshelby solution for the ellipsoidal inclusion and heterogeneity"*, In: Computers and Geosciences, 2011.
- [32] Healy D. *"Elastic field in 3D due to a spheroidal inclusion - MATLABcode for Eshelby's solution"*, In: Computers and Geosciences, 2008
- [33] Surojit Poddar, Madan Lal Chandravanshi, *"Ball Bearing Fault Detection Using Vibration Parameters"*, Department of Mechanical Engineering, Indian school of Mines, Dhanbad, Jharkhand, India.
- [34] Robert B. Randall, *"Rolling element bearing diagnostics - A tutorial"* School of Mechanical and Manufacturing Engineering, University of New South Wales, Sydney, NSW 2052, Australia.
- [35] E.P. Kingsbury. *"Precessional slip in angular contact ball bearing"*, Bearing center, the Charles Stark Draper Laboratory, Cambridge, 1981.
- [36] Gumbel EJ. *"Statistics of extreme"*, New York and London, Columbia University Press, 1958.
- [37] H.V. Atkinson, G. Shi, *"Characterization of inclusions in clean steels: "a review including the statistics of extremes methods"*, Department of Engineering Materials, University of Sheffield, UK, 2002.